LINEAR SYSTEMS THEORY
APPLIED TO A HORIZONTALLY LAYERED CRUST

by

OLIVER GEORGE JENSEN

B.Sc. University of British Columbia, 1964
M.Sc. University of British Columbia, 1966

A THESIS SUBMITTED IN PARTIAL FULFILMENT OF

THE REQUIREMENTS FOR THE DEGREE OF

DOCTOR OF PHILOSOPHY

in the Department

of

GEOPHYSICS

We accept this thesis as conforming to the

required standard

THE UNIVERSITY OF BRITISH COLUMBIA

December, 1970

ABSTRACT

Elastic wave propagation in a multilayered crust with causally or acausally attenuating layers is formulated directly in terms of linear systems theory. The solution of the linear systems analog determines the wave motions at the free surface, motions of all internal boundaries and the waveforms propagated into the mantle in response to plane P or S waves generated within the layering or entering into the crust. The particular problem solved is the determination of the response of an n-layered crust to teleseismic P or S waves incident with arbitrary angle at the crustal base. Trivial extensions of this problem would allow reflection solutions.

Numerical solutions have been accomplished in both the frequency domain and the time domain. The Fourier solution restricted to a non-attenuating crust is equivalent to the standard Haskell matrix solution of elastic wave equations. Direct time domain solutions allow the syntheses of seismograms considering internal crustal absorption.

For demonstration of the utility and advantages of the theory, the linear systems formulation has been applied to studies of the elastic wave response of the central Alberta crust using P waves from 6 teleseismic events.

Frequency domain comparisons between the theoretical and experimental spectral amplitude V/H ratios have shown that, although the theoretical effect of attenuation within the crust can be considerable, little improvement in correlations between theory and experiment has been achieved by considering plausible crustal absorption models. Although significant similarities between the theoretical and experimental V/H ratios were found below 2 Hz, little

correlation was apparent at higher frequencies. Background and scattering noise partly contributed to this effect and it is also probable that insufficient detail and accuracy was available for the model crustal sections.

Time domain synthetic seismograms have been determined which well correspond to the early P coda of several of the experimental records. Assumptions on the event source motions and the mantle properties are required to determine incident P waveforms for these solutions. Causal attenuation within the crustal layering was included. Correlations between the synthetic seismograms and the experimental records has been found to decrease rapidly with time following the P onset. It is suggested that this effect is primarily due to background noise and possible scattering of the waves within the crust. Furthermore, it is probable that the waveforms used for these solutions based on the source motion and mantle attenuation assumptions were not sufficient.

A major apparent advantage of the new formulation is that causal and acausal attenuation solutions are permitted in both the frequency and time domains. Also, the large body of communications theory mathematics can now be applied directly to the propagation problem and could prove useful in attempts at the solution of the non-normal incidence inverse problem.

TABLE OF CONTENTS

LIST OF TABLES

LIST OF FIGURES

ACKNOWLEDGEMENTS

I wish to thank Dr. R. M. Ellis for his invaluable aid and encouragement during the development of this research. I am also grateful to my advisory committee with Drs. G. K. C. Clarke, R. M. Clowes and R. D. Russell for useful discussions and criticisms of various phases of the work.

I would also like to acknowledge the contribution of the Department of Geophysics staff whose preparation of the seismograph field equipment, recording of the experimental data and preparation of the digitization equipment was so necessary to much of this study. During this experiment, equipment was made available by the Seismology Division, Earth Physics Branch and both equipment and facilities were provided by the University of Alberta.

I would also like to thank Judy McLean for a fine job typing the manuscript.

This research was supported by the National Research Council (Grant A-2617) and the Defence Research Board of Canada (Grant 9511-76). The author was partly supported during this research by a University of British Columbia Graduate Fellowship.

CHAPTER I

GENERAL INTRODUCTION

1.1 Introduction

Seismologists have been investigating the propagation of elastic waveforms in horizontally multilayered media since the early development of seismic exploration methods in order to determine the crustal structure and the effects of the structure on seismic waves. In addition to the obvious practical applications in oil and mineral exploration, a knowledge of crustal propagation is necessary to the continuing advance of earthquake seismology. For example, much of the character of a seismogram is generated by the elastic properties of the crust underlying a seismograph station. Thus it is useful to remove these complicating effects in order to study the details of focal mechanisms and to refine our knowledge of the earth's interior. Furthermore, since crustal information is contained in earthquake seismograms, analysis procedures based upon a thorough understanding of elastic propagation could be useful to obtain crustal structure from these seismograms.

The first satisfactory mathematical analysis of elastic wave propagation in horizontally layered structures was that of Thomson (1950) which was subsequently generalized to include both body waves and surface waves by Haskell (1953). As well as surface wave applications, several investigators (e.g., Phinney, 1964; Ibrahim, 1969) have applied the Haskell matrix method to the analysis of earthquake body waves. The Haskell-Thomson approach obtains the propagation solution in terms of frequency component amplitudes; the more recent work of

Wuenschel (1960) for normal incidence and Frasier (1970) for non-normal P and SV motions permit the determination of time domain crustal responses. For vertical incidence P waves, extensions of these methods and other analytical approaches to the inverse problem of determination of the layer paramenters from earthquake and exploration seismograms have received considerable attention in the recent literature (e.g., Goupillaud, 1961; Claerbout, 1968; Ware and Aki, 1969).

This thesis presents a new formulation for the direct propagation problem using linear systems theory which allows both P and SV motions of arbitrary angle with the vertical within the layering and solution in either the frequency or time domain. Linear systems and analog procedures have been used previously. For example, the more restrictive one-dimensional problem of vertical P-wave propagation has been studied in systems (Lindsey, 1960), analog (Sherwood, 1962) and communications theory (Robinson and Treitel, 1966) terms. Also, surface wave normal dispersion has been described by Mueller and Ewing (1962) by means of a linear systems model.

It is notable that when an elastic wave travels through a structured material, a complex record of the elastic properties along the travel path is retained by the wave. Hence, analysis of the wave can provide structural information. This is the essential goal of the inverse seismic problem. The relatively simple geometry of the horizontally multilayered crust leads one to expect that inverse solutions may be first possible for this problem. However, the complete inverse solution also demands that the propagation characteristics due to all elastic effects in the crust are well understood. This thesis should help to extend this understanding.

The inclusion of attenuation, both causal and acausal is new in this work. However, extensions of other approaches may also allow the feature. For instance, Haskell (1953) suggested a possible means for including attenuation in his formulation; derivatives of the Haskell method (e.g., Wuenschel, 1960; Frasier, 1970) could possibly be modified to permit crustal absorption.

The linear systems approach has a further advantage that the direct time and frequency domain problems are cast in very similar forms. Thus, the correspondence of time series and spectral response characteristics are particularly apparent. The equivalence of the time and frequency solutions by other approaches is not direct.

One outstanding feature of a systems formulation is that a great body of analytical techniques already exists, particularly in automatic control engineering and communications engineering, which now can be applied to the problem. Possible further success in determining crustal properties from earthquake and reflection seismograms could be derived by using these mathematical tools. In the past, communications theory has been of great interest to many geophysicists and much recent advance of geophysics has been gained using these methods. Thus, a direct formulation of the propagation problem in the systems form may even broaden the interest among these geophysicists already using communications theory methods. A last consideration which may be of consequence is the fact that the systems form of the problem can lead to direct mechanical and electrical analog procedures. With the recent developments in microelectronic digital logic, for example, small hard-wired computers could efficiently solve propagation problems. The possibility of analog time domain approaches also exists.

The basic assumptions required by the linear systems approach are similar to those used in other methods. Distinct layers having isotropic velocities, uniform densities and welded boundaries are necessary. Plane rotational and compressional waves are considered. Attenuation with an arbitrary complex dependence on frequency is also allowable in each layer. The general solution of the problem requires the determination of the motions on the free surface and within the medium in response to source wave motions generated within the layering or entering into the medium. The choice of the source location of the plane wave generation determines the nature of the physical problem; either the reflection or transmission problem is soluble.

1.2 Outline of Thesis

(a) The systems description of crustal transmission of elastic waves is first obtained in the frequency domain for normal incidence plane waves impinging on a horizontally multilayered crust from a basement halfspace. This restricted formulation is then generalized to non-normal conditions.

(b) The analogous time domain formulation is derived from the general frequency description.

(c) The utility of the theory is demonstrated in comparison analyses with a set of earthquake and nuclear event seismograms recorded in central Alberta. Both time and frequency analyses as well as seismogram synthesis are obtained.

(d) Extensions of the method are suggested which could allow analysis of propagation in crusts possessing complex linear and non-linear properties. The possibility of inverse solutions is also indicated.

The problem has been specifically formulated to describe properties of teleseismic seismograms: that is the crustal transmission problem. The obvious extension to permit normal incidence reflection solutions is noted.

CHAPTER II

THE LINEAR SYSTEM THEORY FOR A MULTILAYER CRUST

2.1 Description of the Problem

In this work elastic propagation is to be formulated in two dimensions for waveforms incident on a horizontally layered medium from a halfspace beneath. This model represents a teleseismic arrival impinging on a layered crust from a basement.

Each crustal layer i is specified by its compressional and shear wave velocities α_i, β_i; density ρ_i and thickness η_i. The P and SV ray angles in each layer, designated e_i and f_i respectively, represent the angles between the ray path and the vertical axis (Figure 1). The free surface displacement, the intermediate boundary displacements and the displacement waves propagated downwards into the basement generated by a plane P or S wavefront incident on the crust from the basement are sought.

In this chapter the normal incidence wave propagation problem will be formulated first and then generalized to the non-normal problem. This approach should most simply demonstrate the essential nature of the formulation without obscuring the method in the details of the general problem. Time domain system descriptions will then be derived from these frequency formulations.

2.2 Linear Systems Approach

The linear system formulation describes wave propagation in terms of filter or communications theory. In this manner, the crust can be regarded as a filter system or communications channel which receives an

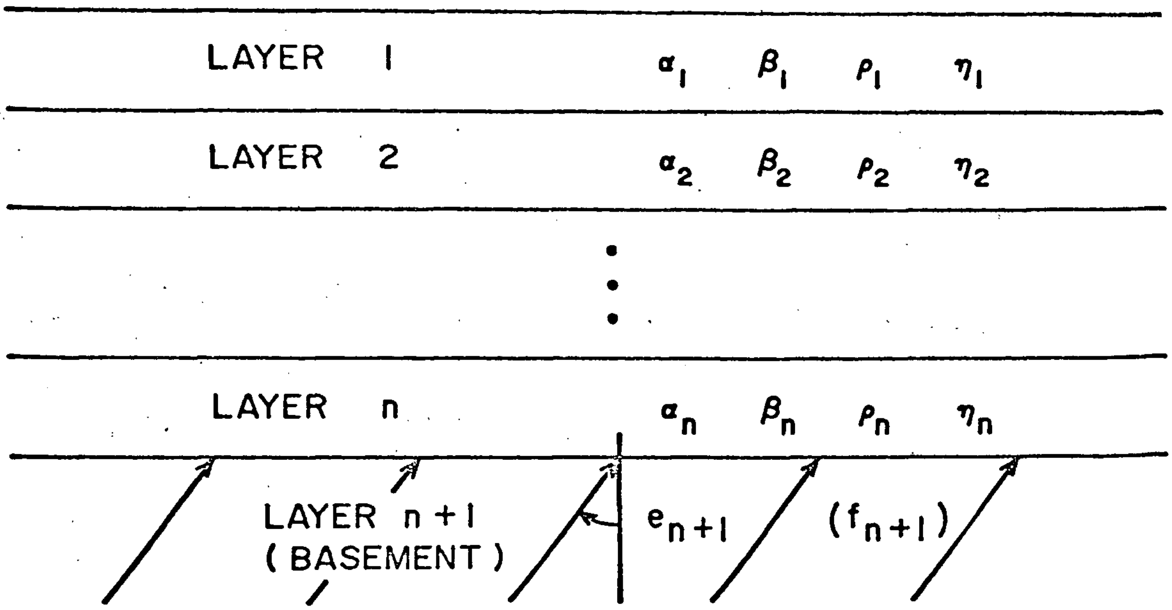

Fig. 1. The horizontally multilayered medium with n layers overlying a basement halfspace. Each layer i is specified by P- and S-wave velocities α_i and β_i; density ρ_i and thickness η_i. The plane wave from the basement is incident at angle e_{n+1} for P wave (or f_{n+1} for S wave).

input signal and operates on it to create the output signal (or the signal set in the case of many outputs). For crustal transmission the input is a teleseismic P or SV wavemotion incident on the crust at the basement boundary; the output signal set contains the cartesian coordinates of the free surface motions. The waveforms re-transmitted into the basement and all internal boundary motions are also available. These input-output relations can be block diagrammed as in Figure 2.

Under the assumption that the crustal response is linear, the response operator is independent of the input waveform. Thus, if two

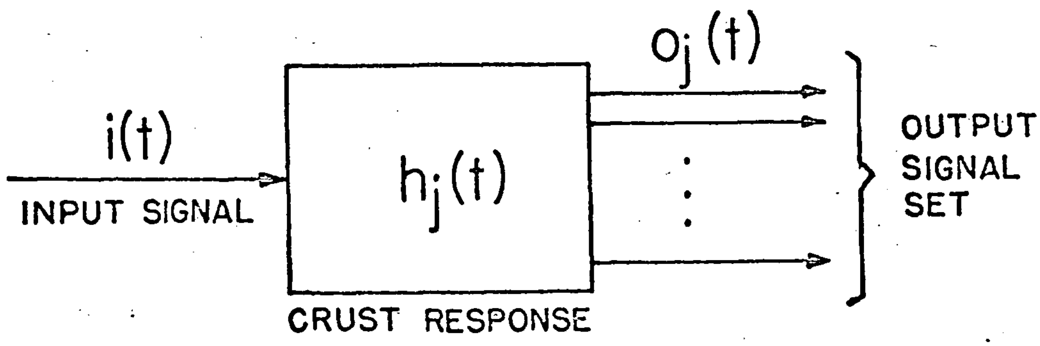

Fig. 2. The input-output diagram for a linear system crust. The output signal set $o_j(t)$ is obtained from the convolution of the input signal $i(t)$ with the crustal response vector $h_j(t)$.

among the input, the output set and the response operator are known, the third is uniquely determinable. In particular, if the input signal and response operator are known, the output signals can be calculated.

A filter system is often described in terms of the output signal set generated by specific input signals such as the Dirac delta function $\delta(t)$. This particular response is called the impulse-response function set of the system, $h_j(t)$. The output signal set $o_j(t)$ is obtained by the convolutions of the input signal $i(t)$ with the impulse response function vector $h_j(t)$:

$$o_j(t) = \int_{-\infty}^{\infty} i(t')h_j(t-t')dt' \qquad (2\text{-}1)$$

$$= i(t)*h_j(t) \quad .$$

For a linear system, an equivalent equation in terms of complex frequency components may be obtained by the Laplace integral transformation such that:

$$O_j(s) = I(s) \cdot H_j(s) \tag{2-2}$$

where $s = \sigma + i\omega$ is the complex frequency and the functions of the variable s designated with capitals are the Laplace transformed time functions,

$$\text{e.g.} \qquad I(s) = L\{i(t)\} = \int_0^\infty i(t)e^{-st}dt. \tag{2-3}$$

This representation relates the transformed input signal to the transformed output signal set by multiplication with the system transfer function vector at each complex frequency s. Both equations completely characterize the system and the parallel functions in the time and frequency domains are generally obtainable from each other through the Laplace transform and its inverse.

2.3 The Linear System Analog for Normal Incidence

The linear system analog for the simple case of normal incidence is now constructed to show the essential concepts. This restriction eliminates any conversions between compressional and rotational motions at the layer boundaries and limits the analog to two equivalent signal channels for each of the up and down-travelling P (or S) waveforms.

The multilayer linear system model may be developed in terms of individual layers as follows. On the boundaries of any one layer i, four possible input-output signals represent the up and down-travelling waveforms; the signals $u_i(t)$ and $d_i(t)$ represent the input displacement waveforms to layer i, while $u_{i-1}(t)$ and $d_{i+1}(t)$ represent the output

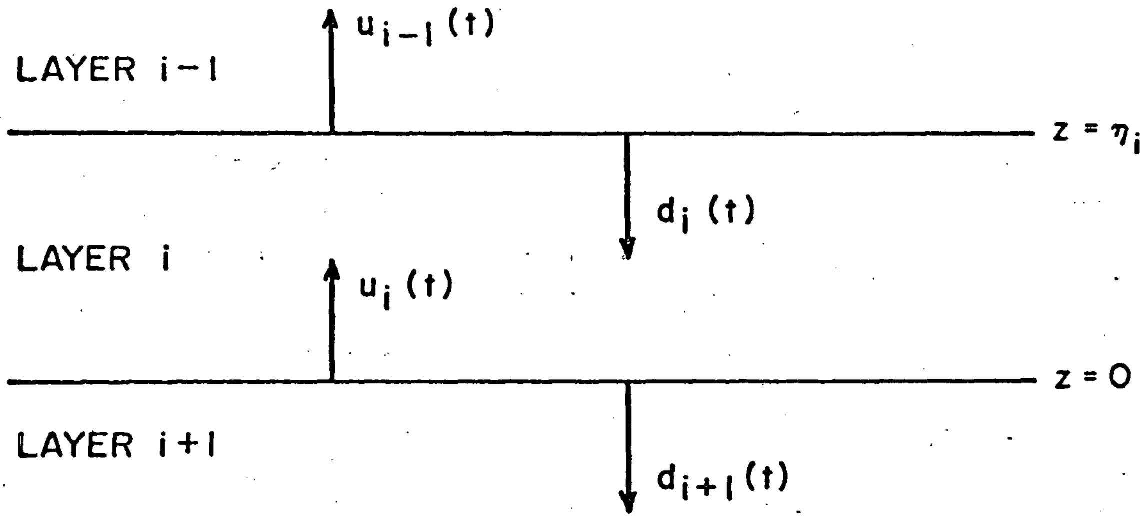

Fig. 3. A representation of the possible input and output waveforms in layer i under normal incidence.

waveforms from layer i and the equivalent input waveforms to layers i-1 and i+1 respectively (Figure 3). Between the boundaries, the up- and down-travelling waveforms are not coupled to each other because the propagation characteristics are assumed to be linear. However, these waveforms are linked at the boundaries by the standard displacement wave reflection and transmission coefficients. The four possible input-output signals are related through four impulse response functions, $h_{i_1}(t)$, $h_{i_2}(t)$, $h_{i_3}(t)$ and $h_{i_4}(t)$, representing the layer. These functions must be determined from the layer parameters. Convolution of the input signals and impulse response function pairs yields the output signals as follows: [1]

$$u_{i-1}(t)=h_{i_1}(t)*u_i(t)+h_{i_2}(t)*d_i(t)$$
$$d_{i+1}(t)=h_{i_3}(t)*u_i(t)+h_{i_4}(t)*d_i(t). \tag{2-4}$$

2.4 The Frequency Domain Description

It is convenient to determine these input-output relations in the frequency rather than the time domain by the Laplace (or Fourier) transform methods. The first equation above under the Laplace transformation becomes:

$$U_{i-1}(s)=H_{i_1}(s)U_i(s)+H_{i_2}(s)D_i(s)$$
$$D_{i+1}(s)=H_{i_3}(s)U_i(s)+H_{i_4}(s)D_i(s). \tag{2-5}$$

In this representation each impulse response function corresponds to a transfer function:

$$H_{i_k}(s) = L\{h_{i_k}(t)\} \tag{2-6}$$

and each time signal corresponds to a transform signal:

$$U_i(s) = L\{u_i(t)\} \quad . \tag{2-7}$$

[1] The existence of these convolution integrals demands that the transfer functions $H_{i_k}(s)$ are sectionally continuous. Any physically reasonable choice of reflection and transmission coefficients and the attenuation functions $A_i(s)$ will fulfill these requirements.

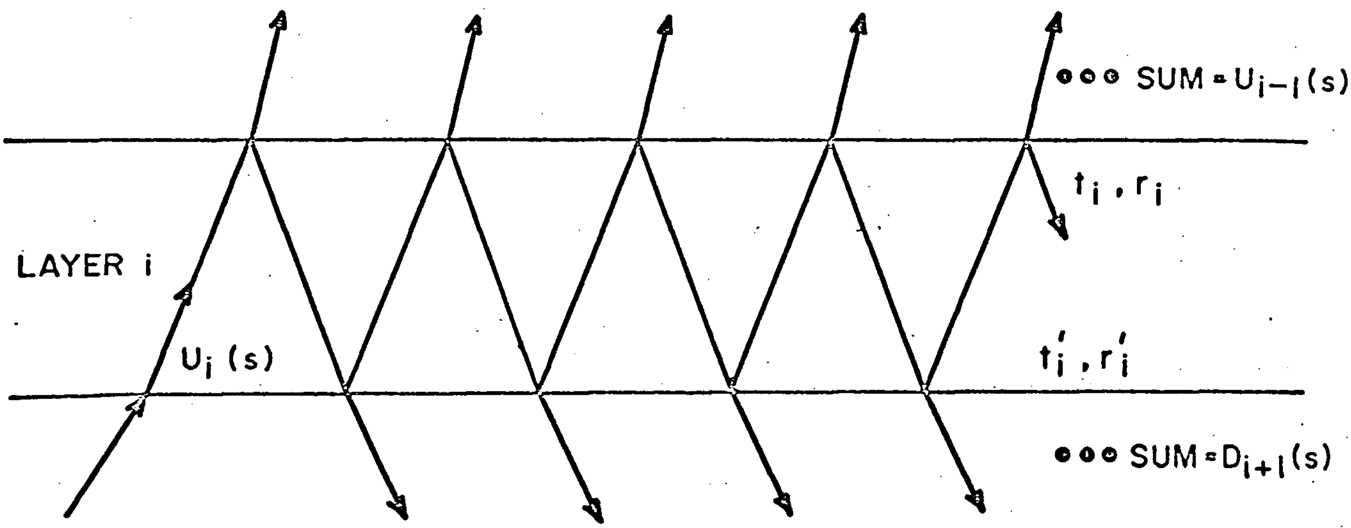

Fig. 4. A ray path representation of the internal reverberations within layer i giving rise to output transform signals $U_{i-1}(s)$ and $D_{i+1}(s)$. The transmission and reflection coefficients for the top and bottom boundaries are t_i and r_i and t_i' and r_i' respectively. This diagram represents the normal incidence condition; the diagram is expanded horizontally for clarity.

Direct calculation for the layer transfer function is possible on the basis of ray theory by the following procedure. Consider all reverberations due to an input P (or S) wave within a layer i (Figure 4). The transfer function $H_{i_1}(s)$ relating input signal $U_i(s)$ to output signal $U_{i-1}(s)$ may be determined as a series in which the first term represents the direct path transmission and each advancing term represents an increasing order of internal reverberation (1,2,3,...):

$$H_{i_1}(s) = t_i\{A_i(s)e^{-sT_i}+A_i^3(s)e^{-3sT_i}r_ir_i' + A_i^5(s)e^{-5sT_i}r_i^2r_i'^2+\ldots\} \tag{2-8}$$

where the displacement wave transmission and reflection coefficients at the upper and lower boundaries are represented by t_i, r_i and t_i' and r_i' respectively. $A_i(s)$ represents an arbitrary attenuation function of the complex frequency per single transit through the layer and T_i is the travel time through the layer determined by the wave phase velocity and layer thickness. The exact limiting sum of this series is:

$$H_{i_1}(s) = \frac{A_i(s)e^{-sT_i}}{1-A_i^2(s)e^{-2sT_i}r_ir_i'} \cdot t_i \tag{2-9}$$

$$= \frac{G(s)}{1-F(s)G(s)} \cdot t_i \tag{2-10}$$

where $G(s) = A_i(s)e^{-sT_i}$ and $F(s) = G(s)r_ir_i'$.

Similarly, the three remaining transfer functions for layer i are:

$$H_{i_2}(s) = \frac{G^2(s)}{1-F(s)G(s)} \cdot t_ir_i' \tag{2-11}$$

$$H_{i_3}(s) = \frac{G^2(s)}{1-F(s)G(s)} \cdot t_i'r_i \tag{2-12}$$

$$H_{i_4}(s) = \frac{G(s)}{1-F(s)G(s)} \cdot t_i' \quad . \tag{2-13}$$

These infinite series limiting sums consider all possible internal reverberation and ray paths within a layer for the normal incidence condition. The Laplace inversion of these transfer functions to obtain an equivalent set of time domain impulse response functions is discussed in Appendix I. A parallel formulation for S waves requires only the appropriate choice of the shear wave phase velocity and reflection and transmission coefficients.

The evident analogy of the form $\frac{G(s)}{1-F(s)G(s)}$ to the simple linear positive feedback network (Bohn, 1963) leads to a functional block representation of the linear system analog for the layer i (Figure 5). This system exactly diagrams all four layer transfer functions. For example, the input signal $U_i(s)$ enters the system at the lower boundary and circulates throughout the system as indicated by the arrows. The resulting output response signal $U_{i-1}(s)$ becomes the product of this input signal and the exact transfer function $H_{i_1}(s)$. Similarly, the three remaining transfer functions of layer i are described in the single diagram. Any number of such networks, each representing one layer can be combined to construct a total multilayer crust linear system network.

To completely determine the problem, input signals and free surface boundary conditions are required. The necessary input signal condition relates the incident waveform coming from the basement to the signal $u_n(t)$ in the bottom layer n:

$$u_n(t) = u_{INPUT}(t) \cdot t_{n+1} \quad . \tag{2-14}$$

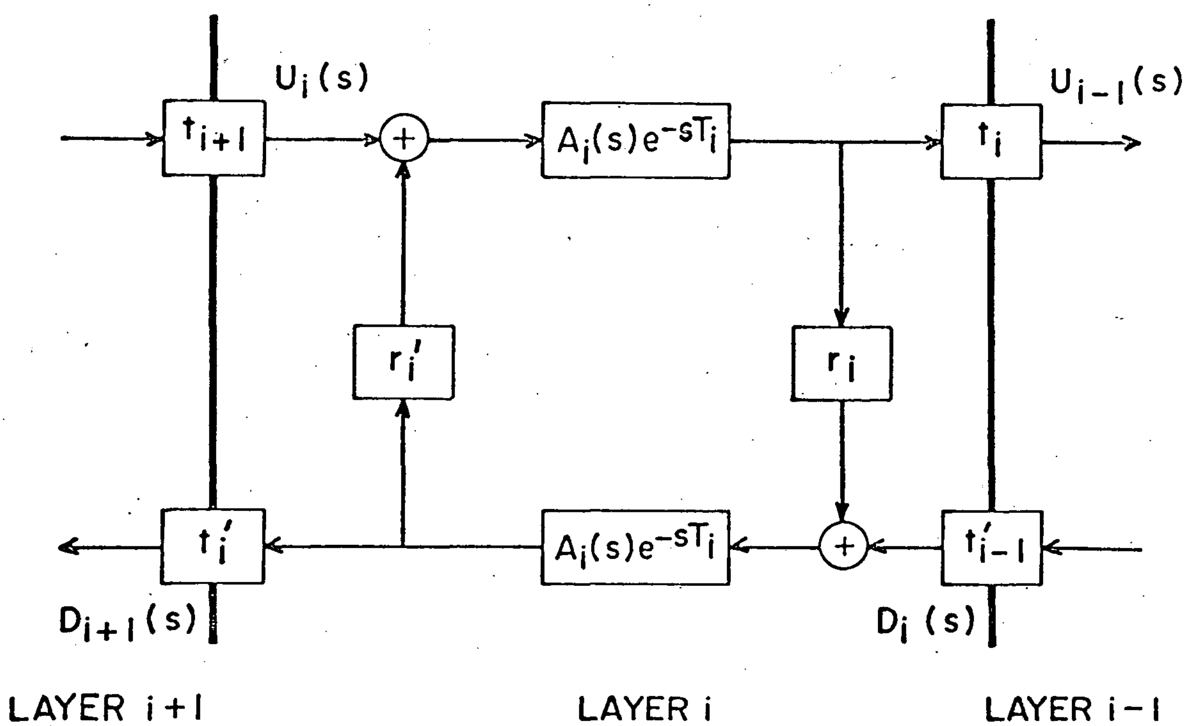

Fig. 5. A functional block representation of the linear system analog for layer i under normal incidence. The heavy vertical lines denote layer boundaries.

The corresponding transform signals are also similarly related:

$$U_n(s) = U_{INPUT}(s) \cdot t_{n+1} \quad . \tag{2-15}$$

The free surface boundary condition is included by the choice of the transmission coefficient $t_1=0$ and the signal $d_1(t)=0$ for layer 1. These two conditions imply that no wavemotion energy is lost or gained at the free surface boundary.

For the case of n layers above a basement halfspace, a set of 2n complex linear simultaneous equations in terms of the individual layer transfer function sets and the signals transforms represents the system:

$$
\begin{aligned}
U_1(s) &= H_{2_1}(s)U_2(s)+H_{2_2}(s)D_2(s) \\
U_2(s) &= H_{3_1}(s)U_3(s)+H_{3_2}(s)D_3(s) \\
D_2(s) &= H_{1_3}(s)U_1(s) \\
U_3(s) &= H_{4_1}(s)U_4(s)+H_{4_2}(s)D_4(s) \\
&\;\;\vdots \\
D_n(s) &= H_{n-1_3}(s)U_{n-1}(s)+H_{n-1_4}(s)D_{n-1}(s) \\
U_n(s) &= t_{n+1}\cdot U_{INPUT}(s) \\
D_{n+1}(s) &= H_{n_4}(s)D_n(s)+H_{n_3}(s)U_n(s)+r_{n+1}\cdot U_{INPUT}(s)
\end{aligned}
\tag{2-16}
$$

The solution of the problem requires the evaluation of each $U_i(s)$ and $D_i(s)$. Then, the desired surface vertical displacement amplitude transform $W_o(s)$ is related to the signal $U_1(s)$ by

$$W_o(s) = H_o(s)U_1(s) \quad . \tag{2-17}$$

$H_o(s)$ may be obtained from the block diagram for layer 1 (refer to Figure 5) noting that $t_1=0$, $r_1=-1$ and $D_1(s)=0$. The surface displacement signal, $W_o(s)$, is the sum of signals due to the incident and reflected waveforms at the free surface boundary. Since the reflection coefficient is -1, the two signals have opposite signs and directions so that the sum is twice the incident signal displacement amplitude. This incident signal is formed by $U_1(s)$ which has been delayed (multiplication by e^{-sT_1}), attenuated (multiplication by $A_1(s)$) and reverberated (divided by $1+A_1^2(s)r_1e^{-2sT_1}$) so that:

$$H_o(s) = \frac{2A_1(s)e^{-sT_1}}{1+A_1^2(s)r_1e^{-2sT}} \quad . \tag{2-18}$$

In cases involving only one or two layers, a solution by direct algebraic manipulations on the matrix of the functional coefficients is possible. However, for many layers, the analytical solutions for the transform surface motion and reflected signals and the subsequent Laplace inversion to give the output time domain response functions is not feasible. In lieu of the analytical approach, numerical solutions of the simultaneous equation set at incremented Fourier frequencies (obtained from the Laplace frequencies by setting $s=i\omega$) may be accomplished to give a steady state frequency response function for the multilayered medium. This more limited analysis corresponds to the Haskell matrix numerical computation for spectral responses. Results of such numerical analyses will be presented in a later chapter.

2.5 The Linear System Analog for Non-normal Incidence

The formulation for non-normal incidence plane waveforms proceeds analogously to that for normal incidence. However, immediate complication arises in the problem of handling conversions between compressional and rotational motions which occur at each layer boundary. Because such conversions occur, the independent P and SV motions must be considered separately requiring a four-channel rather than a two-channel analog approach (Figure 8).

For normal incidence, the waveform ray paths directly correspond to the positive and negative cartesian z directions, but for non-normal conditions, the ray paths are not coincident with the coordinate axes. Consequently, it is convenient to create a set of pseudo-coordinates in which the separate P- and S-wave motions effectively comprise the orthogonal vector pair (Figure 6). In each layer, the directions along the ray paths determine the required pseudo-coordinate set and are related to the cartesian coordinates by the angles between the normal and the P and S rays. It is evident that a different transformation is required for every layer. With horizontal layering, the compressional and shear motions throughout the medium possess a constant apparent horizontal phase velocity c determined by the input conditions. For example, for an input P-waveform from the basement:

$$c = \alpha_{n+1}/\sin(e_{n+1}) \tag{2-19}$$

where e_{n+1} is the P ray normal angle and α_{n+1} is the P phase velocity in the basement. Snell's law then determines the P and S ray angles with the normal in any other layer i:

$$c = \alpha_i/\sin(e_i) = \beta_i/\sin(f_i) \quad . \tag{2-20}$$

Up- and down-travelling waveforms are thus represented by the positive and negative directions of the two axes. The four possible directions on the two pseudo-coordinate axes determine the four required signal channels.

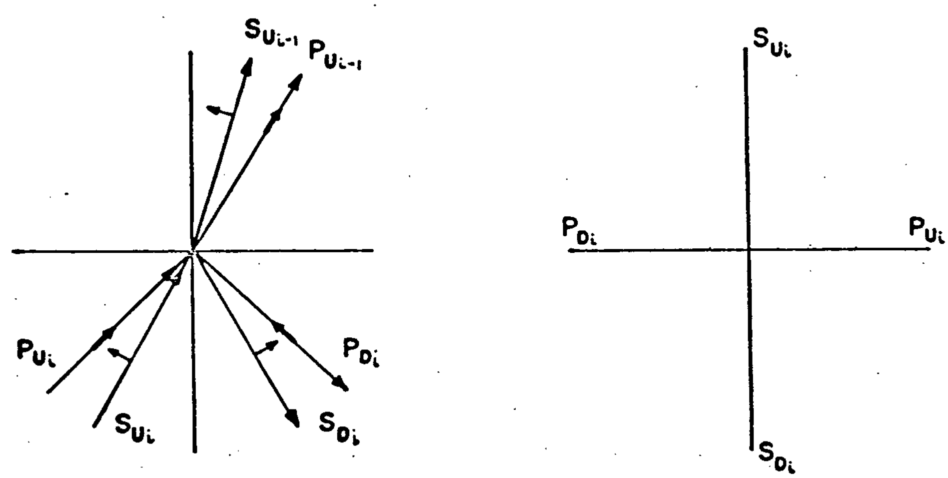

Fig. 6. A representation of the "pseudo-coordinate" transformation for layer i. The arrows on the rays of the cartesian representation show the positive displacement conventions used throughout this work. The pseudo-coordinate representation is for layer i only. The second diagram shows the P and SV displacements in layer i transformed into the pseudo-coordinate representation.

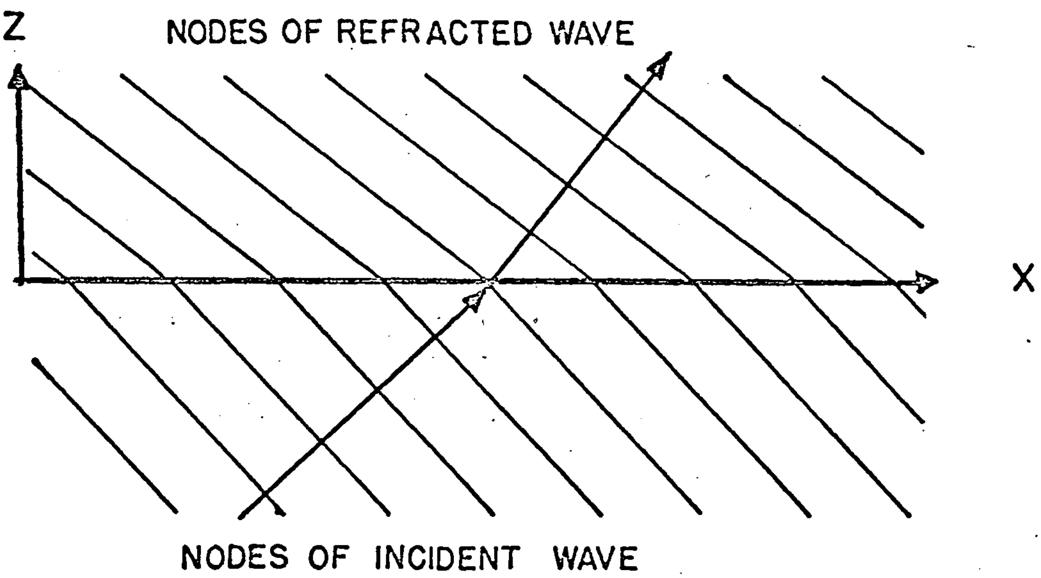

Fig. 7. A diagram showing the non-coincidence of wave constant phase positions (e.g. nodes) and a horizontal layer boundary.

A further complication arises for non-normal incidence because the phase of a plane wave is not constant along a boundary or along any surface of constant depth (Figure 7). For each layer i, the introduction of phase advance (negative time delay) transfer functions with the forms $e^{s\tau_{s_i}}$ for SV motions and $e^{s\tau_{p_i}}$ for P motions (Figure 8) to the linear system analog re-establish the correct phase relations for the signals at the boundaries. For a description and calculation of these phase advance transfer functions see Appendix II.

Just as each layer in the normal incidence problem was characterized by two equations in layer transfer functions and signals, each layer

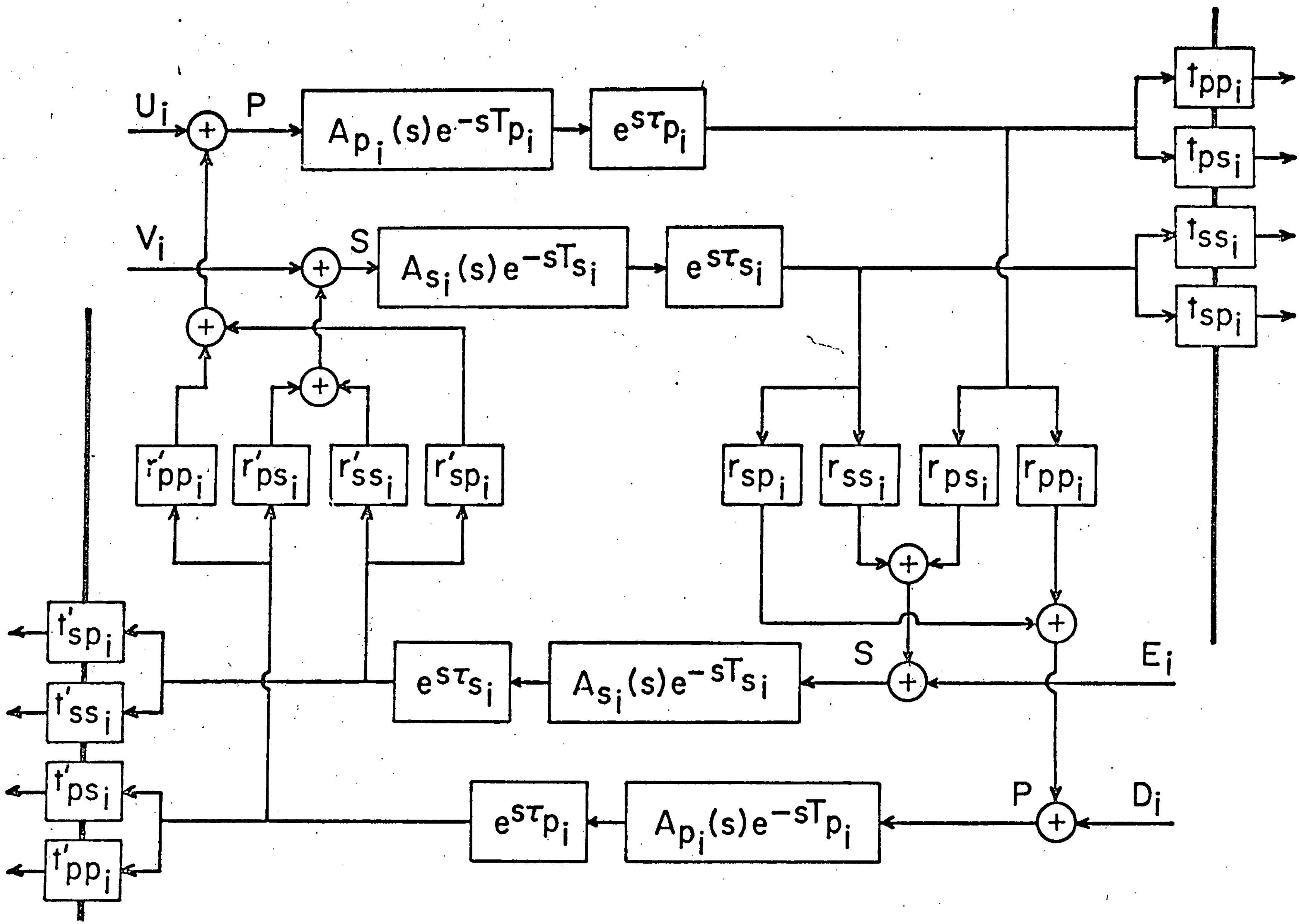

Fig. 8. A functional block representation for non-normal incidence for layer i. Note that four channels are shown, two for the up- and down-travelling P-waves and two for the up- and down-travelling SV waves.

in the non-normal problem is represented by four such equations; the transfer function relations for a layer i in a matrix form is:

$$\begin{bmatrix} U_{i-1}(s) \\ V_{i-1}(s) \\ D_{i+1}(s) \\ E_{i+1}(s) \end{bmatrix} = \begin{bmatrix} H_{i_1}(s) & H_{i_2}(s) & H_{i_3}(s) & H_{i_4}(s) \\ \bullet & \bullet & \bullet & \bullet \\ \bullet & \bullet & \bullet & \bullet \\ \bullet & \bullet & \bullet & H_{i_{16}}(s) \end{bmatrix} \cdot \begin{bmatrix} U_i(s) \\ V_i(s) \\ D_i(s) \\ E_i(s) \end{bmatrix} \qquad (2\text{-}21)$$

where the transforms $U_i(s)$ and $D_i(s)$ correspond to the up- and down-travelling P waves, the $V_i(s)$ and $E_i(s)$ correspond to the up- and down-travelling SV waves and the $H_{i_k}(s)$ are the transfer function set for the layer. A direct algebraic determination of these transfer functions is impractical. However, it is possible to construct directly the layer linear systems block diagram representation (Figure 8) by analogy to the normal incidence system and simplify it using "block diagram reduction procedures" (Kuo, 1962). One example reduction is performed in Appendix III. For frequency component analysis, such reductions are best accomplished during numerical analysis; for time domain analysis, reductions are unnecessary.

The equivalent linear system block representation of one layer for non-normal ray conditions contains four channels interconnected at the boundaries by the conversion reflection and transmission coefficients calculable using the Zoeppritz' displacement relations (Richter, 1958). For ray angles less than the critical angle, the sign of the real valued Zoeppritz' coefficients represents phase changes at refractions and reflections. Supercritical angles between the ray directions and the boundary normal angles determine complex transmission and reflection coefficients representing phase changes other than 0 and π. The linear system approach described in this thesis has not been extended to permit such supercritical conditions. Thus, trapped wave phenomena are not described.

In the functional block diagram of Figure 8, the subscript i refers to the layer i. The single subscripts p and s designate the separate channels for the P and SV waveforms; each functional block so indicated pertains only to the corresponding wave type. For example, $A_{p_i}(s)$ is the transfer function representing the attenuation of a P wave during one transit through layer i. The double subscripts of the Zoeppritz' coefficients indicate conversion from the waveform type indicated by the first subscript to the waveform type indicated by the second. For example, t_{sp_i} is the transmission coefficient which determines the conversion of S waves from layer i into P waves in layer i-1; $r_{pp'_i}$ is the reflection coefficient which determines the P wave to P wave reflection at the lower boundary of the layer i. The waveform types for the separate channels are indicated by P and S symbols. All other symbols retain the definitions of the normal incidence case.

An n-layered non-normal incidence problem requires the solution of 4n complex linear simultaneous equations formed similarly to those discussed in the normal incidence problem:

$$U_1(s) = H_{2_1}U_2(s)+H_{2_2}V_2(s)+H_{2_3}D_2(s)+H_{2_4}E_2(s)$$

$$V_1(s) = H_{2_5}U_2(s)+H_{2_6}V_2(s)+H_{2_7}D_2(s)+H_{2_8}E_2(s)$$

$$D_2(s) = H_{1_9}U_1(s)+H_{1_{10}}V_1(s)$$

$$E_2(s) = H_{1_{13}}U_1(s)+H_{1_{14}}V_1(s)$$

$$U_2(s) = H_{3_1}U_2(s)+H_{3_2}V_2(s)+H_{3_3}D_2(s)+H_{3_4}E_2(s)$$

$$V_2(s) = H_{3_5}U_2(s)+H_{3_6}V_2(s)+H_{3_7}D_2(s)+H_{3_8}E_2(s)$$

$$\vdots$$

$$D_n(s) = H_{n-1_9}U_n(s)+H_{n-1_{10}}V_{n+1}(s)+H_{n-1_{11}}D_{n-1}(s)+H_{n-1_{12}}E_{n-1}(s)$$

$$E_n(s) = H_{n-1_{13}}U_{n-1}(s)+H_{n-1_{14}}V_{n-1}(s)+H_{n-1_{15}}D_{n-1}(s)+H_{n-1_{16}}E_{n-1}(s)$$

$$U_n(s) = t_{pp_{n+1}}U_{INPUT}(s)$$

$$V_n(s) = t_{ps_{n+1}}U_{INPUT}(s) \tag{2-22}$$

$$D_{n+1}(s) = H_{n_9}U_n(s)+H_{n_{10}}V_n(s)+H_{n_{11}}D_n(s)+H_{n_{12}}E_n(s) + r_{pp_{n+1}}U_{INPUT}(s)$$

$$E_{n+1}(s) = H_{n_{13}}U_n(s)+H_{n_{14}}V_n(s)+H_{n_{15}}D_n(s)+H_{n_{16}}E_n(s) + r_{ps_{n+1}}U_{INPUT}(s)$$

The necessary free surface boundary conditions are included by the free surface Zoeppritz' reflection coefficients and the requirement that no wavemotions enter from the vacuum halfspace (i.e. $D_1(s)=E_1(s)=0$). The required input conditions relate the incident signal from the basement to the input signals at the lower boundary of the bottom layer n. For example, the input condition transforms generated by an input SV wave are: [2]

$$U_n(s) = t_{sp_{n+1}} \cdot V_{INPUT}(s)$$
$$V_n(s) = t_{ss_{n+1}} \cdot V_{INPUT}(s) \tag{2-23}$$

A solution requires evaluation of all signals $U_i(s)$, $D_i(s)$, $V_i(s)$ and $E_i(s)$ which are unspecified by either the boundary or input conditions. A following functional operation then relates the P and SV motions incident on the free surface boundary to the signals $U_1(s)$ and $V_1(s)$ obtained from the solution of the 4n simultaneous equations:

$$U_o(s) = H_{o_1}(s)U_1(s)+H_{o_2}(s)V_1(s)$$
$$V_o(s) = H_{o_3}(s)U_1(s)+H_{o_4}(s)V_1(s) \tag{2-24}$$

where $U_o(s)$ is the P and $V_o(s)$ the SV surface incident motions. The set of $H_{o_k}(s)$ are obtained by reduction procedures on the functional block

[2] If S waves with arbitrary polarization determine the incident waveform, the two dimensional analysis is not strictly valid. However, any S motion can be separated into SV (vertical polarization) and SH (horizontal polarization) components. The response to each component can be calculated separately.

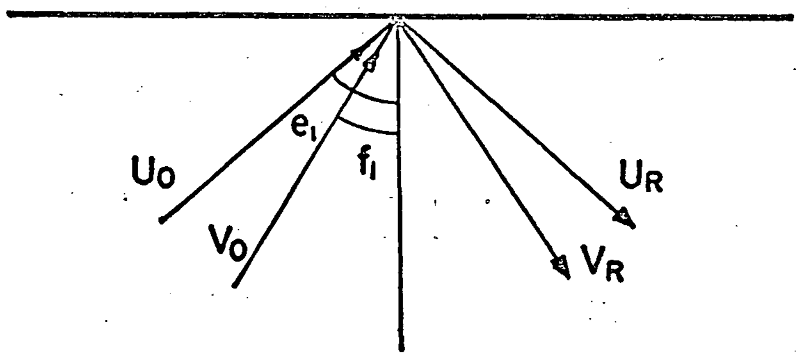

Fig. 9. The free surface reflection for non-normal incidence. U_o and V_o are the incident P- and S-waves and U_R and V_R are the reflected P- and S-waves.

representation of layer 1 considering the free surface boundary conditions in a manner similar to the normal incidence case. Then, the surface motion transforms, vertical component $W_o(s)$ and horizontal component $Y_o(s)$, are obtained by re-combination of the displacement components in the cartesian z and x directions due to the P and SV waveforms incident on and reflected from the free surface (Figure 9). The reflected transform signals, $U_R(s)$ and $V_R(s)$, are related to the surface incident signals by the Zoeppritz' free surface reflection coefficients:

$$U_R(s) = U_o(s)\cdot r_{pp_1} + V_o(s)\cdot r_{sp_1}$$

$$V_R(s) = U_o(s)\cdot r_{ps_1} + V_o(s)\cdot r_{ss_1} \quad . \tag{2-25}$$

The surface displacement amplitude coefficients are then:

$$W_o(s) = [U_o(s)+U_R(s)]\cos(e_1) + [V_o(s)+V_R(s)]\sin(f_1)$$

$$Y_o(s) = [U_o(s)-U_R(s)]\sin(e_1) - [V_o(s)-V_R(s)]\cos(f_1) \tag{2-26}$$

Because the algebraic forms of the transfer functions are so complex, even the simple one layer system is not readily soluble analytically. Again, numerical methods with incremented real frequencies are most easily used to determine the spectral response of the medium.

2.6 Time Domain Formulation

A development of the time domain systems description is now derived from the parallel frequency description for normal incidence conditions. The generalization to permit non-normal incidence is not described explicitly, but the complete system analog is presented. The transform approach described earlier is often used in the analysis of system response characteristics. However, for digital analyses, transform methods can be less efficient (in terms of computer time and storage requirements) if little convolution is necessary for a direct time domain solution.

Two direct approaches to a time domain linear systems solution exist. First, the system of linear simultaneous equations in terms of the signal transforms and layer transfer functions (Equations 2-16, 2-22) can be transformed into the equivalent system of linked convolution integrals. This system of equations in convolutions may be solved by standard numerical procedures for solution of integral equations using digital computers. (e.g., Carnahan et al, 1969). However, the approach has some drawbacks as each layer requires sixteen equivalent convolutions in the general non-normal case. For non-attenuating conditions, each of the sixteen required impulse responses for each layer is an infinite impulse train with decreasing impulse amplitudes with increasing time (Figure 10). The rate of the decrease of amplitude depends upon the reflection coefficients at the two layer boundaries. Efficient computation using digital methods requires finite (and preferably short) convolutions which necessitates the truncation of the infinite duration impulse responses. However, for accuracy, the truncated impulse responses must be at least as long as the time required for several waveform transits through the layer in order that the reverberation properties of each layer are well characterized. With the inclusion of attenuation the layer impulse response functions are no longer simple impulse trains but rather each impulse is broadened by the preferential low-pass nature of attenuation and the attending dispersion (Figure 10). This broadening increases with time at a rate determined by the layer Q.

The second approach which is computationally more efficient and used in this work accomplishes a time domain formulation in terms of system block representations by analogy to the frequency descriptions of Figures 5 and 8. Each frequency domain system block transfer function corresponds to an equivalent time function which can be directly obtained from the frequency function through the inverse Laplace transform. The time domain system descriptions of Figures 11 and 12 have been obtained

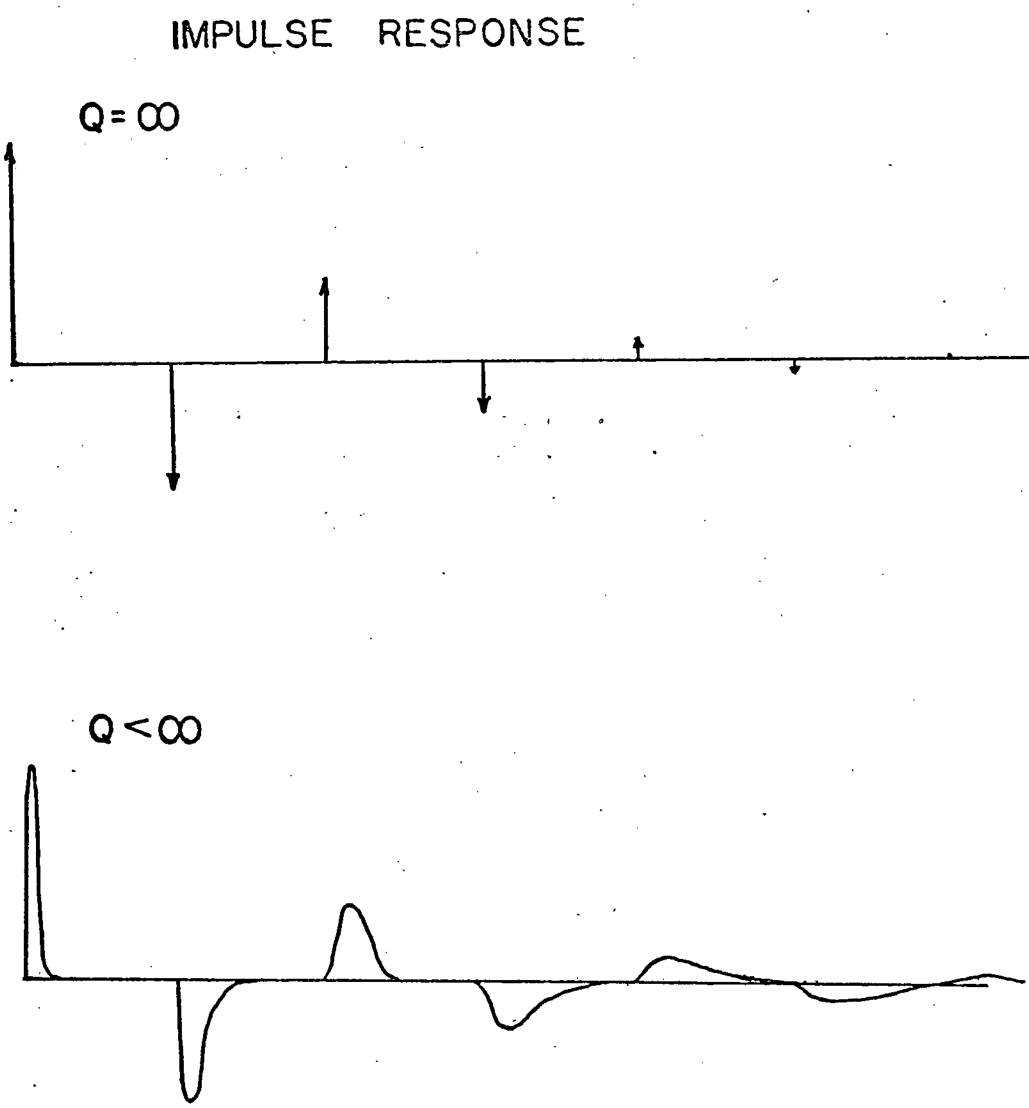

Fig. 10. A comparison of a normal incidence layer impulse response for infinite Q and causally absorbing conditions.

in this way. For example, for layer i at normal incidence the frequency domain delay and absorption transfer function $a_i(s)e^{-sT_i}$ (Figure 5) is inverse Laplace transformed to give the equivalent time domain delay and absorption function $\delta(t-T_i)*a_i(t)$ (Figure 11) where $a_i(t)$ describes the impulse response of the layer per single transit determined by the layer

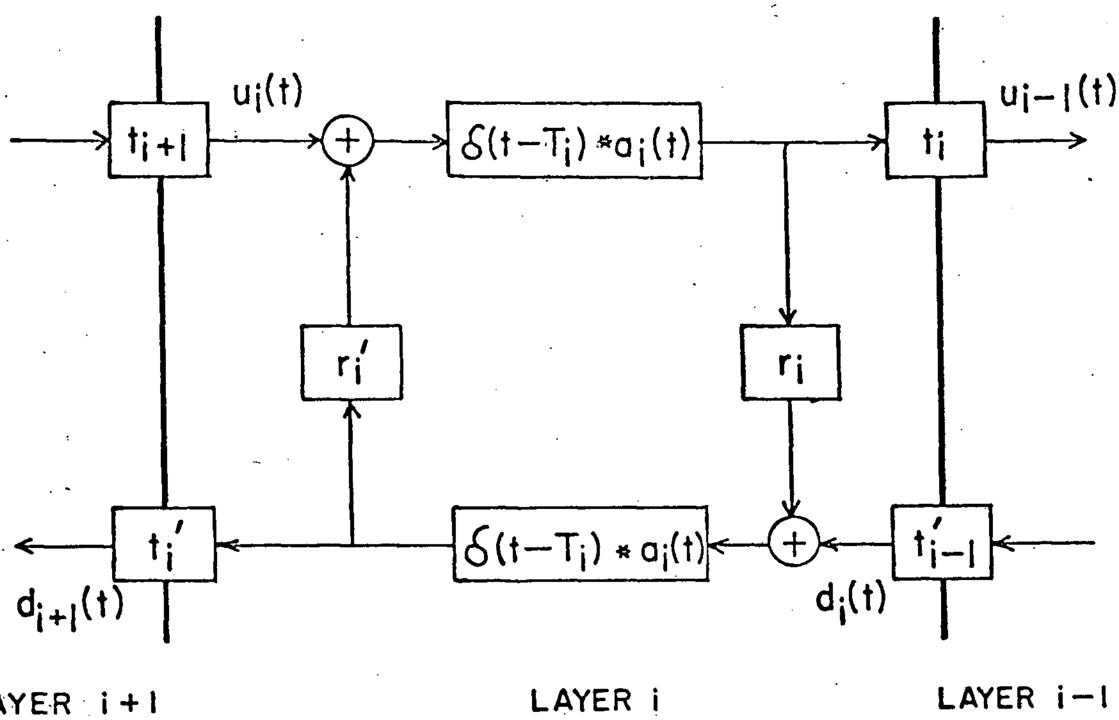

Fig. 11. The time-domain representation of the system analog of one layer at normal incidence. Compare to the frequency representation of Figure 5.

absorption properties. (The form of this absorption function is discussed later in this chapter).

To describe the essential nature of the time domain description, the normal incidence formulation (Figure 11) is now further demonstrated. At the lower boundary of layer i, a waveform $u_i(t)$ enters the system. This waveform combines by addition to any waveform $u_r(t)$ which results

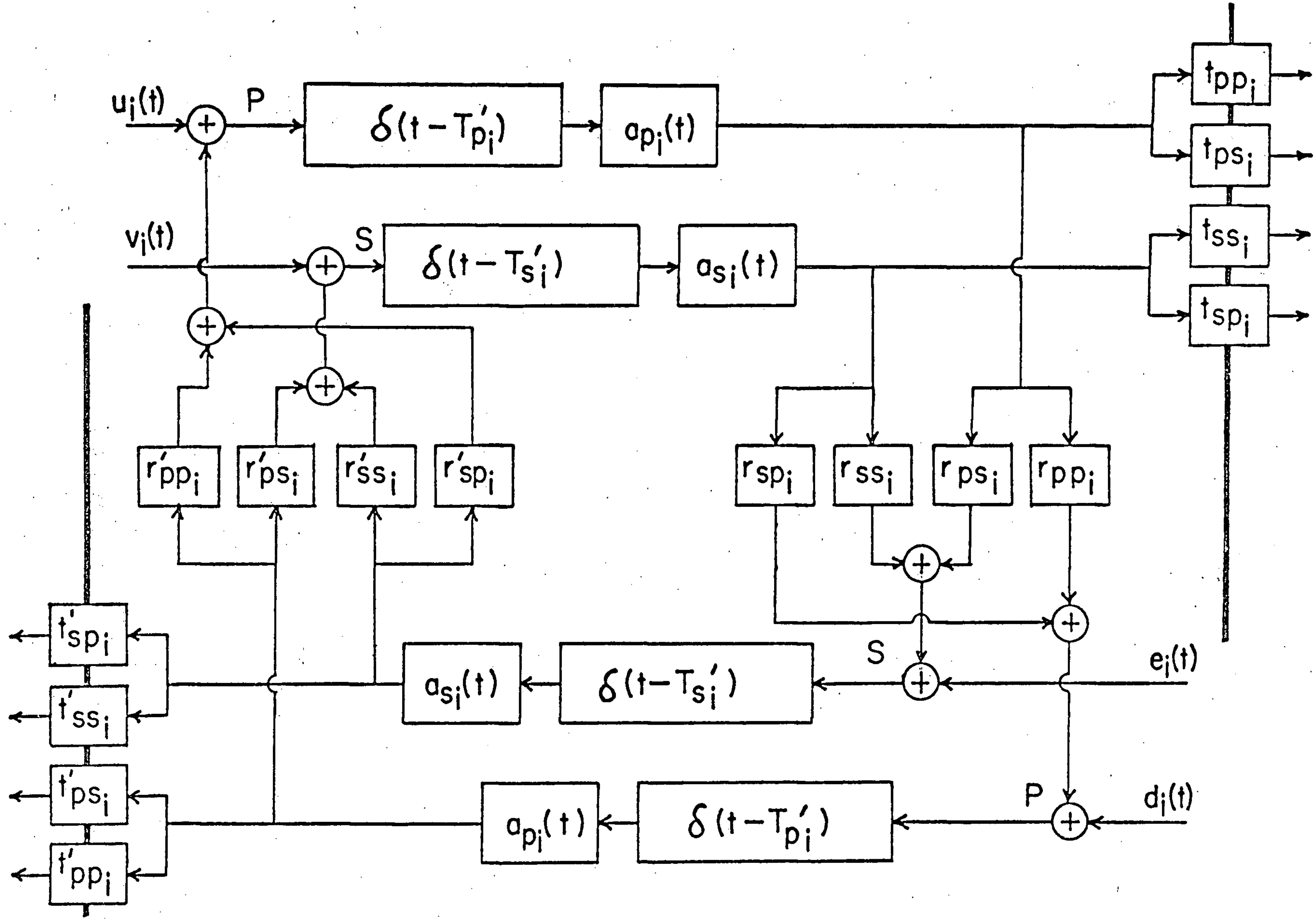

Fig. 12. The time-domain representation of the system analog of one layer for non-normal incidence. Compare to Figure 8.

from the reflection of any down-travelling wave at the lower boundary. $u_r(t)$ is the output signal from the system block r_i' which represents the lower boundary reflection coefficient. The sum waveform is then delayed by the delay operator $\delta(t-T_i)$ and absorbed according to the function $a_i(t)$ during its transit to the top boundary so that the equivalent waveform incident on the top boundary is:

$$\begin{aligned} y_i(t) &= (u_i(t)+u_r(t))*\delta(t-T_i)*a_i(t) \\ &= (u_i(t-T_i)+u_r(t-T_i))*a_i(t) \quad . \end{aligned} \tag{2-27}$$

If the layer possesses no internal attenuation:

$$a_i(t) = 1 \quad , \tag{2-28}$$

and

$$y_i(t) = u_i(t-T_i)+u_r(t-T_i) \quad . \tag{2-29}$$

The remaining system blocks are merely constants describing the other reflection and transmission coefficients at the layer boundaries and are identical to those of the frequency domain system. For example, the waveform $y_i(t)$ incident at the top boundary of the layer is partially transmitted into the next layer through the transmission coefficient t_i to form $u_{i-1}(t)$:

$$u_{i-1}(t) = t_i \cdot y_i(t) \quad . \tag{2-30}$$

$y_i(t)$ is also partially reflected back into layer i to form $d_r(t) = r_i \cdot y_i(t)$ which combines by addition to any input down-travelling waveform $d_i(t)$.

This combined waveform is delayed and absorbed during its transit to the lower boundary to form:

$$x_i(t) = (d_i(t-T_i)+d_r(t-T_i))*a_i(t) \quad . \tag{2-31}$$

$x_i(t)$ is partially reflected at the lower boundary to form $u_r(t) = r_i' \cdot x_i(t)$ which again combines by addition to $u_i(t)$ entering the layer at the lower boundary.

For normal incidence, only two convolutions with the attenuation and delay operator are necessary for each layer; four are required for non-normal incidence. If attenuation is not present, the form of these convolutions simplifies to mere delays of the input waveforms. Then only the past histories of the input function must be retained for a duration equal to the transit time.

Two linked integral equations thus describe the normal layer responses:

$$\begin{aligned} u_{i-1}(t) &= t_i[u_i(t-T_i)+ \frac{r_i'}{t_i'} d_{i+1}(t)]*a_i(t) \\ d_{i+1}(t) &= t_i'[d_i(t-T_i)+ \frac{r_i}{t_i} u_{i-1}(t)]*a_i(t) \quad ; \end{aligned} \tag{2-32}$$

a similar set of four equations describe the non-normal case.

For digital time simulations, each operator and signal within the system model must be time incremented. Then, for time incremented solutions (simulations) of the n-layered crust response to an input waveform, a set of 2n linked equations of the above form must be solved.

(4n such equations describe non-normal incidence). As in the frequency formulation, the necessary input conditions are determined by the input signal at the basement boundary; the correct free surface reflection coefficients determine the required boundary conditions. For the digital simulation, it is important to choose the constant time increment to be small enough as to prevent aliasing of the system frequency response or the spectral character of the input waveform due to sampling.

2.7 Attenuation and Dispersion in the System Model

Elastic wave attenuation in an absorbing medium is usually described in terms of the material Q factor (Knopoff, 1964). For a Q constant at all frequencies, a spatial absorption factor $\alpha(\omega) = \frac{\omega}{2Qc}$ determines the decreasing amplitude of an harmonic wave with distance:

$$U(x,\omega) = U(o,\omega)\exp(-\alpha(\omega)x) \quad . \tag{2-33}$$

If the absorption function is real and the phase velocity c is independent of frequency a non-physical acausal attenuation law results. Futterman (1962) extended this description of attenuation to allow the principle of causality to hold while retaining the essential linear nature of the absorption (Q remains constant in frequency) and wave motion in order that superposition remains valid. Subsequent analyses by Wuenschel (1965) demonstrated that Futterman's theory well described attenuation in real materials.

Under the condition of causal attenuation, a plane wave having travelled through distance x can be represented by a superposition integral in terms of the origin Fourier coefficients:

$$u(x,t) = \int_{-\infty}^{\infty} U(o,\omega)\exp(i[K(\omega)x-\omega t])\,d\omega\ , \text{ [3]} \tag{2-34}$$

where $K(\omega) = k(\omega)+i\alpha(\omega)$.

$K(\omega)$ also describes the dispersion properties of the material. For Futterman's model (A1,D1) which is used in later analyses $K(\omega)$ has the form:

$$K(\omega) = \begin{cases} \frac{\omega}{c}[1- \frac{1}{2\pi Q}\ \ln\left|(\frac{\omega}{\omega_o})^2-1\right|+i(\frac{1}{2Q})] & \omega > \omega_o \\ \\ \frac{\omega}{c} & \omega \leq \omega_o \end{cases} \tag{2-35}$$

where ω_o is an arbitrary cutoff angular frequency below which Q can be considered to be infinite. For frequencies well above ω_o, Futterman shows that the dispersed wave phase $v(\omega)$ and group $u(\omega)$ velocities are related to the limiting undispersed phase velocity c by:

$$v(\omega) \cong u(\omega) \cong c(1- \frac{1}{\pi Q}\ \ln(\frac{\omega}{\omega_o}))^{-1} \tag{2-36}$$

c, thus describes a lower velocity limit on an inverse dispersion condition. The absorption transfer functions and impulse responses which are required by the linear systems formulation are described by this attenuation model. For the time domain system:

---

[3] The integral representation for Fourier superposition in this case is that normally used in wave propagation problems. Throughout the rest of this thesis, the communications theory convention is used.

$$a_i(t) = \int_{-\infty}^{\infty} \exp(i[K_i(\omega)\eta_i - \omega t])d\omega \tag{2-37}$$

where η_i is the thickness of layer i and $K_i(\omega)$ the complex propagation function determined by the layer Q, phase velocity and the cutoff frequency ω_o. This $a_i(t)$ is the Futterman model impulse response (i.e. $U(o,\omega)=1$) of the layer. The equivalent frequency description (for the frequency domain linear system analog) in Fourier terms is:

$$A_i(\omega) = \exp(iK_i(\omega)\eta_i) \quad . \tag{2-38}$$

If the causal property for attenuation is not required (i.e. no phase information is desired) then the Futterman absorption function can be simplified to the usual acausal form:

$$A_i(\omega) = \exp(\frac{-\omega T_i}{2Q_i}) \tag{2-39}$$

where Q_i is the layer Q value and T_i the layer transit time.

It should be noted that the Futterman analysis of attenuation requires ω_o and c. In practice, however, the dispersed phase velocity $v(\omega)$ and group velocity $u(\omega)$ are the observable quantities while ω_o and c must be obtained by calculation. Because the form of the absorption impulse response function $a_i(t)$ is only weakly dependent upon the actual cutoff frequency, ω_o can be chosen arbitrarily to be very small compared to the frequencies of interest. Futterman's choice of $\omega_o=10^{-3}$ sec^{-1} has been used in the computation of the absorption functions used later in this thesis.

In the preceding discussion, the absorption transfer function, $A_i(\omega)$, and the absorption time function, $a_i(t)$, can represent either P-wave or S-wave attenuation. It is only necessary to specify the particular transit time and Q corresponding to the wave type to determine the frequency or time function desired.

The transmission-reflection conditions at a flat boundary between two causally absorbing media are affected by the coincident dispersion of the elastic waves. Because the velocity ratios between the two media are not necessarily constant at all frequencies, each Fourier component observes transmission and reflection coefficients which are different from the non-dispersed case. The velocity ratios also determine the ray directions of the transmitted frequency components by Snell's Law. If the ratios are not constant, the transmitted frequency component ray directions are not all coincident and a geometrical condition on dispersion results. In a frequency domain analysis, this dispersion property is not a major problem because transmission and reflection coefficients and ray directions can be computed for each Fourier component frequency. However, in a time domain approach, the separation of frequency components cannot be accomplished and the method becomes an approximation of the true solution. Wuenschel's (1965) analysis of attenuation and dispersion in the Pierre Colorado shales suggests that the frequency dependence of the dispersed phase velocity is small over frequency ranges of several octaves. Consequently, a constant transmission-reflection coefficient and ray direction approximation appears to be valid and is assumed in the following analyses.

CHAPTER III

ANALYSIS OF THE ALBERTA SEISMOGRAMS

3.1 Introduction

In order to demonstrate the unique features and utility of this theory, the results of analyses of seismograms recorded in central Alberta will be compared to linear systems solutions in both time and frequency domains. The effects of crustal attenuation on spectral ratios will be shown to be significant for the low Q values which are thought to characterize crustal sediments. It will be observed that the correlation between experiment and theory is best at frequencies below 1 Hz. Time domain synthetic seismograms will also be calculated by the systems approach and compared with experimental recordings. The effects of crustal attenuation and the assumed form of the incident wavelet will be shown. Although exact syntheses have not been obtained, significant similarity with experiment will be evident.

The primary aim of the thesis has not been to determine the Alberta crust, but rather to develop the new linear systems technique and demonstrate its particular usefulness. Thus, the nature of each of the following experimental analyses is basically one of example.

3.2 The Analysis Problem

The character of the P coda of a seismogram depends upon: a) the source generated waveform, b) the physical properties of the source to receiver paths such as Q, mantle layering, and the near receiver crustal structure and c) the response characteristics of the recording instruments. This last effect can be well determined by the calibration of the seismograph system. The combination of the source waveforms and the mantle path effects determines the waveform incident on the base of the crust which is necessary for the solution techniques presented in this work.

The assumed linear nature of elastic propagation in the crust permits inverse approaches. For example, if a seismogram is known and the crustal response is linear and known, the corresponding input waveform can be directly computed. Also, from a known input signal and its resulting seismogram, the unique response of the crust to elastic waves can be obtained. However, since there is seldom any comparison information on the nature of the source or incident teleseismic waveforms, these inverse approaches are not useful to demonstrate the utility of the present theory without further assumptions. Rather, frequency and time domain propagation solutions will be compared with analyses of the experimental seismograms.

3.3 The Experiment

For analyses a chosen set of seismograms recorded south of Edmonton, Alberta during a field program of October and November 1968 has been used. Three portable FM tape recording short period seismograph stations at the University of Alberta Edmonton Seismological Observatory (our seismograph is designated LED in this thesis), and at the nearby Chamulka (CHA) and Larsen (LAR) farms (Figure 13) recorded 16 useful events from teleseismic distances. Six of these were chosen for analytical comparisons with the theory (see later Figure 16, Table III). This region of Alberta is characterized by a flatly bedded sedimentary

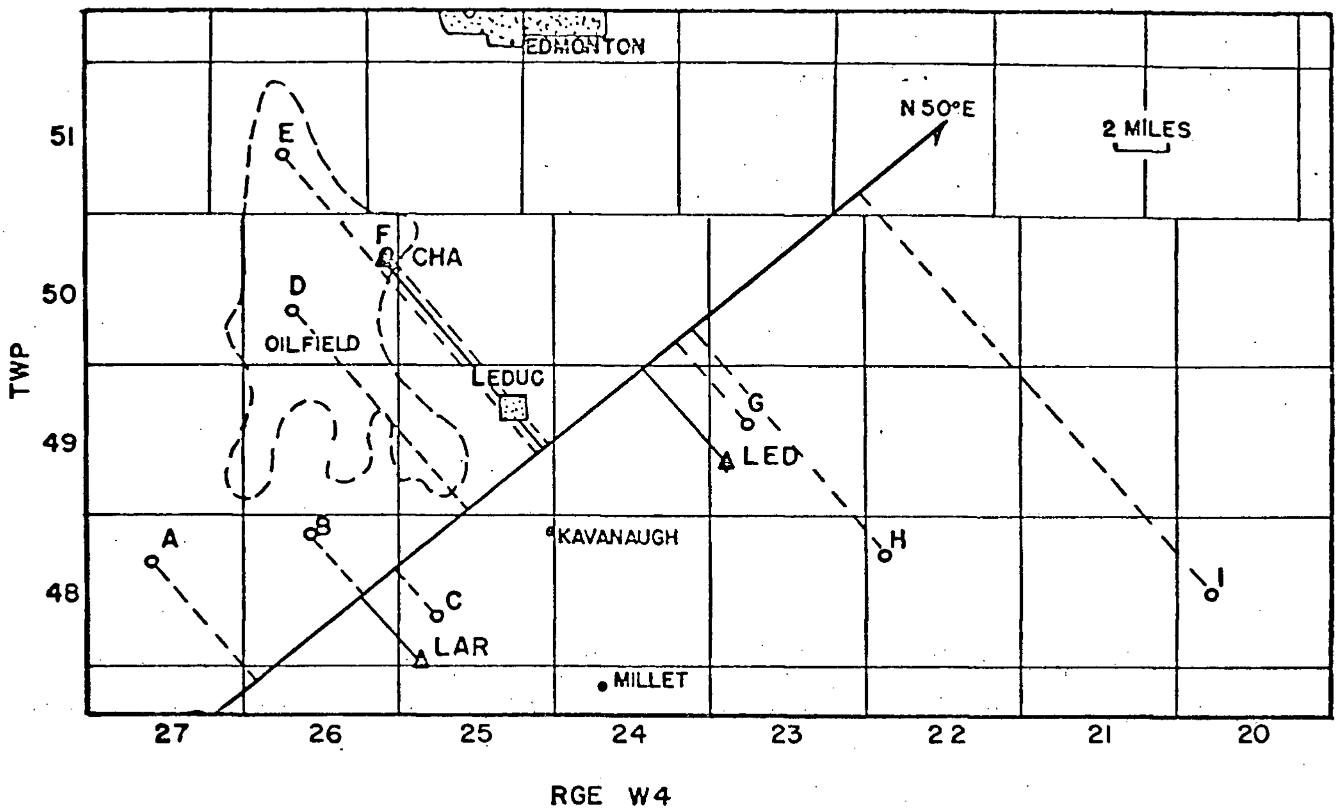

Fig. 13. A map of the seismic station and oilwell locations by which the crustal section was determined. The well sites are designated by letters and correspond to those of Figure 14. The Dominion Land Survey Range and Township coordinates are shown.

section which can in general be approximated by the horizontal layer model. Maximum dip angles on the notably continuous formation boundaries are generally less than 1^{o} except in anomalous areas such as the Leduc-Woodbend oilfield (which lies beneath station CHA) in which oil-bearing Devonian reef structures exist. Therefore, these records are ideally suited to this problem. Also, the sedimentary section is well known from reflection seismic surveys and oilwell borehole geophysics for several nearby drill sites.

3.4 The Crust Model

The station locations formed a triangular pattern 15 kilometers on a side. Over these relatively short distances, velocity and resistivity logs from deep oilwells in the vicinity permitted easy and certain correlations of the major sedimentary formations to determine an interpolated profile section for the upper crust (Figure 14, Table I). A regional downward dip normal to the Rocky Mountain strike in a direction N 130^{o}W was assumed in order to facilitate the interpolation between the well sites to the station locations. (e.g. Ellis and Basham, 1968).

In order to affect the character of a seismogram, a formation layer must have a thickness comparable to the wavelength of the highest frequencies recorded by the seismograph. More exactly, a linear systems solution shows that the fundamental reverberation frequency of a layer is determined by the imaginary component of the Laplace frequency s at the principal pole of the transfer function set (Appendix I). For a non-attenuating layer under normal incidence, this condition corresponds to one of two frequencies depending upon the reflection coefficients at the layer boundaries:

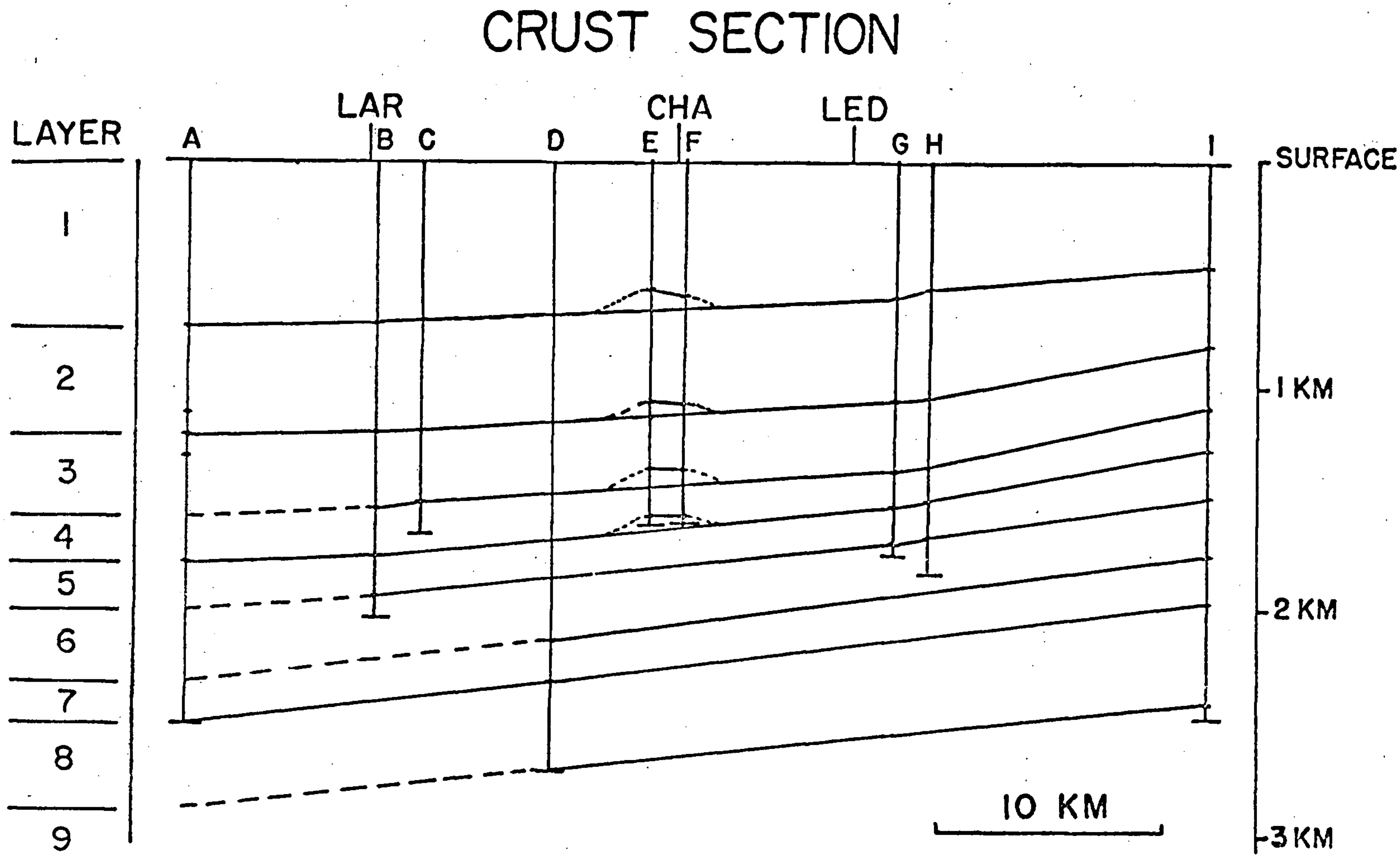

Fig. 14. The sedimentary crustal section obtained by interpolation between oilwell geophysical logs. The layer numbers correspond to those in Table I. The dotted boundaries underlying station CHA show the effect of the Leduc-Woodbend oilfield. The control oilwell sites used are designated by letters which correspond to those of Figure 13. Extrapolations are indicated by dotted lines.

either $$f_{o_i} = \frac{1}{2T_i}$$

$$\text{(3-1)}$$

or $$f_{o_i} = \frac{1}{4T_i}$$

where T_i is the layer P-wave (or S-wave) transit time. [4] Thus, f_{o_i} determines the minimum frequency component for which the layer reverberates; frequencies significantly lower than this are unseen. The sedimentary crust models (Figure 14, Table I) include all distinct layers for which the transit time, T_i, is greater than 0.05 seconds. Consequently, the layer modelling is sufficiently detailed to include the fundamental layer reverberation character for frequencies markedly less than 10 Hz. Furthermore, all other layer boundaries which showed notable velocity contrasts were also considered in the crustal models, thus allowing layers for which T_i approximates only 0.025 seconds (f_{o_i} = 20Hz). The frequencies recorded by the seismographs are limited to a band below 5 Hz. The crust model detail should be sufficient to describe reverberations in this band.

The subsedimentary crustal section included in the total crustal model of Table I follows the gross crust of Cumming and Kanasewich (1966) for southern Alberta. The total crust model is desirable since the Mohorovicic discontinuity first causes a part of an incident P wave to be converted into SV motions and particularly affects much of the early character of the horizontal seismograms.

---

[4] The first condition results if the product of the two reflection coefficients is positive; the second if the product is negative. Also for the positive product, there is a pole on the $\omega = 0$ axis (i.e. $f_{o_i} = 0$). This pole determines only the zero frequency character of the layer response and does not affect wave propagation (Appendix I).

TABLE I

CRUSTAL SECTIONS

LAYER	FORMATION (TOP)	THICKNESS (km)			P-VELOCITY (km/sec)			DENSITY (gm/cc)		
		LED	CHA	LAR	LED	CHA	LAR	LED	CHA	LAR
1	Post Alberta	0.62	0.58	0.71	2.7	2.7	2.7	2.2	2.2	2.2
2	Alberta	0.46	0.49	0.49	3.0	3.0	3.1	2.3	2.3	2.3
3	Blairmore	0.31	0.28	0.35	3.7	4.1	4.1	2.4	2.4	2.4
4	Wabumum	0.16	0.23	0.21	5.5	5.6	5.6	2.6	2.6	2.6
5	Ireton	0.17	0.22	0.19	4.0	4.2	4.5	2.4	2.4	2.5
6	Cooking Lake	0.26	0.27	0.30	5.3	5.4	5.5	2.6	2.6	2.6
7	Elk Point	0.19	0.19	0.18	4.6	4.7	4.7	2.5	2.5	2.5
8	Cambrian	0.42	0.40	0.37	4.1	4.2	4.2	2.4	2.4	2.4
9	Precambrian	10.0	10.0	10.0	6.1	6.1	6.1	2.7	2.7	2.7
10	Sub-Layer I	24.0	24.0	24.0	6.5	6.5	6.5	2.8	2.8	2.8
11	Sub-Layer II	11.0	11.0	11.0	7.2	7.2	7.2	2.9	2.9	2.9
12	Mantle Boundary	-	-	-	8.2	8.2	8.2	3.0	3.0	3.0

These model considerations do not exactly represent non-normal incidence as the fundamental resonance frequencies are slightly increased as the incident angle increases. But since the waveform incident angles are generally small for the teleseismic source distances, only small effects are to be expected.

Independent data on the layer S velocities, formation densities and elastic wave attenuation properties are not available for the Alberta crust. However, reasonably probable values for the S-wave velocities were determined assuming Poisson's ratio is 1/4 so that:

$$\beta_i = \alpha_i/\sqrt{3} \tag{3-2}$$

Formation densities were obtained from the P-wave velocity-density relation of Nafe and Drake (Grant and West, 1965).

Few results have been reported for the attenuation properties of body waves within the crust and among these little consistency is apparent. The studies of McDonal et al (1958) on the thick shale formations near Pierre, Colorado are among the most widely quoted. However, other in situ Q measurements by subsequent workers (e.g., Tullos and Reid, 1969) have not shown attenuation coefficients which closely agree with their results. Various authors (Press, 1964; Anderson et al, 1965) have inferred body wave Q's from surface wave analyses. But such studies do not provide the resolution required in the present analysis. Clowes and Kanasewich (1970) experimentally obtained Q for the central Alberta crust using deep reflection seismograms. They determined average Q near 300 in the sediments and approximately 1500 in the lower crust. Their sediment Q appears to be significantly greater than that found by

McDonal et al for similar materials. In fact, order of magnitude differences appear to be common among the several Q's reported for sedimentary crusts.

For this thesis, material Q values have been obtained from the literature (Knopoff, 1964; McDonal et al, 1958; Savage, 1965) and correlated with the known formation materials in the sedimentary portion of the Alberta crust. Within the lower crust, Q's have been estimated on the basis of the average crustal attenuation (Press, 1964). Comprehensive data on the composition of the Alberta sediments has been compiled by the Alberta Society of Petroleum Geologists (1964). Since most of the major formations are substantially homogeneous, the correlations between the formation rock material and published Q factors for the materials should give plausible values. Q has been reported to be approximately frequency independent over a wide range of frequencies between 1 Hz and 10^6 Hz (Knopoff and MacDonald, 1958 and 1960). Thus, Q factors which have been published for relatively high frequencies have been assumed to be constant to the Futterman cutoff angular frequency ω_o. Furthermore, at frequencies below 1 Hz, realistic Q values have almost no effect on body wave propagation in the crust and the assumption that Q is constant with frequency to the cutoff presents no apparent difficulties. Shear and compressional Q's have been assumed to be identical.

The crustal model Q factors for the individual layers which have been chosen for this work are tabulated and referenced in Table II. Of these, only those from the Alberta and post Alberta formations can be expected to be accurate. These formations are basically uniform shales which appear to be contiguous with the Pierre, Colorado shales for which

TABLE II

FORMATION Q's

FORMATION	MATERIAL	Q CHOSEN	Q APPLICABLE	REFERENCE
Post Alberta	sandy shale	23	23 (Pierre shale)	1,2
Alberta	shale	30	21-52	1
Blairmore	shale, sandstone	30	21-52	1
Wabumum	dolomite	100	45-190? (limestone)	1
Ireton	shale	30	21-52	1
Cooking Lake	limestone	100	45-190?	1
Elk Point	salt, evaporites	100	70-220 (hard chalk)	3
Cambrian	sandstones, clastics	50	52 (sandstone)	1
Precambrian	granite?	200	57-200	1
Sub-Layer I	-	500	-	estimated, 4
Sub-Layer II	-	500	-	estimated, 4

Q (average for whole crust) = 186: Q (average for sediments) = 40. The average Q's were computed considering the travel times through the individual layers.

References: 1) Knopoff (1964)
2) McDonal et al (1958)
3) Savage (1965)
4) Press (1964)

The validity of the Q's for the sub-sedimentary layers is questionable. The results of Press (1964) apply particularly to Pg waves in the tectonically active region of the Nevada Test Site. For the remaining chosen Q's, values obtained in the lab must be assumed to apply in situ.

attenuation properties are well known (Williams and Burk, 1964). McDonal et al (1958) obtained Q=23 for P waves and Q=10 for S waves with frequencies beyond 20 Hz in this formation. In order to conform to the Q assignments to other layers the Q=23 value has been assumed to describe the S wave attenuation in this layer also.

The average Q for the sedimentary portion of the crust above the Precambrian by the above model is approximately 40 while the average Q for the whole crust is near 200.

3.5 Data Preparation

The FM tape recorded seismograms were digitized with a sampling rate of 20 per second for the numerical analyses. The rapid falloff of the seismograph sensitivity from 5 Hz ensures that there is little seismogram content beyond the 10 Hz Nyquist frequency so that aliasing effects are minimal. Transient calibration pulses were recorded at the beginning of each 5-day tape record. From these pulses, the absolute ground motion amplitude frequency response of each station component seismograph was determined using the transient calibration procedure outlined by Deas (1969). However, the high frequency instrumental response character is poorly determined by this method since the digitization (quantization) noise swamps the high frequency components in the calibration pulses (Figure 15). Consequently, the theoretical response for frequencies beyond 2 Hz was assumed to be representative of the systems. The response characteristics of the three components of any one station were designed to be virtually identical; only the absolute sensitivities significantly varied between components. The results of the pulse calibrations were used to establish absolute sensitivities.

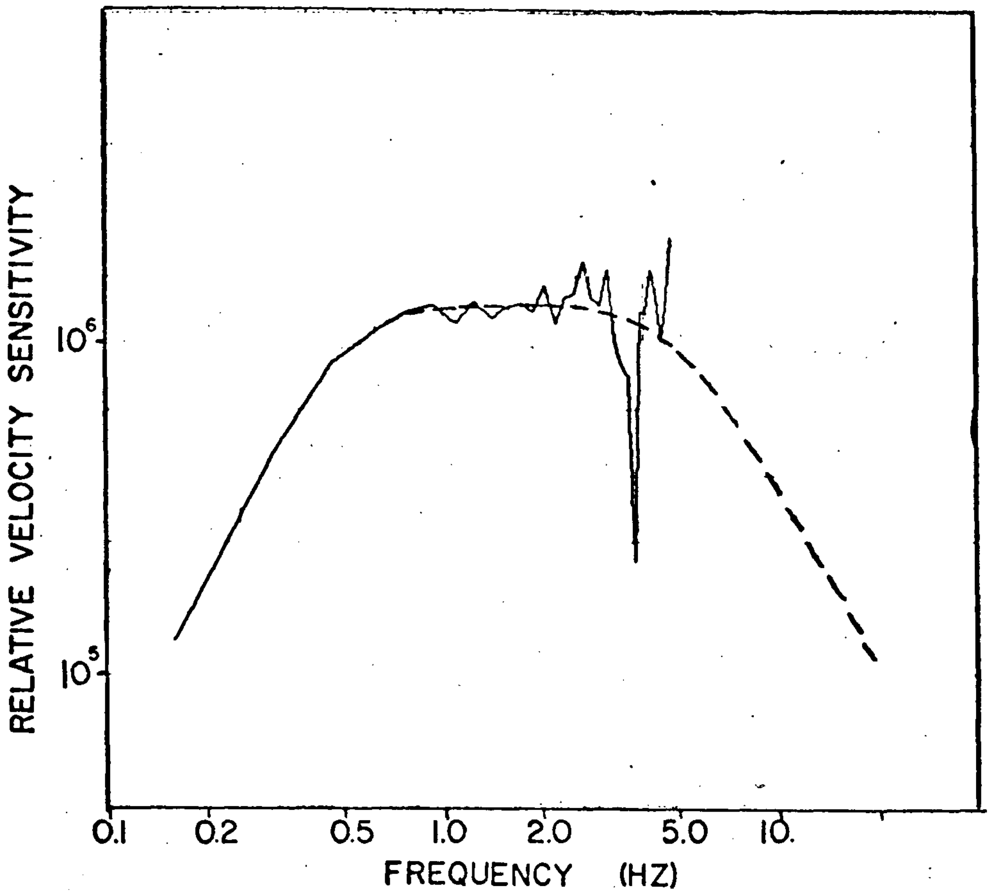

Fig. 15. The theoretical standard seismograph response (dotted line) compared to a response calibration obtained by the transient method (solid line).

The nature of the propagation problem is essentially two dimensional; motions only occur vertically and horizontally along the wave ray paths. For the comparisons of the theory with the seismograms, it is then necessary to perform a transformation on the N and E horizontal components to establish the equivalent radial component motion along the surface projection of the ray path and the transverse component normal to it. For transformation, the two horizontal seismogram components must have identical responses. For this purpose, all station component sensitivities were normalized to the response calibration of the vertical component of station LED on October 4, 1968. The absolute sensitivities of the instruments varied with time. Effects of temperature on the transistorized amplifiers and seismometers partially account for this effect.

3.6 The Seismograms

The six events used in these comparison analyses (Table III, Figures 16a-f) were chosen primarily for their short and apparently simple P coda. For these events, the wave motion incident on the base of the crust should comprise a basically transient P wave of short duration. If the source to receiver path is not structured in its elastic properties, P to S wave conversions do not occur along the path. However, it should be noted that distinct structure in the upper mantle and continuous velocity and density variations (hence acoustic impedance variations) along the source to receiver path must cause some conversion of energy from compressional to rotational motions. For these analyses, source generated P and S motions are assumed to arrive at the receiver several minutes apart with the incident waveform entirely compressional. The P coda is thus considered to be the result of the purely compressional waveform impinging on the base of the crust at the Mohorovicic discontinuity.

Ellis and Basham (1968) have suggested that an increase in the transverse component amplitude with time (this increase is observed for

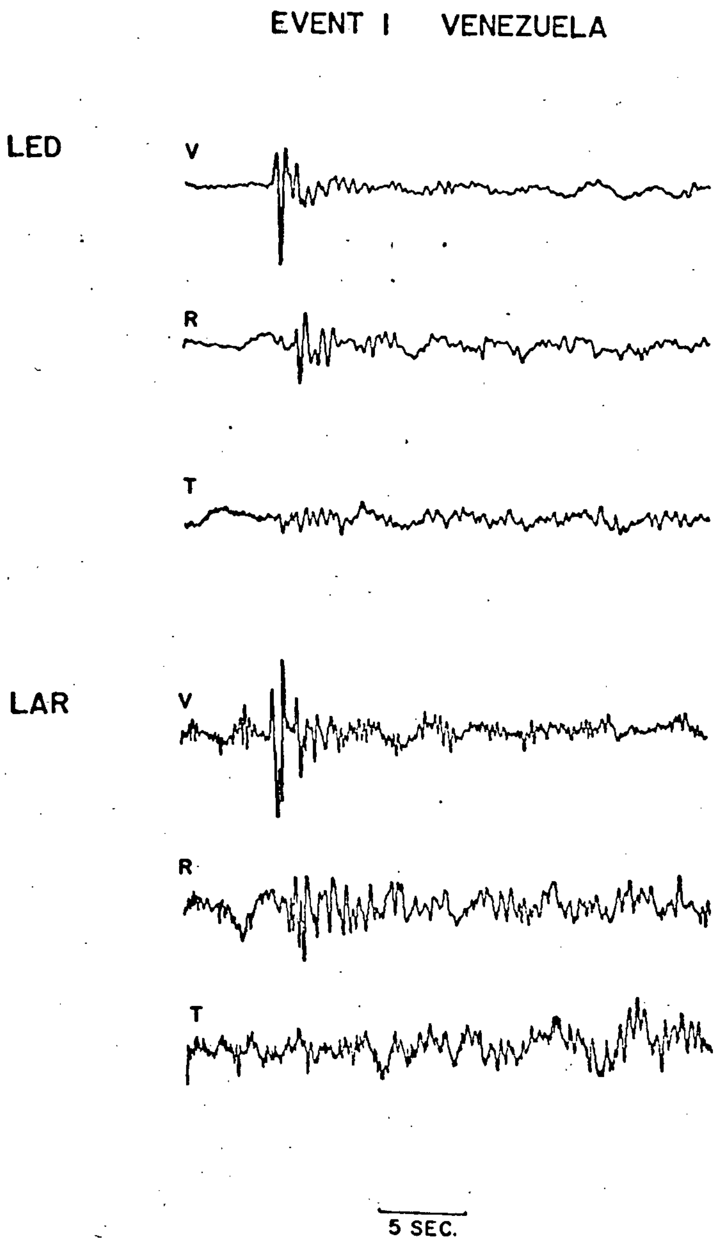

Fig. 16a-f. The vertical, radial horizontal and transverse horizontal components of the experimental seismograms for the events studied in this work. The P-coda onset for each event is exactly 5 seconds from the beginning of each record.

(a) Venezuela

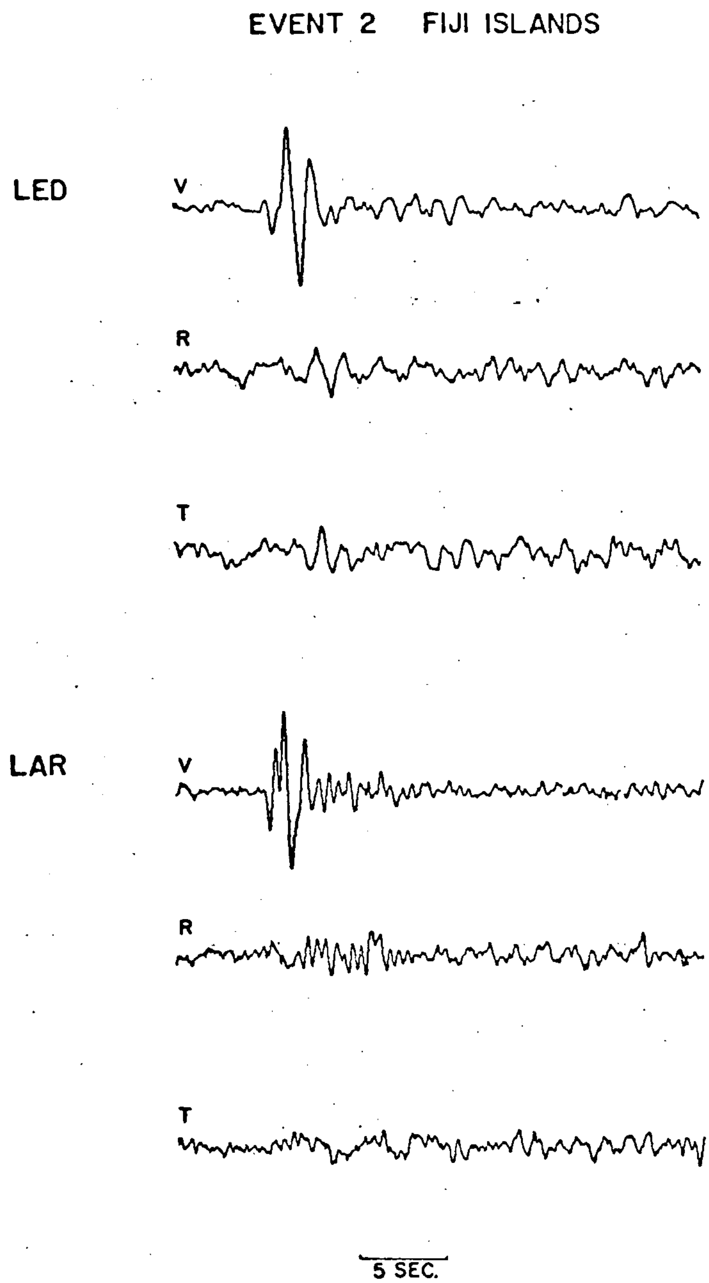

(b) Fiji Islands

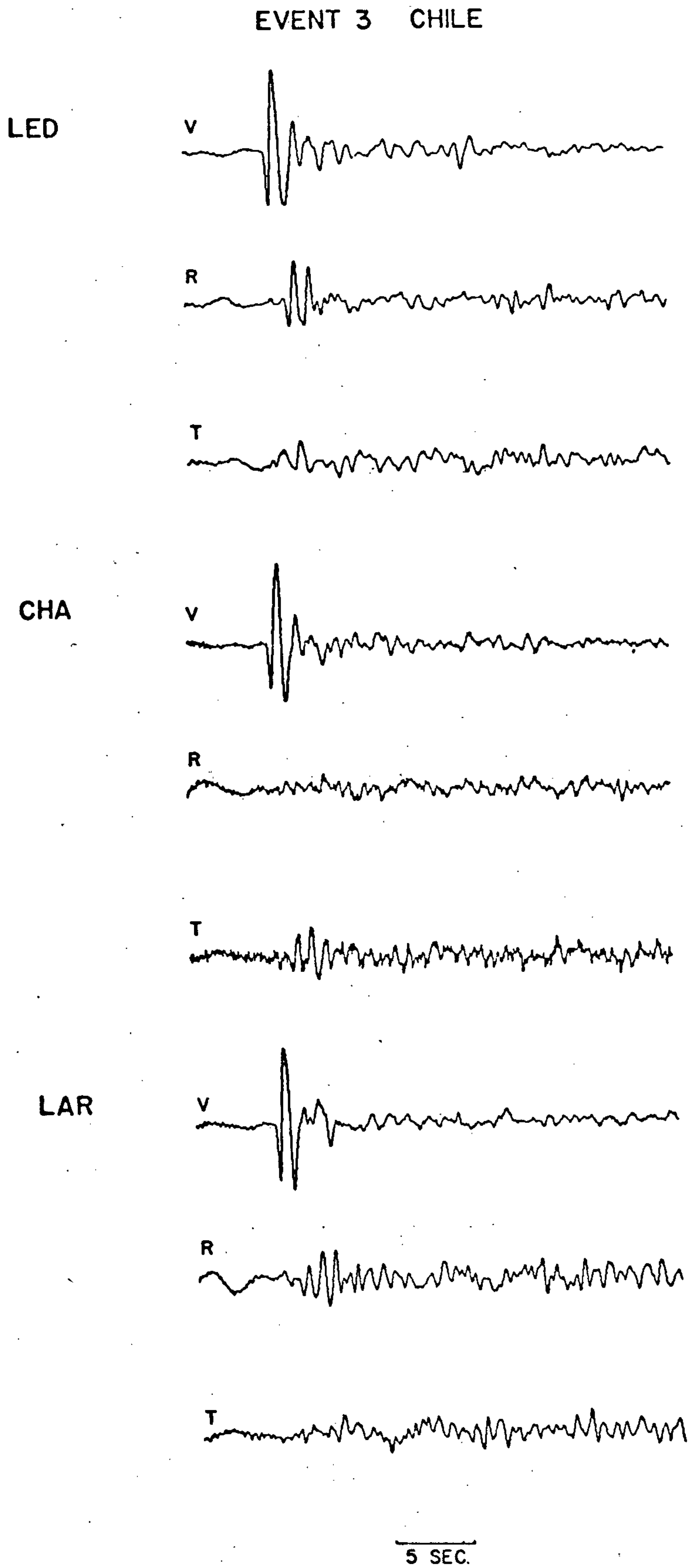

(c) Chile

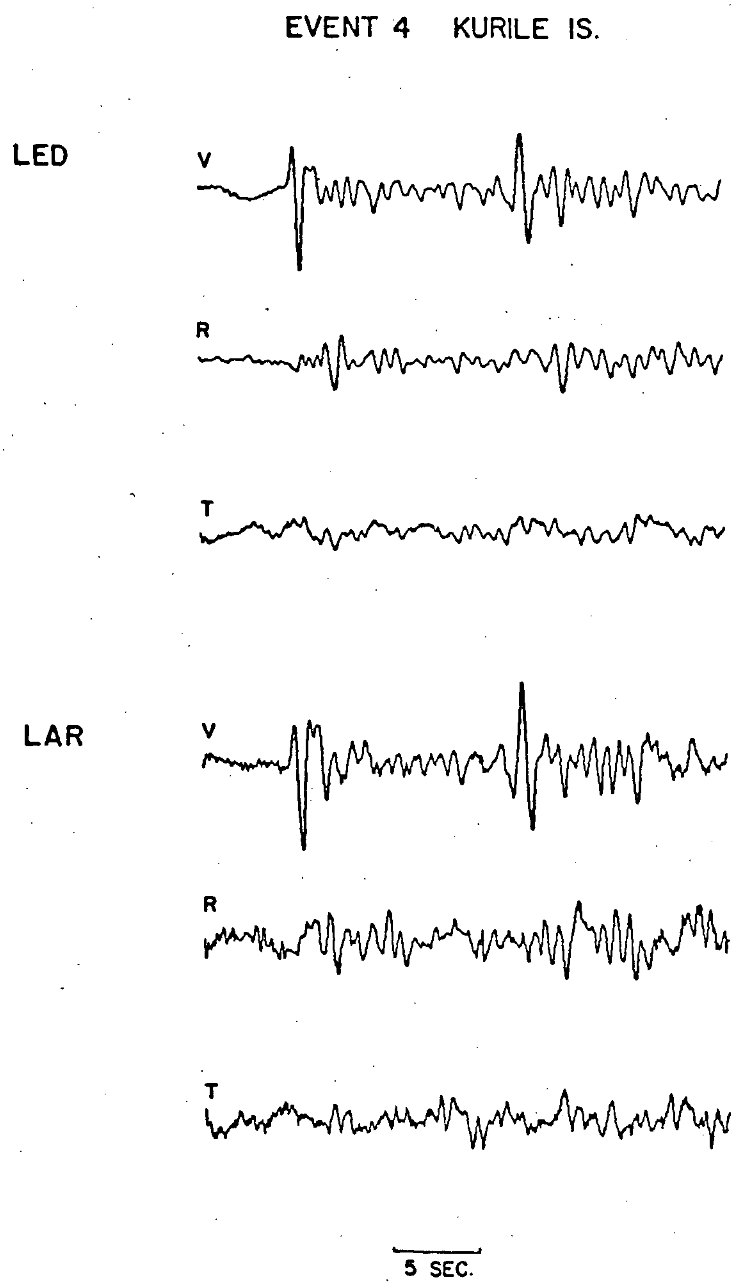

(d) Kurile Islands

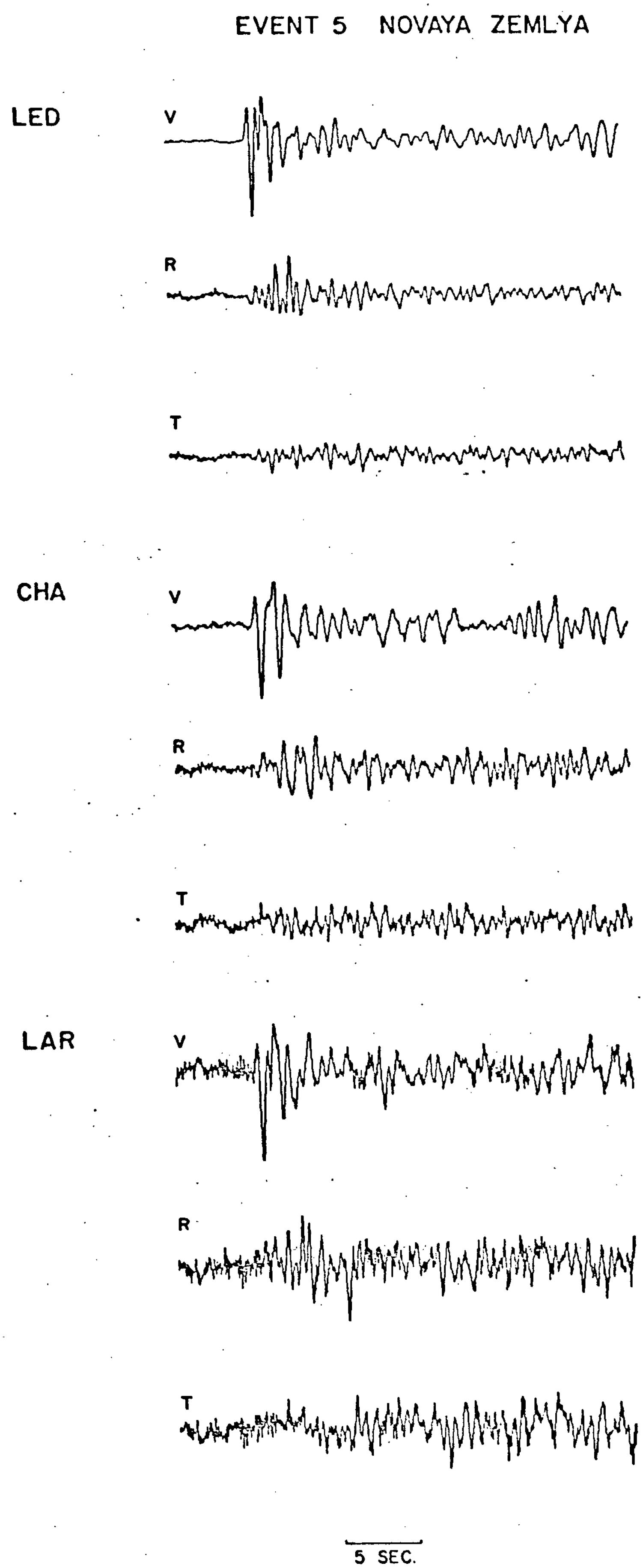

(e) Novaya Zemlya

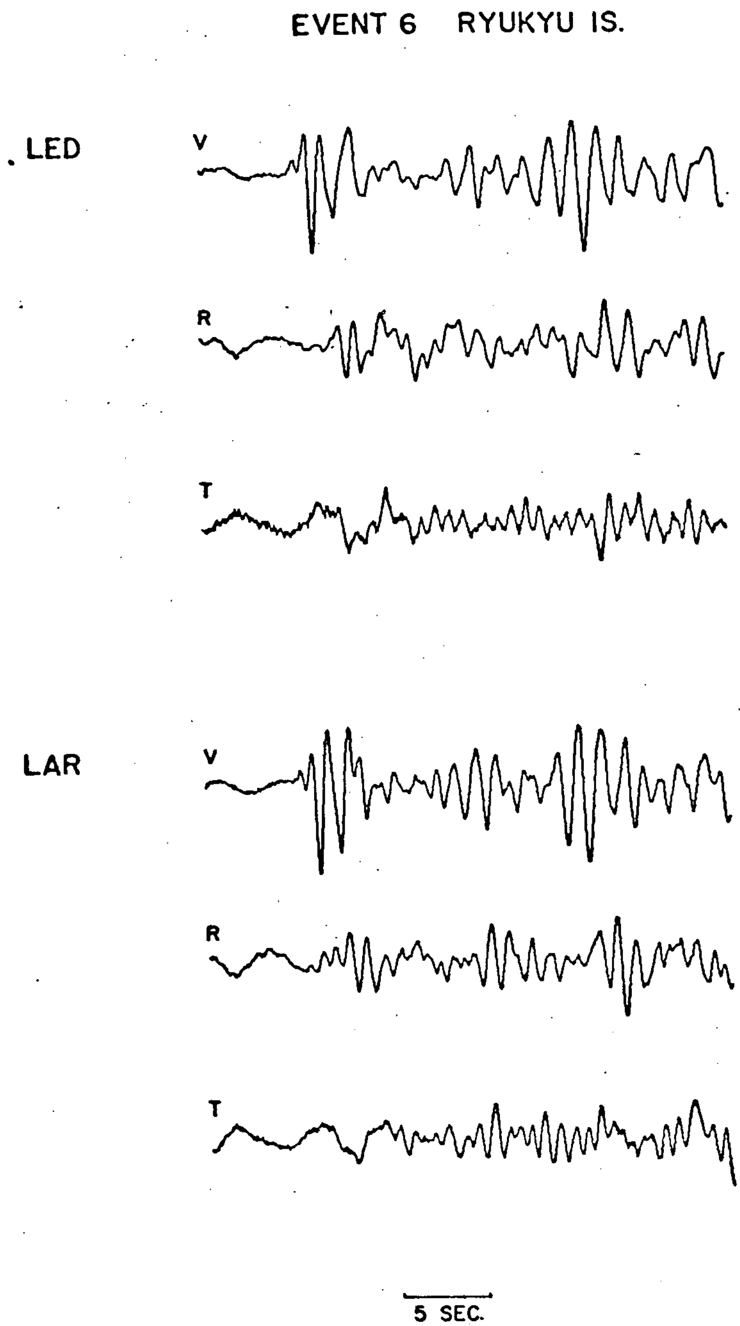

(f) Ryukyu Islands

TABLE III

EVENTS USED IN ANALYSES

EVENT	LOCATION	LAT	LONG	DEPTH	MAG	DELTA	INCIDENCE	AZIMUTH (S-E)
1	Venezuela	10.7°N	62.6°W	97 km	4.8	58.6°	30°	117° E of N
2	Fiji Is.	20.9°S	178.8°W	607 km	5.7	92.9°	19°	238°
3	Chile	19.6°S	68.9°W	107 km	5.3	82.1°	21°	138°
4	Kurile Is.	49.7°N	155.8°E	35 km	5.5	53.0°	31°	305°
5	Novaya Zemlya	73.4°N	54.9°E	0 km	6.0	53.4°	31°	4°
6	Ryukyu Is.	27.5°N	128.4°E	48 km	5.8	83.4°	21°	308°

example on the Venezuelan event recorded at station LAR in Figure 16a) may be due to signal generation of noise by scattering within the crustal layering or topographic features. This effect may then indicate the rate of degradation of the record for the purposes of this analysis. For most of the chosen events, the radial and transverse motion amplitudes become comparable within 15 to 30 seconds of the P onset. Twenty-five seconds of the record has been used in the subsequent frequency domain analyses of the seismograms. Generally, one would not expect the noise generated transverse amplitudes to exceed the radial amplitudes for horizontally layered structures. However, some records such as the CHA seismograms from the Chilean earthquake (Figure 16c, Table III) show a predominance of horizontal transverse motion. It should be noted that the station CHA was located on the flank of the Leduc-Woodbend oilfield, a region in which there exists significant departure from horizontal layering in the sedimentary crust (see Figure 14). Indeed, it appears that the oil bearing Devonian reef structure causes the overlying sedimentation layers to be lifted. The complicated subsurface geometry at the station CHA does not permit easy prediction of the departures from the expected zero transverse motions. Also, strongly topographic features of the nearby North Saskatchewan river valley (typically 1 kilometer across and 100 meters deep) could affect the CHA records. Furthermore, although the CHA record of the Chilean event is notably anomalous with respect to transverse motions, the Novaya Zemlya records are not. This may indicate that there is an azimuthal dependence of anomalous transverse motions. The essentially anomalous nature of the CHA location was known before analyses and the two events were included only for the purpose of comparing the distinctly horizontal layering at LED and LAR with the more structured geometry of CHA.

3.7 Frequency Analyses - Theoretical Spectral Amplitudes

For the determination of theoretical frequency amplitude response characteristics of the model crusts, impulse (white, zero phase spectrum) signals representing P waveforms were used as inputs to the linear system analogs. Amplitude and phase spectra were calculated for the surface motions, for all internal boundary motions and for the waveforms retransmitted into the basement halfspace. For non-normal incidence conditions, both the vertical and horizontal motion amplitude components have been obtained. A frequency sampling interval of 0.1 Hz between 0 and 5 Hz was chosen to reveal the major spectral peaks in this range while limiting the computational time.

The surface motion amplitude response for the sedimentary portion of the Leduc model crust (Table III) above the Precambrian for normal incidence is shown in Figure 17. The phase spectra showed mainly a lagging trend with frequency due to the time delay between the input waveform and the surface motions. The phase spectra and internal boundary motion spectra will not be presented in this analysis.

It is notable that reverberation resonances occur at several frequencies (Figure 17). The first resonance peak of the LED crustal response at approximately 0.4 Hz is primarily due to the reverberation multiple with the longest path bounded by the surface and the Precambrian basement. (Appendix I describes a procedure for the computation of the fundamental reverberation frequency and harmonics for one layer).

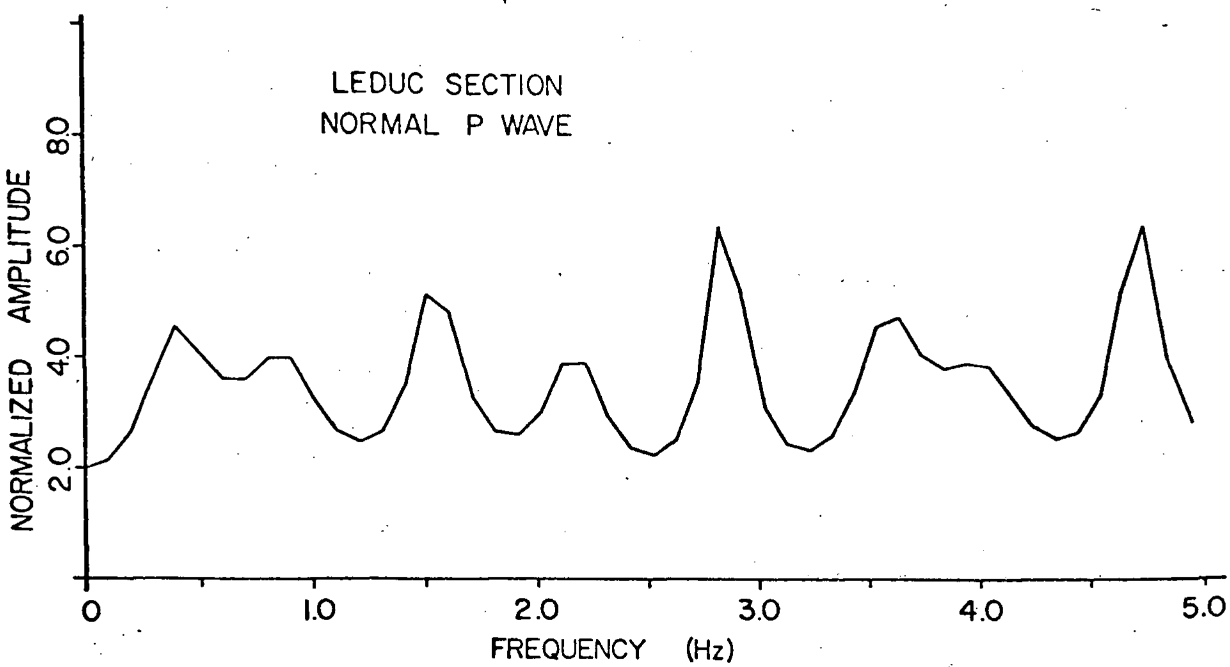

Fig. 17. The spectral amplitude response of the theoretical non-attenuating Leduc crustal section to a normal incidence white amplitude spectrum P-wave incident at the Precambrian-Cambrian boundary.

Spectral peaks for higher frequencies are the result of the combined effects of higher harmonics of this reverberation and primary resonances for multiples with shorter paths (which cause higher frequency reverberation) along with their coincident harmonics.

The spectral amplitude response for a 30° (at the Precambrian boundary) incident P wave consists of both vertical and horizontal components (Figure 18). There is a marked similarity in the form of the vertical amplitude component with that for the normal incidence condition although its amplitudes are reduced. Particularly

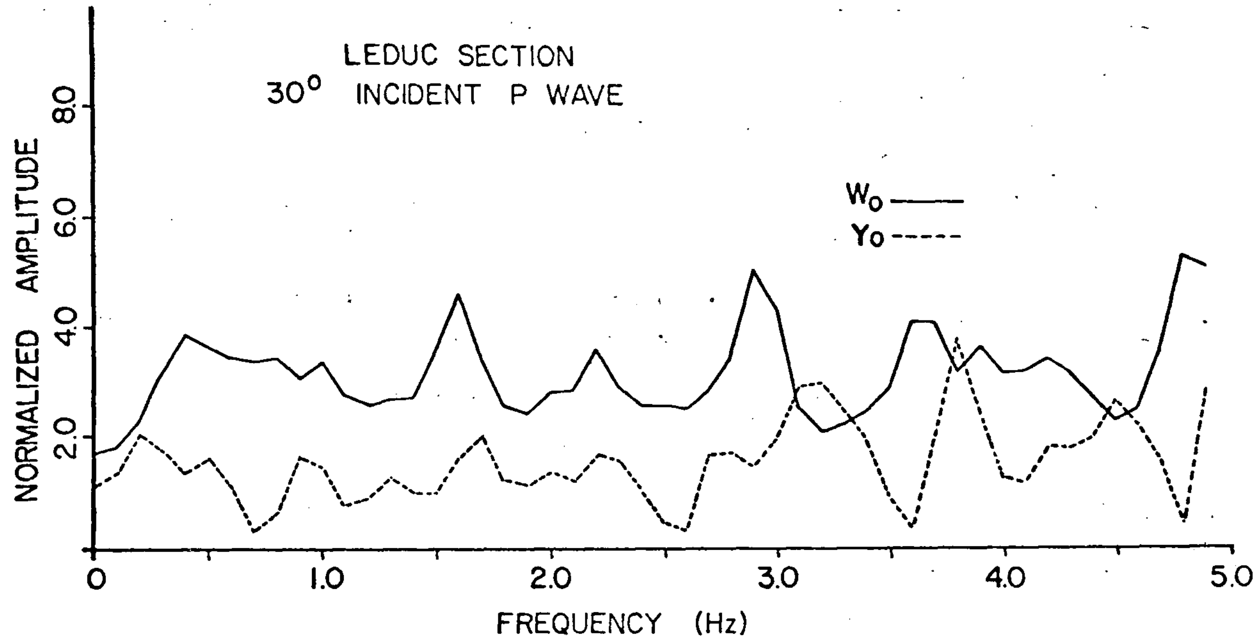

Fig. 18. The spectral amplitude response of the theoretical non-attenuating Leduc crustal section to a 30° incident P wave at the Precambrian-Cambrian boundary. W_o represents the vertical component motion, Y_o the horizontal.

the resonance of the fundamental reverberation and the peaks near 1.6 Hz, 2.3 Hz and 2.9 Hz are common to both responses. This is expected because for small incidence angles, the P motions within the layering dominate the vertical component while the SV motions dominate the horizontal component. In this example, the horizontal amplitudes are lower than the vertical; however, for S wave inputs or P wave input motions with much larger incident angles the opposite condition would occur. A 30° incident angle at the Precambrian boundary corresponds to a 42° angle at the Mohorovicic discontinuity. This incidence angle corresponds to a source at only 25° epicentral distance (after Ichikawa, see Basham, 1967). For such nearby sources, signals from refractive and reflective paths contaminate the early P coda. Also, geometrical spreading of the wavefront invalidates the necessary plane wave assumption. Experimentally, source distances greater than approximately 35° should be used.

The effect of crustal absorption on the spectral amplitudes for the 30° incidence condition is shown in Figure 19. For the calculation of these example spectra Q=50 was chosen to represent every layer for both P and S motions. This Q is near the computed average for the sediments (Table II). Acausal, zero phase attenuation with no attending dispersion is considered. Significantly, there is a decrease

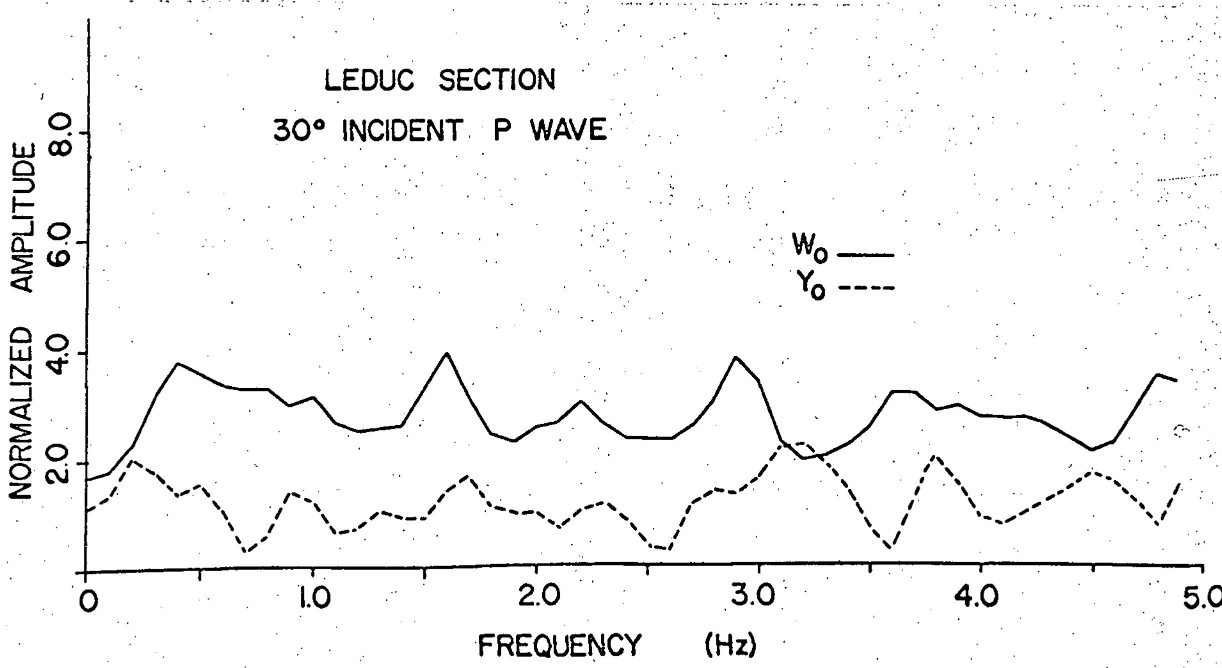

Fig. 19. The spectral amplitude response of the theoretical crustal section to a 30° incidence P wave at the Precambrian-Cambrian boundary. The crust is assumed to have a Q of 50 in every layer.

of the spectral amplitudes with increasing frequency for both vertical and horizontal components. The constant Q model gives a negative exponential dependence of amplitudes with frequency which describes this condition. A further significant effect of the absorption is the apparent reduction in the quality of the resonances, particularly at higher frequencies. The resonance quality is determined by the energy absorbed per cycle at the resonant frequency harmonic and is a direct measure of the crustal attenuation. It was noted previously that physical attenuation must be causal which demands a dispersion effect such as in the Futterman model. The dispersion of phase velocities would cause a slight shift of the resonance peaks but the form of the curve amplitude dependence on frequency would remain nearly unchanged. Since the effects of dispersion on the spectral amplitudes are minimal, the acausal model reasonably represents the crustal amplitude response of an attenuating crust.

3.8 Frequency Analysis - Spectral Ratio Technique

To compare the spectral amplitude responses with ground displacement amplitudes due to earthquakes, it is necessary to remove the effects of the seismograph response. This requires extreme enhancement of low frequency components where microseismic and instrument noise may exceed signal levels and high frequencies where wind, water and cultural noise may swamp motions generated by the teleseismic waves. Also, these seismograms are basically a record of the ground motion velocities rather than displacements and an integration of the records with respect to time would be necessary before spectral amplitude comparisons could be made. Rather than apply such reconstructions to the data, the technique using spectral ratios (Phinney, 1964) is more useful. Since the frequency response character of the seismographs were normalized, all motion components can be assumed to have been identically affected by the instruments.

For a given P arrival, the vertical and radial horizontal seismogram P coda are responses to the same input waveform which is incident at the base of the crust. Their Fourier spectra may be described:

$$\begin{aligned} W_o(\omega) &= H_v(\omega)\cdot U_{INPUT}(\omega) \\ Y_o(\omega) &= H_h(\omega)\cdot U_{INPUT}(\omega) \quad . \end{aligned} \tag{3-3}$$

where $H_v(\omega)$ and $H_h(\omega)$ are the total crust vertical and radial horizontal transfer functions and $U_{INPUT}(\omega)$ is the Fourier spectrum of the arbitrary input waveform. It is evident that the vertical-to-horizontal spectral amplitude ratio depends only upon the crustal transfer function ratio and is completely independent of the input waveform (Phinney, 1964):

$$V/H \doteq \frac{|W_o(\omega)|}{|Y_o(\omega)|} = \frac{|H_v(\omega)|}{|H_h(\omega)|} \tag{3-4}$$

Furthermore, over small horizontal distances, one may expect that the low frequency content of a P arrival incident on the base of the crust due to a teleseismic source would not vary significantly. Therefore, the ratios between the vertical component spectral amplitudes at two nearby sites should describe another ratio which is independent of the input waveform. For example:

$$W_o(\omega)]_1 = H_v(\omega)]_1 \cdot U_{INPUT}(\omega)$$
$$W_o(\omega)]_2 = H_v(\omega)]_2 \cdot U_{INPUT}(\omega) \tag{3-5}$$

and:

$$V_2/V_1 = \frac{|W_o(\omega)]_1|}{|W_o(\omega)]_2|} = \frac{|H_v(\omega)]_1|}{|H_v(\omega)]_2|} \quad . \tag{3-6}$$

These vertical-to-vertical component spectral amplitude ratios may be useful in the comparisons of the crustal sections at two stations. Also, because the vertical components usually possess high signal-to-noise ratios relative to the horizontal components, the accuracy obtainable from such analyses should be better.

Phinney showed that a comparison of the V/H ratios determined experimentally from long period P-wave seismograms and by direct calculation using the Haskell method could be useful for crustal interpretations. Although, his work yielded good comparisons between theory and experiment, other investigations have been less successful at short periods (Utsu, 1966; Ellis and Basham, 1968). The work of Ellis and Basham included an area in central Alberta near that studied in these analyses. They ascribed part of their limited success to scattering which generates noise from signal. However, their Haskell matrix analyses did not include attenuation. The present work will attempt to determine the significance of crustal absorption to spectral ratios. Later, it will be shown that for short periods and the low Q's of crustal sediments, the effect of absorption can be considerable.

Fig. 20a. Spectral V/H ratios for various attenuation conditions in the sedimentary crust compared to the non-attenuating ratios. The designated Q's have been applied to every layer; the solid line is for infinite Q.

Fig. 20b. Spectral V/H ratios for Q values in each layer assigned according to Table II compared to non-attenuating ratios. The solid line is for infinite Q; the dashed line for the chosen Q's.

SPECTRAL V/H RATIOS

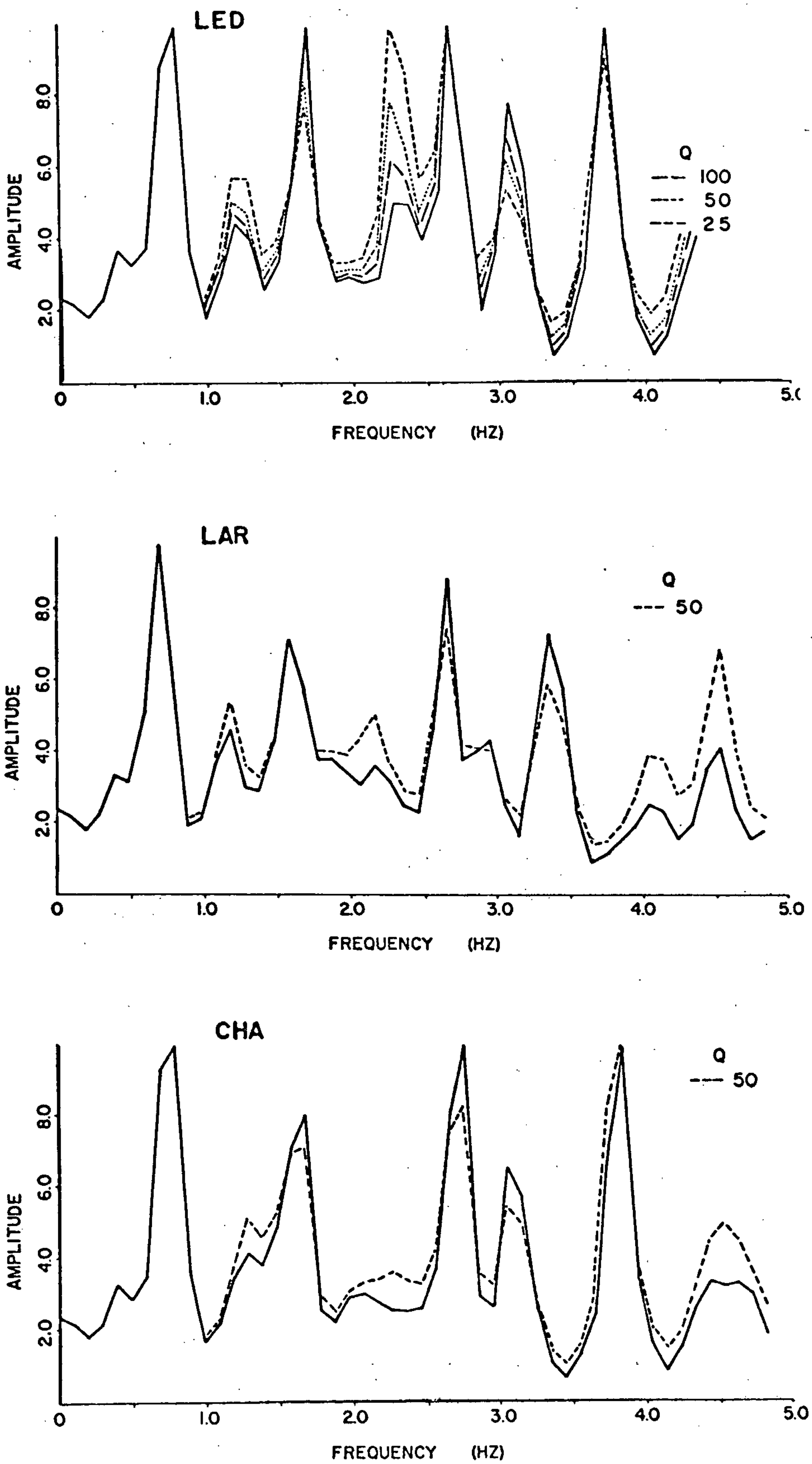

Fig. 20a.

SPECTRAL V/H RATIOS

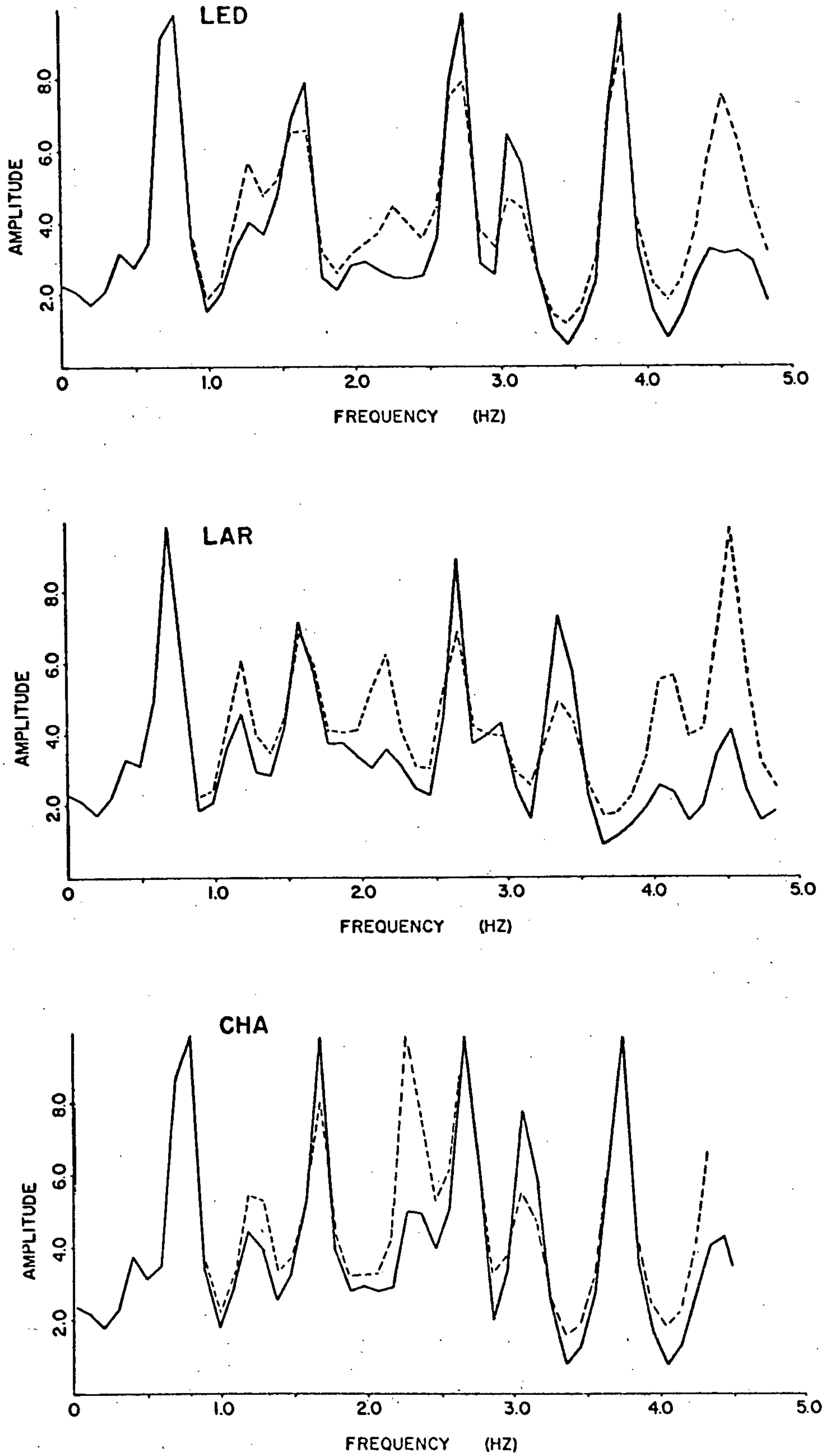

Fig. 20b.

The work of Ellis and Basham in central Alberta included the analysis of 41 events which allowed them to use a statistical approach in their experimental comparisons. In this present work only 6 events are used and statistically valid inferences cannot be deduced.

3.9 Theoretical Spectral Ratios

Theoretical V/H ratios were computed for the three station crust models for an incident P wave making a 22^{o} angle with the Precambrian upper boundary (which is equivalent to a 30^{o} incidence angle at the Mohorovicic boundary). The computed ratios are presented in Figures 20a and 20b. Several different internal layer attenuation conditions are compared. Since the broad features of the V/H ratios are not greatly affected by neglecting the large scale layering of the sub-sedimentary Alberta crust (Ellis and Basham, 1968), only the portion of the crust above the Precambrian has been considered in these analyses. The major effect of neglecting the three deeper model layers is to remove closely spaced harmonic peaks due to the long path multiples involving the deep crustal boundaries. Smoothing of the computed ratios was not considered necessary but the frequency sampling increment was chosen sufficiently small to determine all of the major spectral ratio features. Small changes in the P wave incidence angle have little effect on the location of the V/H peaks although the peak amplitudes are modified. Consequently, if the absolute ratio amplitudes are not required, the one set of ratios for 22^{o} incidence should be sufficient for comparisons with the ratios experimentally determined from the suite of earthquake events with incidence angles ranging from 14^{o} to 23^{o}. The theoretical ratios for 22^{o} incidence should underestimate the ratio amplitudes for the smaller angles of P-wave incidence.

The curves designated by infinite Q (Figures 20a and 20b) describe non-attenuating crustal conditions; designations with other Q's represent the V/H ratios for the crust model with the specified Q applied to each layer. The value Q=100 is thought to be a conservative estimate of the absorption in the Alberta sediments but the value Q=25 must be implausibly low. The Q values of Table II average 45 for the sediments.

In these ratio comparisons, it is apparent that at low frequencies the effect of crustal absorption is virtually insignificant. But, above 1 Hz absorption effects increase noticeably. For example, the LED and LAR V/H ratio peaks near 1.2 Hz are increased sharply by lowering Q while the ratio peaks near 1.7 Hz are decreased. Furthermore, the LED V/H peak near 2.4 Hz is more than doubled by decreasing the theoretical Q from infinity to 25. For all three crustal models, large increases in the ratio amplitudes are particularly evident beyond 4 Hz for attenuating conditions. Attenuation of a harmonic wave increases exponentially with frequency and the effect of absorption must become a dominant factor in V/H ratios at high frequencies.

The positions of several of the major V/H peaks are not affected by the addition of attenuation. Therefore, these features should be useable for comparisons of the basic crustal models with experiment. Similarly, the features which strongly depend on attenuation could provide separate information on the crustal absorption characteristics.

Theoretical ratios of the vertical component spectral amplitudes from station pairs are shown in Figure 21. Vertical-to-vertical ratios have been computed only for non-attenuating crust conditions because the absorption characteristics at the three close locations should be very

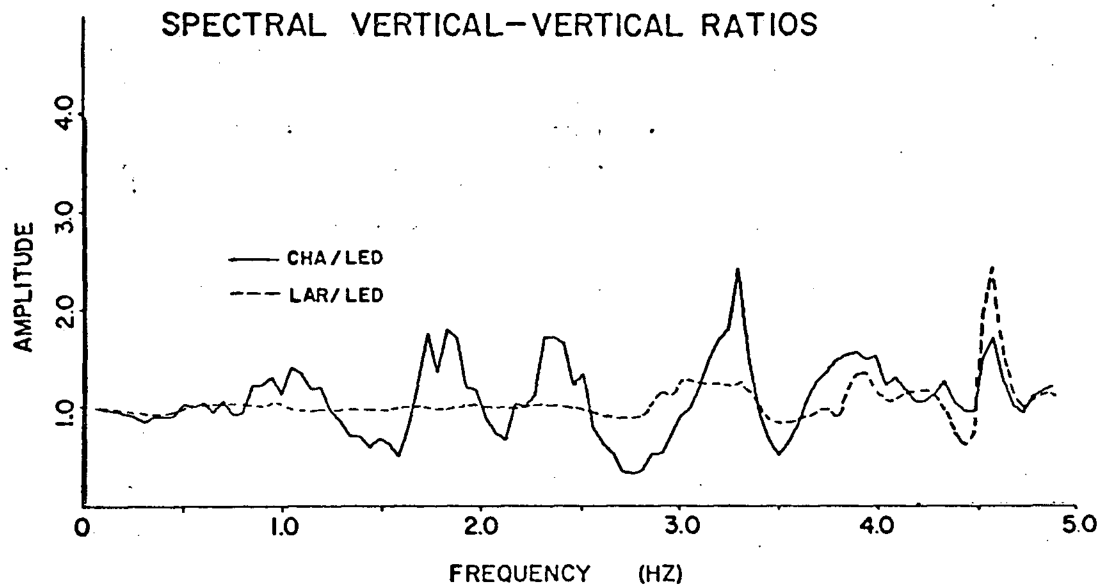

Fig. 21. Vertical-to-vertical spectral ratios for non-attenuating crust models.

similar and the effect on the ratios must be small. Significantly, the theoretical LAR/LED vertical ratios are featureless below 3 Hz while the CHA/LED ratios possess more character. This is not surprising since the ratio describes the relative vertical crustal responses and since the LED and LAR crust models are quite similar their response characteristics should be similar. The CHA crust model describes an anomalous location on the Leduc-Woodbend oilfield. The difference in the CHA and LED models is manifested by the greater vertical-to-vertical spectral ratio character.

3.10 Experimental Spectral Ratios

For comparisons of experimental and theoretical spectral ratios, discrete Fourier spectra have been computed using the algorithm of Cooley and Tukey (1965) on the first 25 seconds (500 sample points) of the normalized records following the P onset. Vertical-to-horizontal experimental spectral ratios computed from these spectra are shown for the chosen events in Figures 22a-f. Within the 25 second time window the transient P-coda has generally decayed to ground noise levels (e.g. Figure 16a-f) so that it may be assumed that the spectrum calculated from the truncated records generally represents the infinite duration transient. The choice of a longer record would decrease the average signal-to-noise ratio and reduce confidence in the ratio calculations. Also later arriving phases could be admitted. The 25 second record length is a reasonable compromise for the chosen event records. The sampling interval of 0.05 seconds from the digitization and the record length of 25 seconds gives a frequency resolution of 0.04 Hz using the Cooley-Tukey algorithm. This resolution is excessive for comparisons with the theoretical ratio computations. Smoothing of the experimental spectra using 5 and 9 point Fejer (triangular) running operators was applied to reduce the highly resolved detail while retaining the broad spectral features which should result from reverberations in the upper sedimentary crustal layers.

For three chosen event seismogram sets, smoothed ratios of the Fourier spectra of the signal and 25 seconds of pre-event noise for both vertical and horizontal components were compared (Figure 23a-c) to determine confidence limits on the computed V/H ratios. For these three

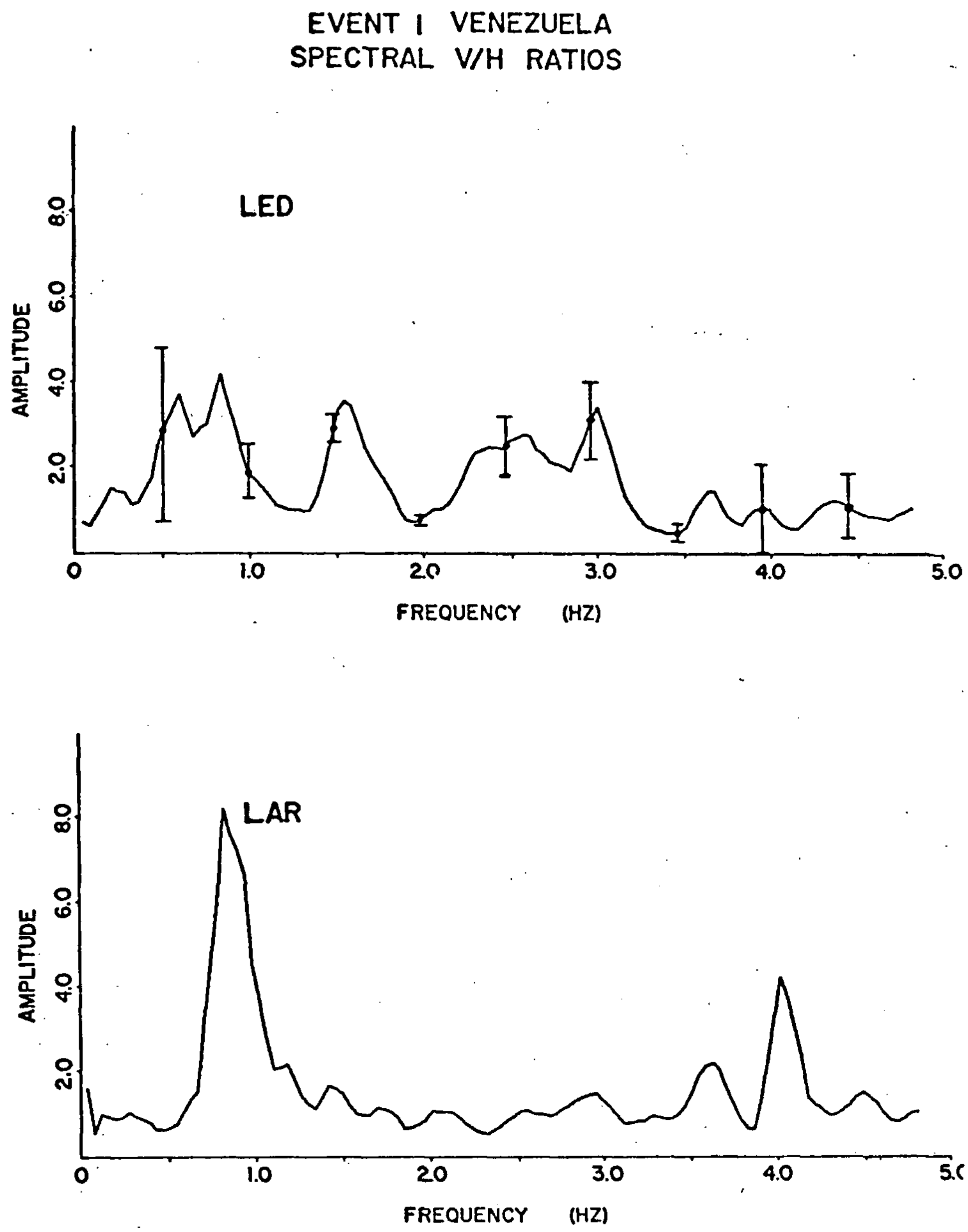

Fig. 22a-f. Experimental V/H spectral ratios obtained from the suite of seismograms. Error bars are included on 3 of the spectral ratios for comparison. These error conditions are thought to be typical.

(a) Venezuela

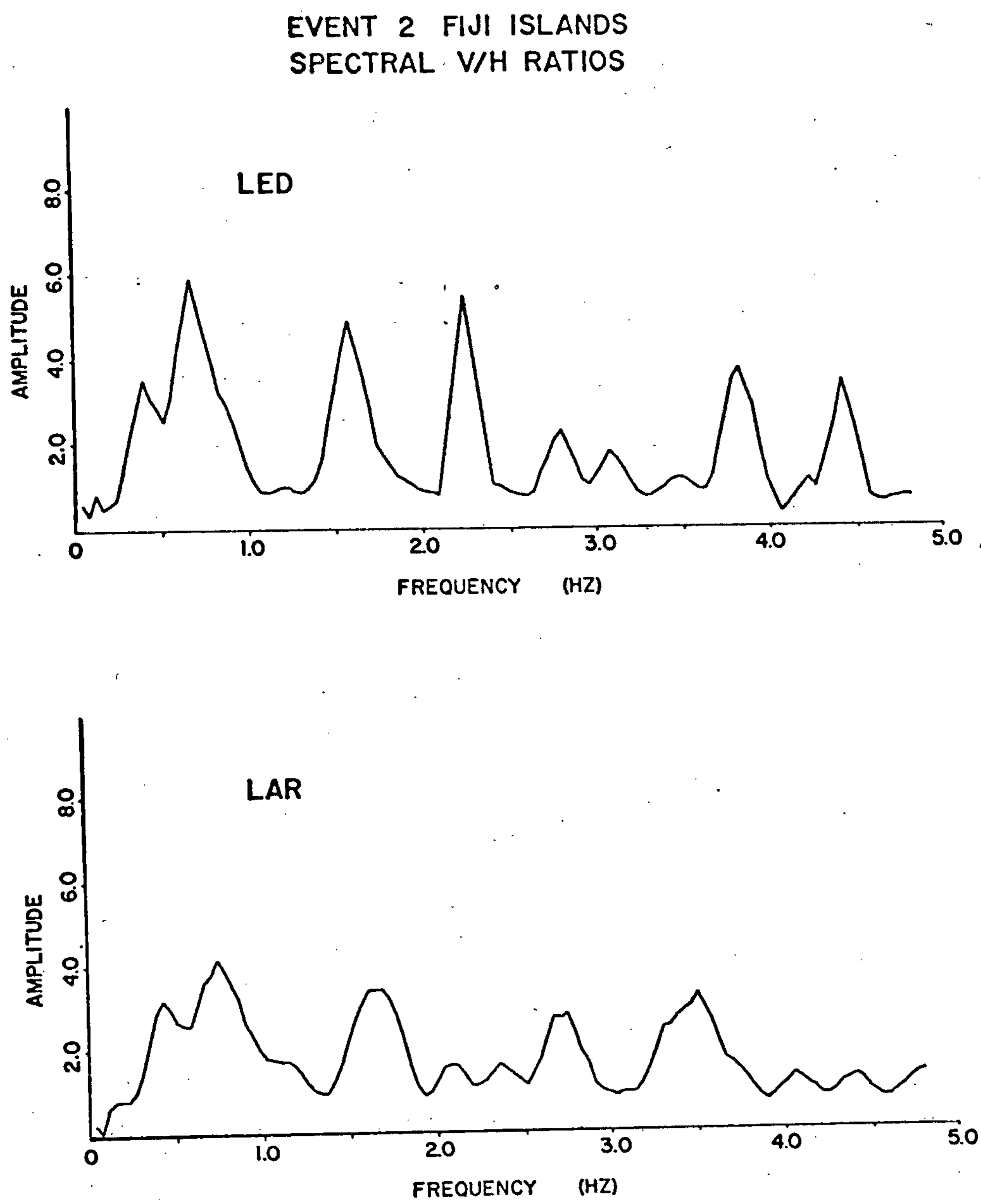

(b) Fiji Islands

EVENT 3 CHILE
SPECTRAL V/H RATIOS

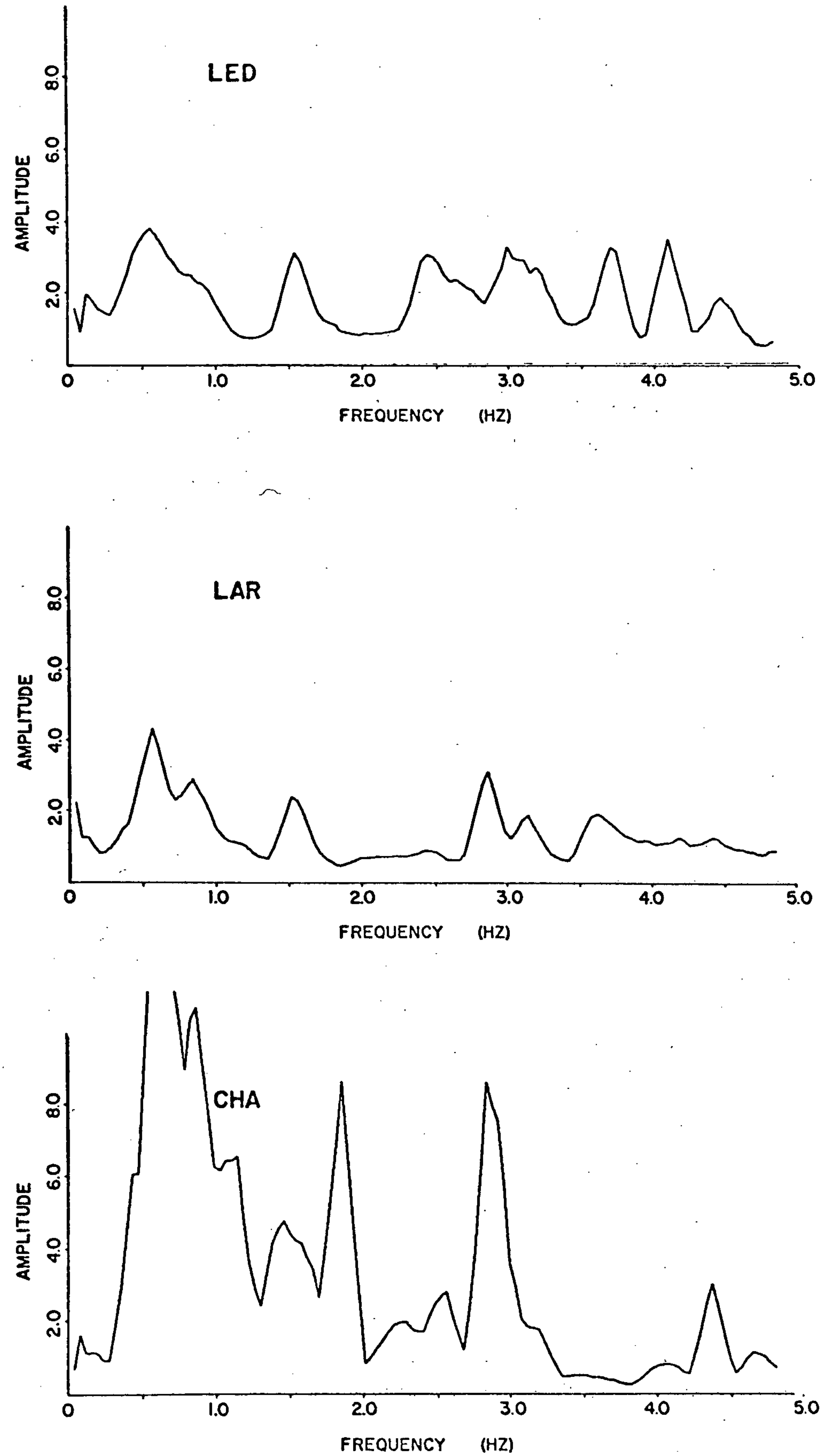

(c). Chile

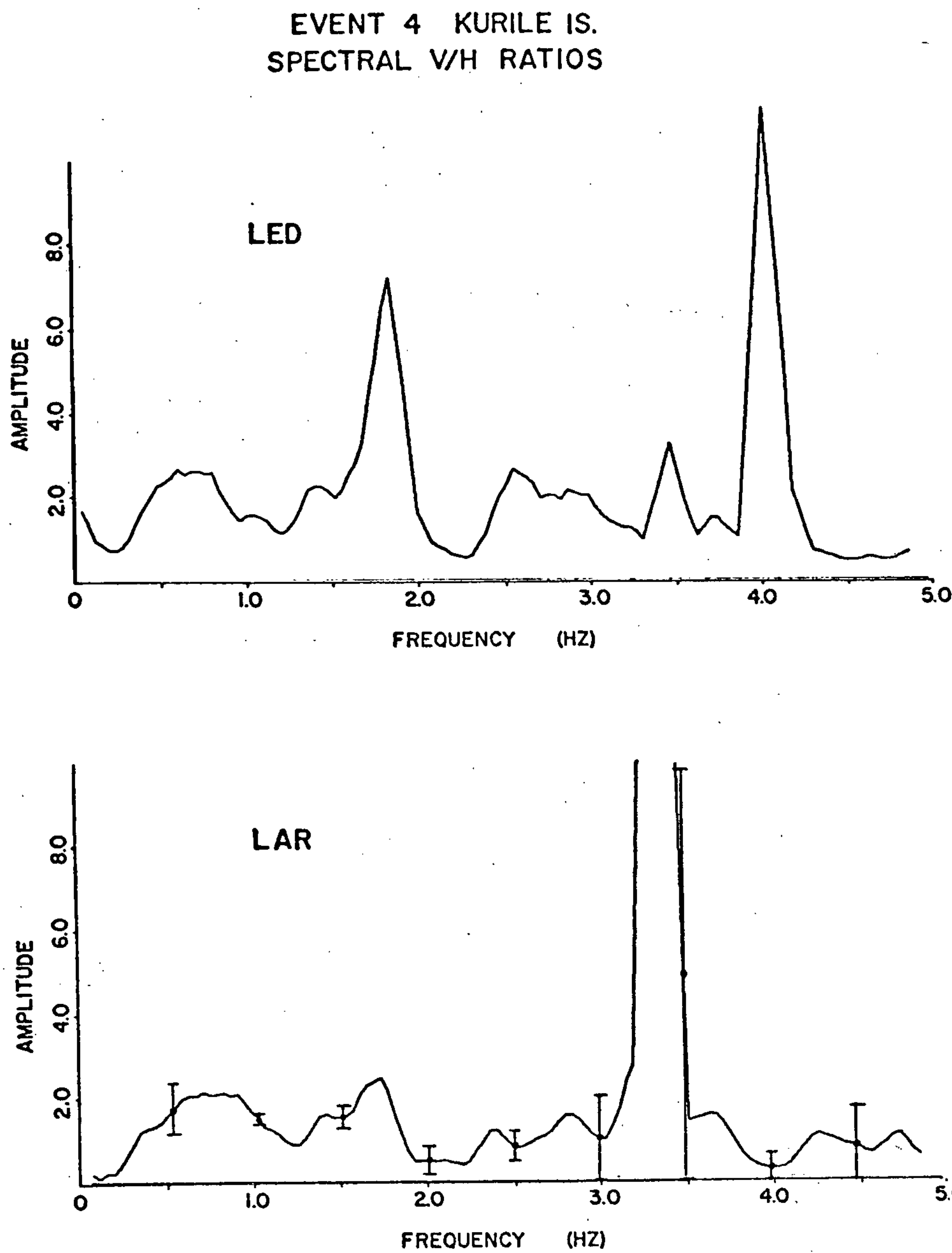

(d) Kurile Islands

EVENT 5 NOVAYA ZEMLYA
SPECTRAL V/H RATIOS

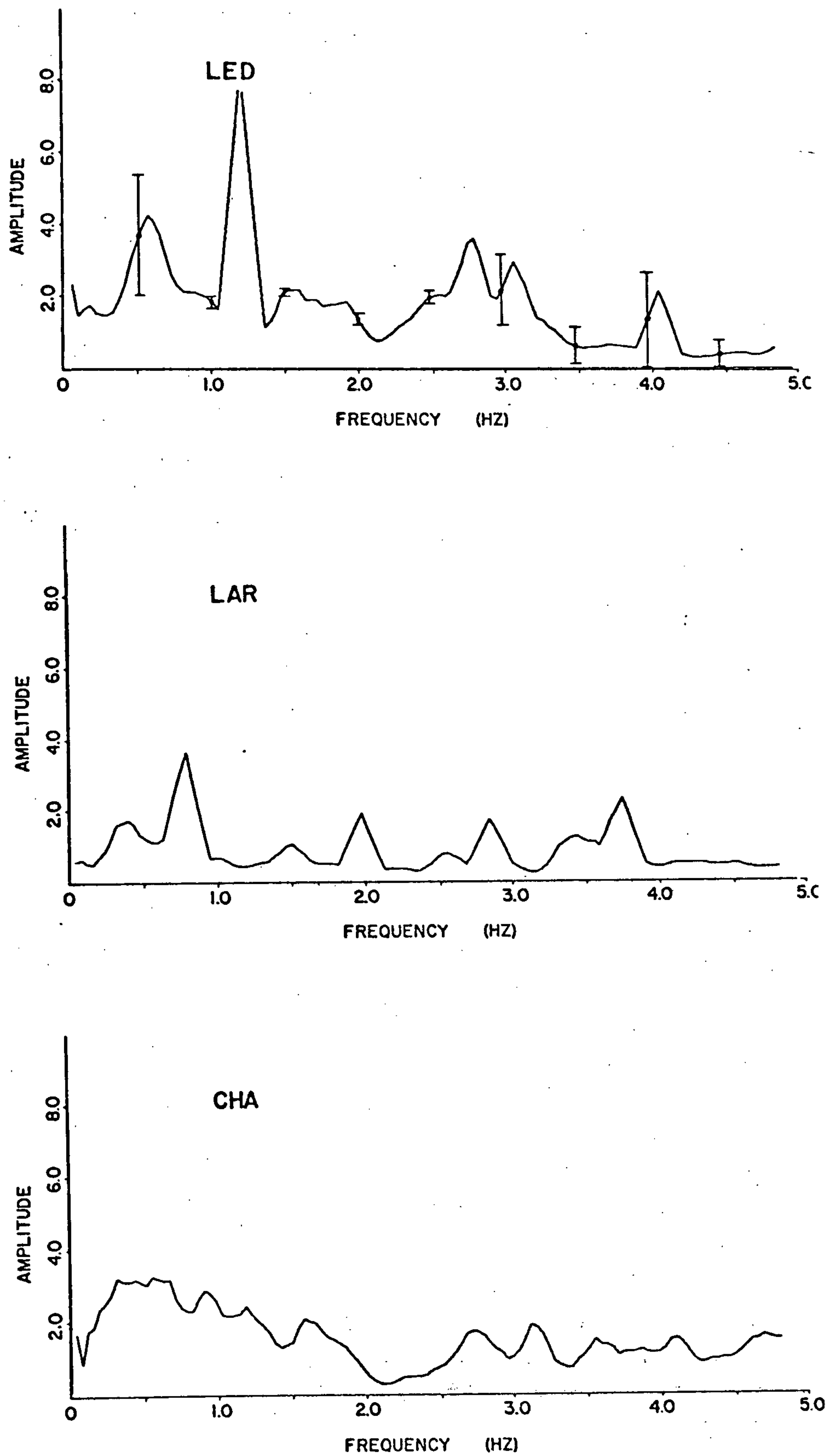

(e) Novaya Zemlya

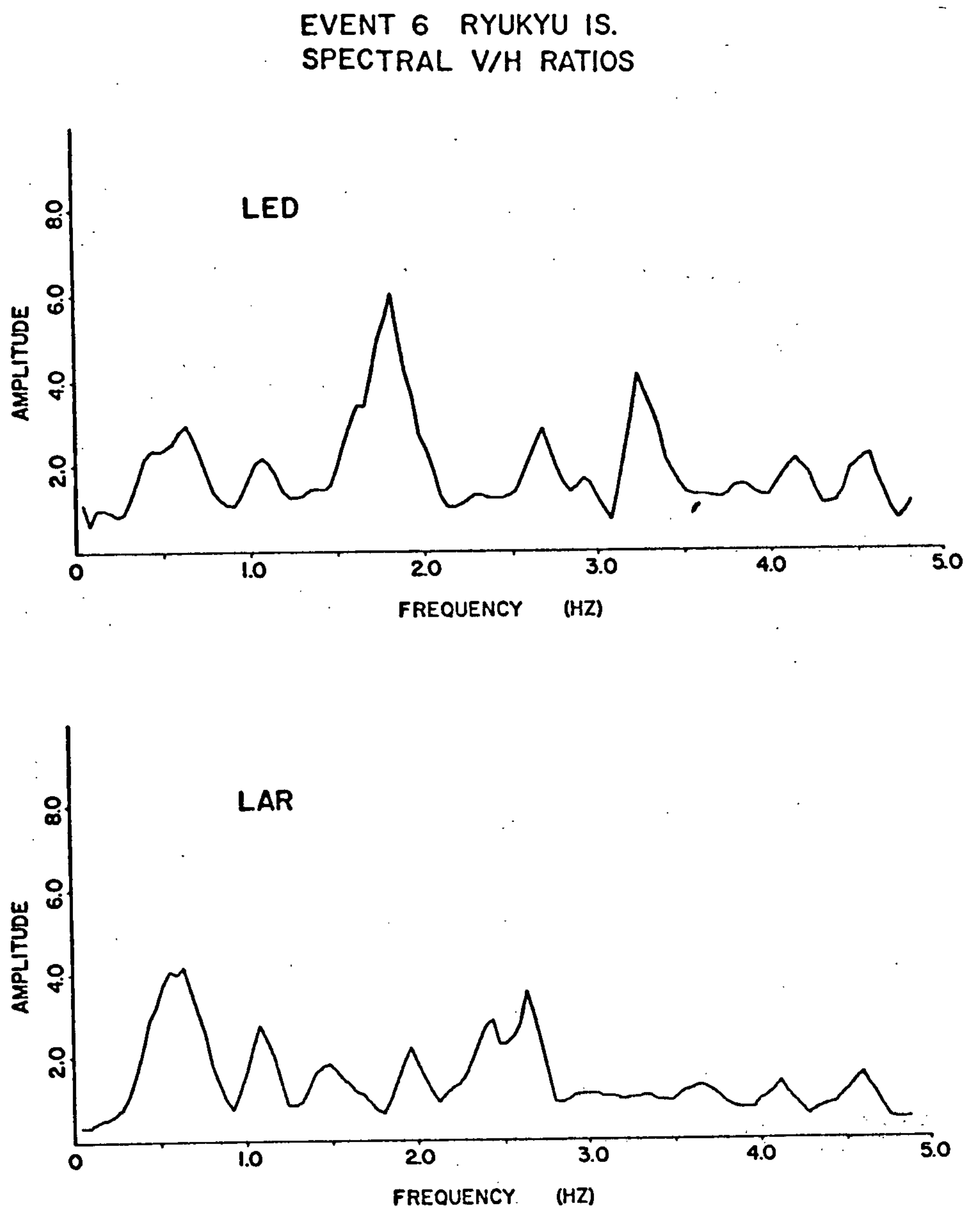

(f) Ryukyu Islands

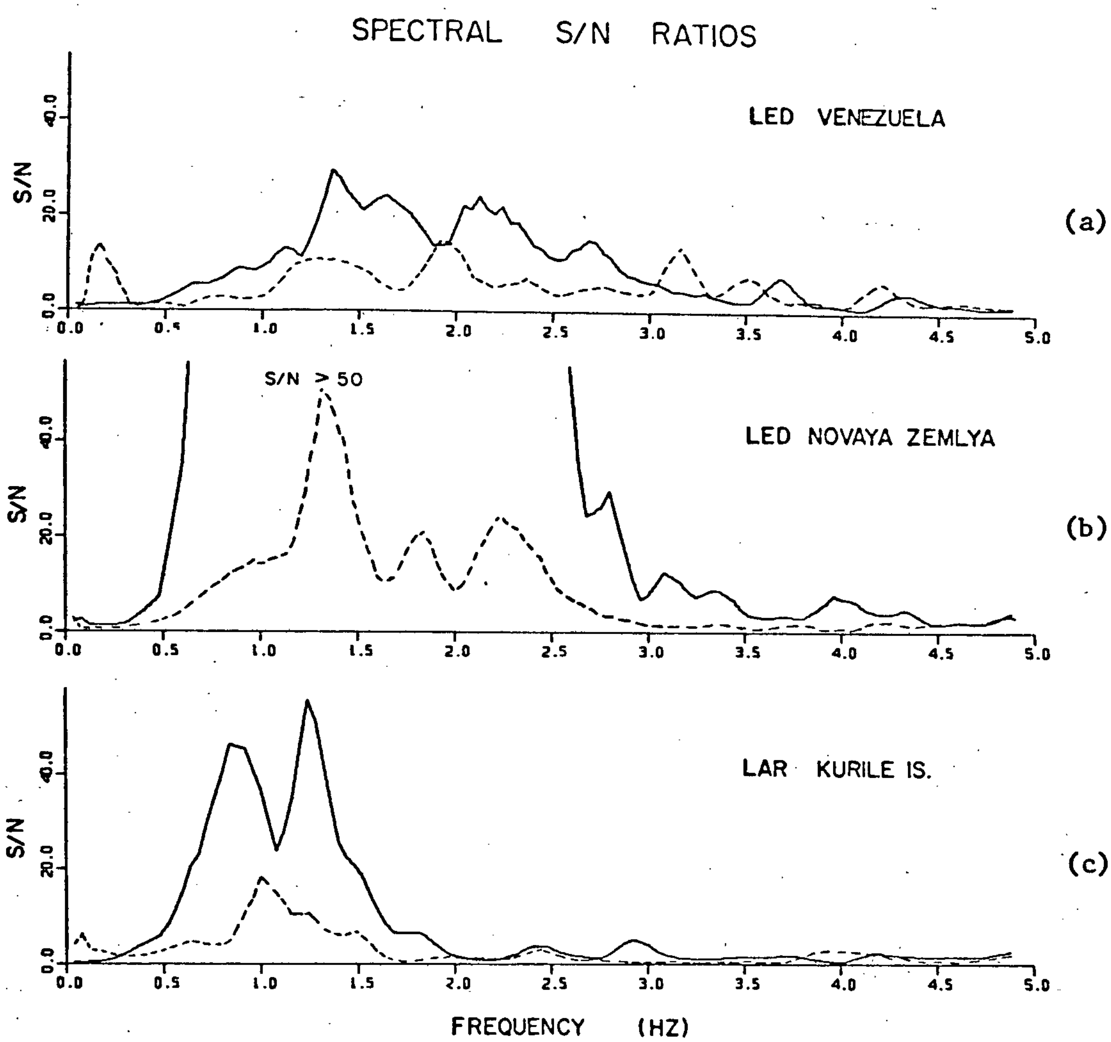

Fig. 23a-c. Spectral signal-to-noise ratios for the vertical (solid line) and horizontal (dotted line) for three events. The noise spectrum was obtained from the 25 seconds preceding the P onset of each event.

analyses, large signal-to-noise ratios were found between 1 and 3 Hz. The expected root mean squared errors due to the background noise are designated by the error bars on the corresponding spectral ratios (Figures 22a,d,e). The LED Venezuela recording showed typical relative pre-event noise; only the Fiji Islands records at LED and LAR possessed lower apparent signal-to-noise ratios. Thus the relative errors found for the LED Venezuela ratio is considered to be typical of (or worse than) the remaining ratios for which error conditions were not obtained. (One further possible exception is the LAR Venezuela recording for which there is a particularly high frequency noise contamination. However, the signal-to-noise ratio at useable frequencies does not appear to be poor).

3.11 General Features of Spectral Ratios

The most notable general feature of the experimental V/H ratios is that the amplitudes are much lower than the theory predicts. (the theoretical computations for the large 22^{o} incidence angle should underestimate ratio amplitudes for the steeper angles). The only possible exception is the CHA Chile seismograms (Figure 16c, Table III) for which high ratios are evident between 0 and 2 Hz but return to the anomalous lower values beyond this. This event recording is also anomalous with respect to horizontal motions since the transverse amplitudes exceeded radial amplitudes.

Reduced ratio amplitudes must result from a relative enhancement of the horizontal ground motions compared to the vertical motions. Possible causes include background noise and signal generated noise by scattering. It is significant that the horizontal component background noise was generally higher than the vertical. This effect would be expected to reduce the ratio amplitudes towards values less than 1 at frequencies where the signal-to-noise ratio is small. However, records for which the average signal-to-noise ratio appears to be very high would then be expected to show substantially better agreement with the theory. But even those with the least relative background noise also exhibit reduced ratio amplitudes. For example, the LED seismograms from the Chile and Novaya Zemlya events show anomalously low ratio amplitudes. The computed ratios for which error conditions were calculated (Figures 22a,d,e) determine that these reduced amplitudes are not due to background noise, at least in the band from 1 to 3 Hz.

In their work on V/H ratio comparisons, Ellis and Basham (1968) suggested that scattering noise generated from the signal could have caused part of their lack of comparison between their theoretical and experimental results. Scattering can result from both internal crustal irregularities and from surface topography which determines a non-flat free surface boundary. To explain a reduction of ratio amplitudes by scattering, it is necessary that the mechanism preferentially reduces vertical component motions or preferentially converts vertical motions to horizontal. Since a vertical to horizontal conversion is basically a P to S conversion, a scattering mechanism which increased shear motions relative to compressional motions could explain the reduced apparent experimental ratios. The effects of topographic scattering should most affect the LED station which was located near a broad valley and the CHA station which was situated within 2 km of the North Saskatchewan River valley which is approximately a half km wide and 100 m deep. Surprisingly, only the CHA station gave spectral ratios which were not anomalously low.

An attenuation condition which preferentially absorbed P motions relative to S motions could also help to explain this condition. However, most experimental evidence (e.g. McDonal et al, 1958) shows that S attenuation is greater than P which would determine the inverse effect.

3.12 Details of the Spectral Ratios

The V/H ratios from the recordings of the six events have a common significant spectral ratio maximum between 0.5 and 1 Hz. (The ratios computed for the CHA recordings show less character for this peak and its validity is questionable in this case). The theoretical calculations find a major ratio maximum near 0.7 Hz which correlates with the experimental feature. Most ratios computed for the LAR and LED station events show a further common maximum between 1.5 and 2 Hz. However, for the LED Novaya Zemlya ratios, this peak is displaced to approximately 1.3 Hz which is suspicious although the record quality and signal-to-noise ratio are especially good. Theoretical ratios for LED and LAR show maxima at 1.6 and 1.7 Hz which apparently correlate with these experimental features. Low frequencies are primarily affected by the structures of the crust which have a scale size of the order of the harmonic wavelength. Since the gross crustal features should be well modelled, it is not surprising that this area of agreement between theory and experiment exists. However, beyond approximately 2 Hz the little correlation between the theory and experiment could indicate that the small scale model structure inadequately describes the actual crusts. Also, since P-arrival signal levels decrease rapidly with frequency, background noise begins to play an increasing role at higher frequencies. Beyond 3 Hz, the signal-to-noise ratios become so low (Figure 23) that good correlations cannot be expected. Where the signal-to-noise ratio is near (or below) 1, background noise must largely determine the V/H ratios. But, even beyond 3 Hz the smoothed ratios computed solely from the pre-event noise for the three events were found not to be similar to the equivalent event ratios. Consequently, if the background noise can be assumed to be a stationary process, it does not appear to be the whole cause of the high frequency discrepancies between theory and experiment. This lends weight to a scattering noise hypothesis. The cause of the large LAR V/H ratio peak near 3.5 Hz is not evident. However, signal-to-noise ratios are very small (as evidenced by the large error bars (Figure 22d)) beyond 3 Hz and the peak is probably not an indication of crustal features.

Any similarity in the experimental and theoretical ratios for the CHA Chile event recordings is surprising because this station was the most anomalous in terms of subsurface layering and topography. Furthermore, the Chile event records showed particularly large transverse horizontal motions. Apparent correlations should be discounted as accidental.

The inclusion of attenuation in the theoretical solutions did not improve the agreement between theory and experiment. Furthermore, the experimental details do not discriminate the various crustal Q models. For example, although the 1.7 Hz peak was noted as a possible indicator of crustal attenuation conditions it is apparent that there is no consistency in its relative amplitude among the experimental ratio results.

For ideal horizontal layering, the V/H ratio is independent of the azimuth of the P-wave ray approach. However, two pairs of experimental ratios show strong azimuthal dependence. The LED ratios from the Venezuela (azimuth 117° E of N) and Chile (azimuth 138° E of N) events give nearly identical ratio character, within the expected error limits, throughout the strong signal band below 3 Hz. A striking similarity is not so noticeable on the corresponding LAR recordings. Also, the LED Ryukyu Is. (308° E of N) and Kurile Is. (305° E of N) ratios are quite similar to about 3 Hz; again, the LAR ratios do not exhibit much similarity. For the LED recordings, such azimuthal correlations are more notable than correlations between events at similar receiver-to-event epicentral distances. Admittedly this sample of events is small, but the results seem to indicate that the ideal horizontal layering condition does not explicitly apply to the crust beneath LED.

Experimentally determined spectral ratios between station vertical component pairs are shown in Figure 24a-c. The LAR/LED ratios from the Venezuela, Chile, Novaya Zemlya and Kurile Is. events generally show the expected relatively featureless ratios below 2.5 Hz. But, beyond 3 Hz the ratios become much larger than the theory predicts. The Fiji and Ryukyu ratios also appear to be anomalous at the low frequencies. Both have more character and larger amplitudes than expected. Little character from the theoretical ratios correlates with the experimental ratios; however, the Kurile Is., Venezuela and Novaya Zemlya experimental ratios all show similar character below 3 Hz. Since the signal-to-noise ratios are generally high at these frequencies, some of this similarity must be significant although its interpretation

SPECTRAL VERTICAL-VERTICAL RATIOS

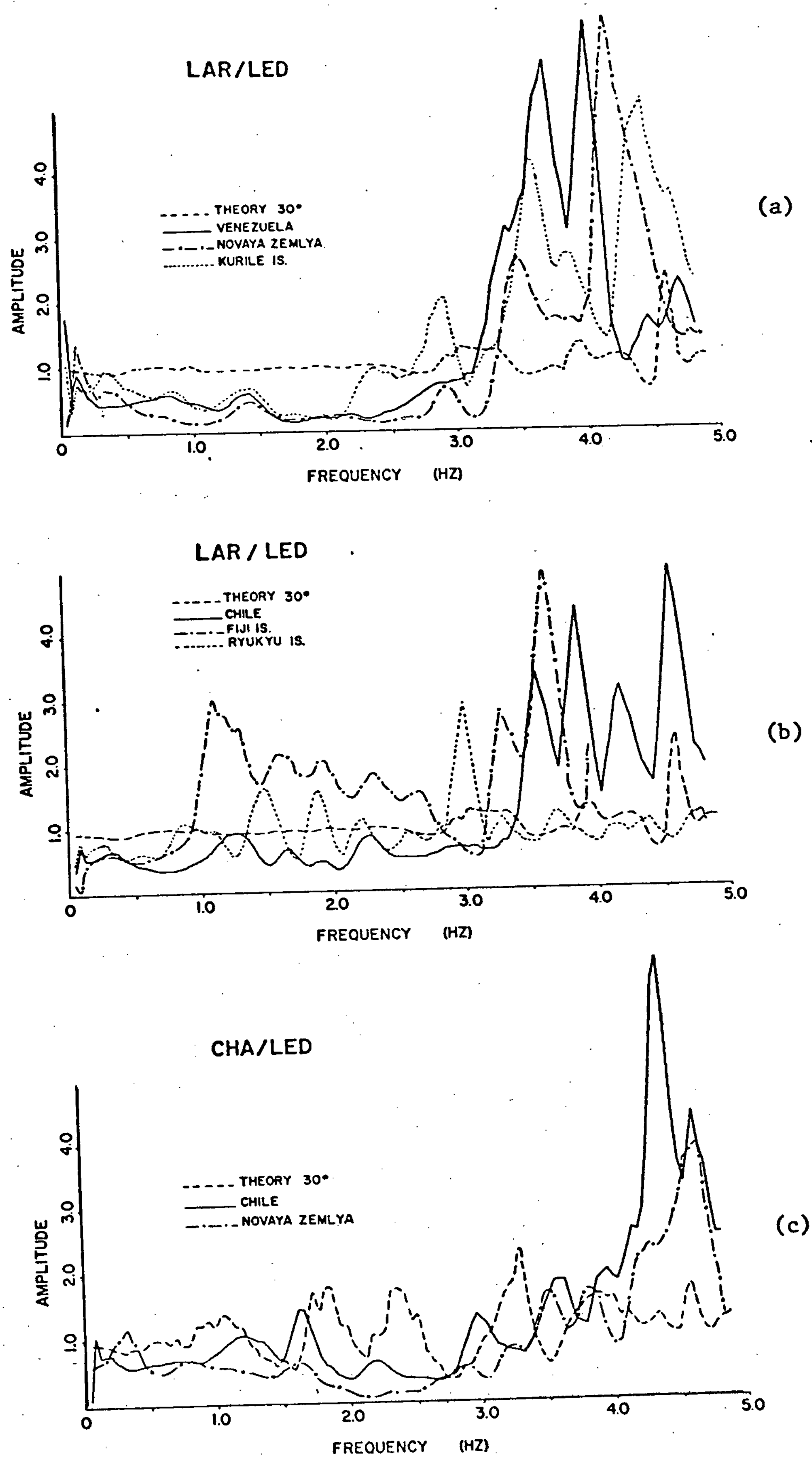

Fig. 24a-c. Theoretical vertical-to-vertical ratios are compared to those obtained from the experimental seismograms for 30° incidence angle.

is not evident. The CHA/LED ratios from the Chile and Novaya Zemlya events show little correlation with theory. However, beyond about 3 Hz a ratio enhancement relative to theory is also observed as for the LAR/LED ratios. The enhancement suggests that the LED vertical component lack high frequencies relative to the other two stations. The LED instruments were located on the Canadian seismic network pier on bedrock while the LAR and CHA instruments were less ideally located on alluvium. High frequency noise is easily generated by wind in unconsolidated materials and probably contributes to the greater noise at stations LAR and CHA.

3.13 Time Domain Syntheses

In principle, it is possible to determine exactly one among the crustal transmission response, the incident waveform from the basement and the output seismogram set provided the other two are known explicitly. However, the nature of the propagation problem only allows direct knowledge of the received seismograms. In the following syntheses, the approach taken is to obtain synthetic seismograms from the response of the system model of the crust to incident waveforms created on the basis of simple and plausible assumptions. Then, comparisons between the synthetic and experimental seismograms are expected to demonstrate the usefulness of the linear systems approach and the validity (in part at least) of the Alberta crust models for propagation problems at low frequencies.

It is arguable that the inverse approach which strives to obtain the input waveform or the crustal response function from the experimental seismograms is scientifically better. However, it is evident that assumptions on both the nature of the waveform and the crustal response function will still be required for comparison. Thus, by the inverse approach, comparisons can be directed only between computed and assumed solutions. However, the creation of synthetic seismograms allows the direct comparison of solutions (which are dependent on the applied assumptions) with the reality of the experimental seismograms.

By simulating the continuous linear systems crust models using the methods discussed in Chapter II, time domain responses of the crust to any input displacement waveform can be calculated. A FORTRAN simulation program for these syntheses is listed in Appendix IV. A requirement of this digital synthesis procedure is that each layer transit time is an integer multiple of the sampling interval. However, if the sampling interval is chosen small enough to allow a Nyquist frequency beyond the frequencies of interest, the requirement is not particularly restrictive. The experimental seismograms used in this work are band limited to frequencies below about 5 Hz. The FORTRAN program of Appendix IV assigns a minimum layer transit time of one time sample interval. For the following syntheses the time increment of 0.05 seconds has been used for comparisons with the digital experimental data.

Vertical component synthetic responses of the upper sedimentary portion of the LED crust model to an example arbitrary incident P displacement waveform at normal and 30° angles are shown in Figure 25. The reverberations of the primary motion lasting several seconds due to long path multiples within the modelled crust are particularly notable. The small scale high frequency character results from shorter path multiples

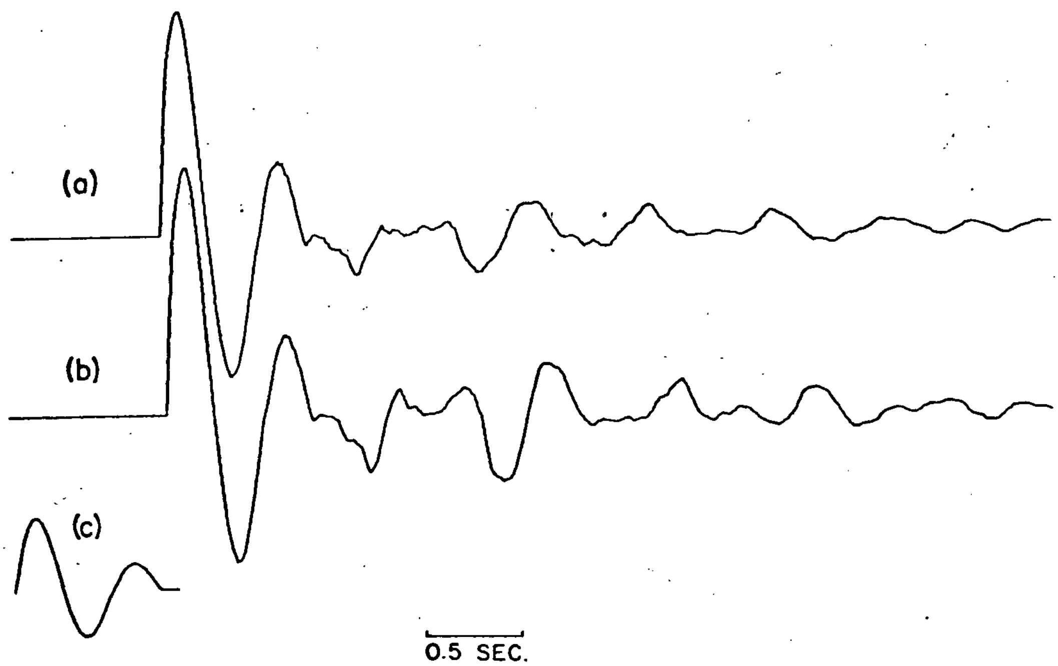

Fig. 25. Comparison of non-normal (a) and normal (b) incidence synthetic seismograms. Wavelet (c) incident on the Precambrian-Cambrian boundary at 30° produces synthetic seismogram (a), at normal incidence produces synthetic seismogram (b).

within the thinnest layers. For the 30° incidence synthetic response, the late reverberations arrive earlier than the corresponding reverberations for normal incidence. In frequency solutions this same effect appears as a displacement of the reverberation spectral peaks toward higher frequencies as the incidence angle increases. (This effect can also be noted in Figures 17 and 18). For non-normal incidence, the horizontal motion response is also available. The method permits the P and S waveforms retransmitted into the basement to be found but these were not generally used in this work.

3.14 Syntheses with Layer Attenuation

Causal minimum phase attenuation within each layer of the crust is allowed in the time domain syntheses by the inclusion of the attenuation time operators $a_i(t)$ (see Chapter II) where each operator is the impulse response of the attenuating layer for one transit. In this work, the Futterman (1960) absorption model (A1,D1) described earlier has been used to compute the time incremented attenuation operators which represent each layer for its particular Q and transit time. An example of one such attenuator impulse response of the post Alberta crustal layer formation with Q=23 is presented in Figure 26. It is particularly significant that its response rapidly decays to values near zero by 0.1 seconds following onset. The transit time through the post Alberta formation at its P-wave phase velocity (undispersed) is approximately 0.23 seconds which is considerably longer than this effective 0.1 second "length" of the operator. The effective "length" increases with decreasing Q. Therefore, other crustal layer formations which have higher Q's determine attenuation operators which are even shorter relative to their layer transit times.[5]

---

[5] The FORTRAN simulation program of Appendix IV demands that the operator is shorter than the layer transit time which limits layer Q's to values greater than approximately 5. Although such Q's are already unrealistically low, program modifications could be made to allow the very long operators which correspond to arbitrarily low Q's.

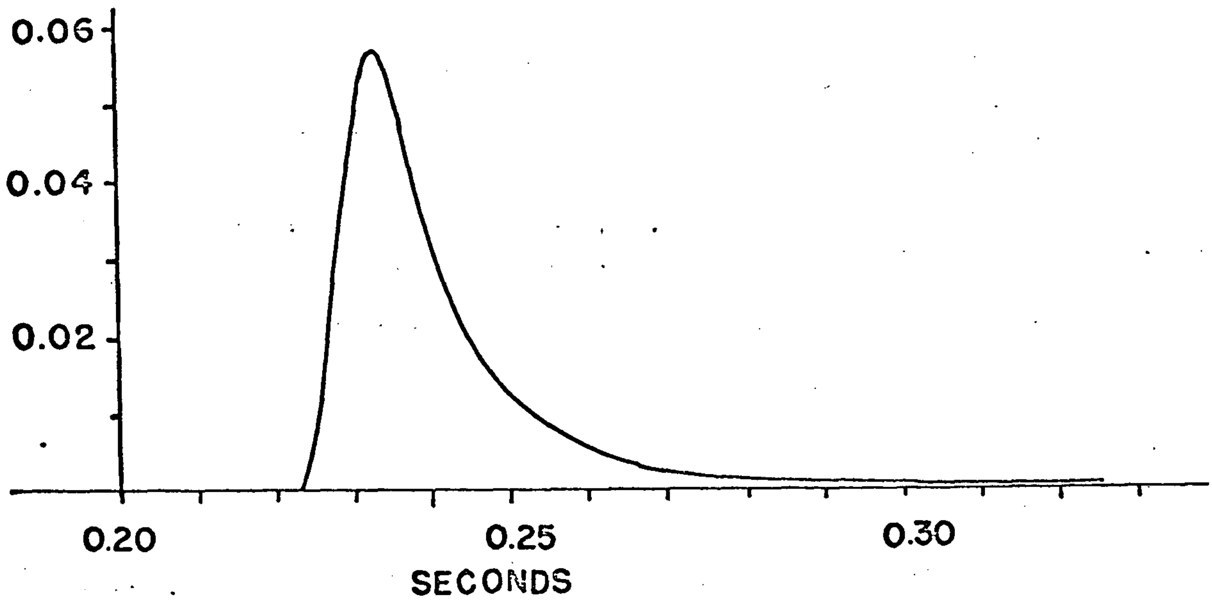

Fig. 26. The impulse response of layer 1 of the crustal section (Table I) assuming causal attenuation with Q=23. Assuming the Futterman attenuation description the non-attenuated impulse would arrive at 0.23 seconds. The amplitude scale is arbitrary.

The time incremented layer attenuators must be sampled and properly normalized to preserve the relative spectral response. For the 0.05 second sampling interval, the layer attenuator operator weights for the P and S motions of all model layers are given in Table IV. For each layer, the Q values represented by these attenuator operators are approximately equivalent for both P and S motions to those given in Table II. However, several of the thinnest model layers produce such small attenuation in one transit that no broadening or dispersion of an

TABLE IV

ATTENUATOR WEIGHTS FOR THE 0.05 SECOND SAMPLING INCREMENT

FORMATION	Q	P WEIGHTS	S WEIGHTS
Post Alberta	23	0.839,0.139,0.022	0.621,0.320,0.044,0.015
Alberta	30	0.932,0.06	0.831,0.154,0.015
Blairmore	30	0.953,0.047	0.947,0.053
Wabumum	100	1.0	1.0
Ireton	30	1.0	1.0
Cooking Lake	100	1.0	1.0
Elk Point	100	1.0	1.0
Cambrian	50	0.979,0.021	0.974,0.026
Precambrian	200	0.946,0.054	0.940,0.060
Sub-Layer I	500	0.915,0.085	0.815,0.168,0.017
Sub-Layer II	500	0.946,0.054	0.940,0.60

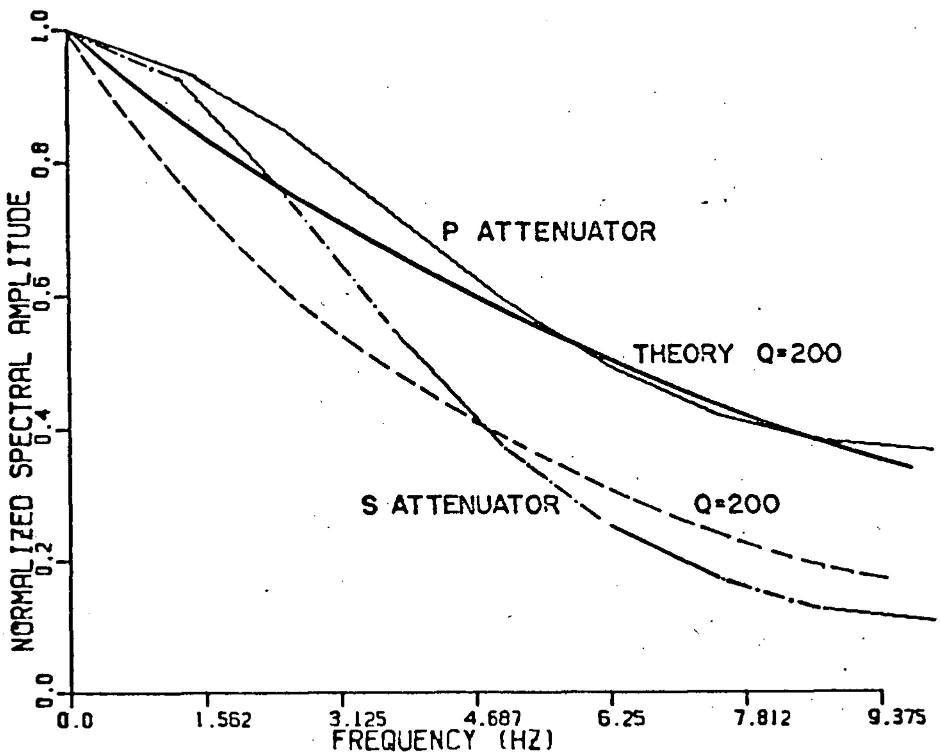

Fig. 27. The theoretical frequency response of the crust for one passage of an impulse for average Q=200 compared to the frequency response due to the sum of the time domain attenuation operators of Table IV. The value Q=200 is near the average model Q value of 186.

impulse can be seen on the 0.05 second time scale. For these layers, the single weight value unity which corresponds to infinite Q or zero absorption must be applied. The spectral response of the layer attenuators for one transit of an impulse through the total crustal section is compared to the theoretical spectral amplitude response for an average

Q equal to 200 (Figure 27). At the low frequencies, it is evident that the computed layer attenuation operators underestimate the average Q while they slightly overestimate Q at high frequencies. Arbitrarily better agreement can be achieved by using smaller time sampling intervals at the expense of increased computational time. However, the chosen attenuators are considered to be an adequate description of attenuation in the following syntheses.

Normal incidence synthetic crust responses for the upper sedimentary portion of the crust model and for the waveform used in the syntheses of Figure 25 show the effect of increasing the crustal attenuation (Figure 28). The infinite Q response is compared to the crust response with the appropriate attenuators of Table IV and to another response for which Q was arbitrarily chosen to be approximately 15 in every layer. The significant dispersion effects on the initial waveform and the preferential removal of the high frequency character are evident. The apparent energy and the effective length of the record are also reduced.

3.15 Impulse Synthetic Crustal Responses

The Dirac delta function is often a convenient input signal for many continuous linear systems problems. However, numerical simulations with infinite amplitude zero length impulses are not possible. Rather, it is useful to represent the impulse area numerically and compute the areas of the response impulses. Synthetic crust responses to a 30° incidence P impulse at the Mohorovicic discontinuity for the three crustal models are presented in Figure 29. Significant similarity in both the vertical and horizontal component syntheses for the three station crust models is evident.

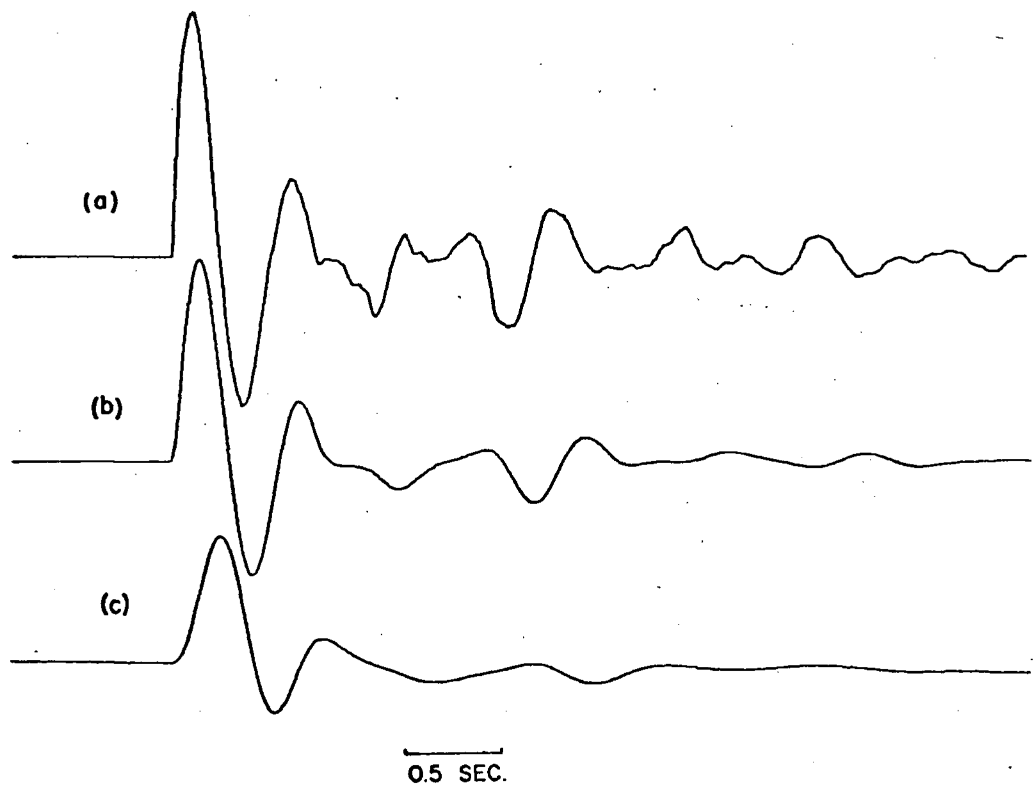

Fig. 28. Normal incidence synthetic seismograms dependence on Q. Infinite Q (a) is compared to the model Q values of Table IV (b) and to an average crustal Q=15 (c). Note the dispersion of the primary arrival. The incident waveform of Figure 25 has been used.

A larger scale P impulse normal incidence synthetic response for the LED crust model is shown in Figure 30. Several of the reverberation multiples which cause delayed impulses are designated by integer sets. For these, each boundary of the crust model is numbered from 0 for the surface to 11 for the crust-mantle boundary. The first integer represents the first reflection; the next represents the

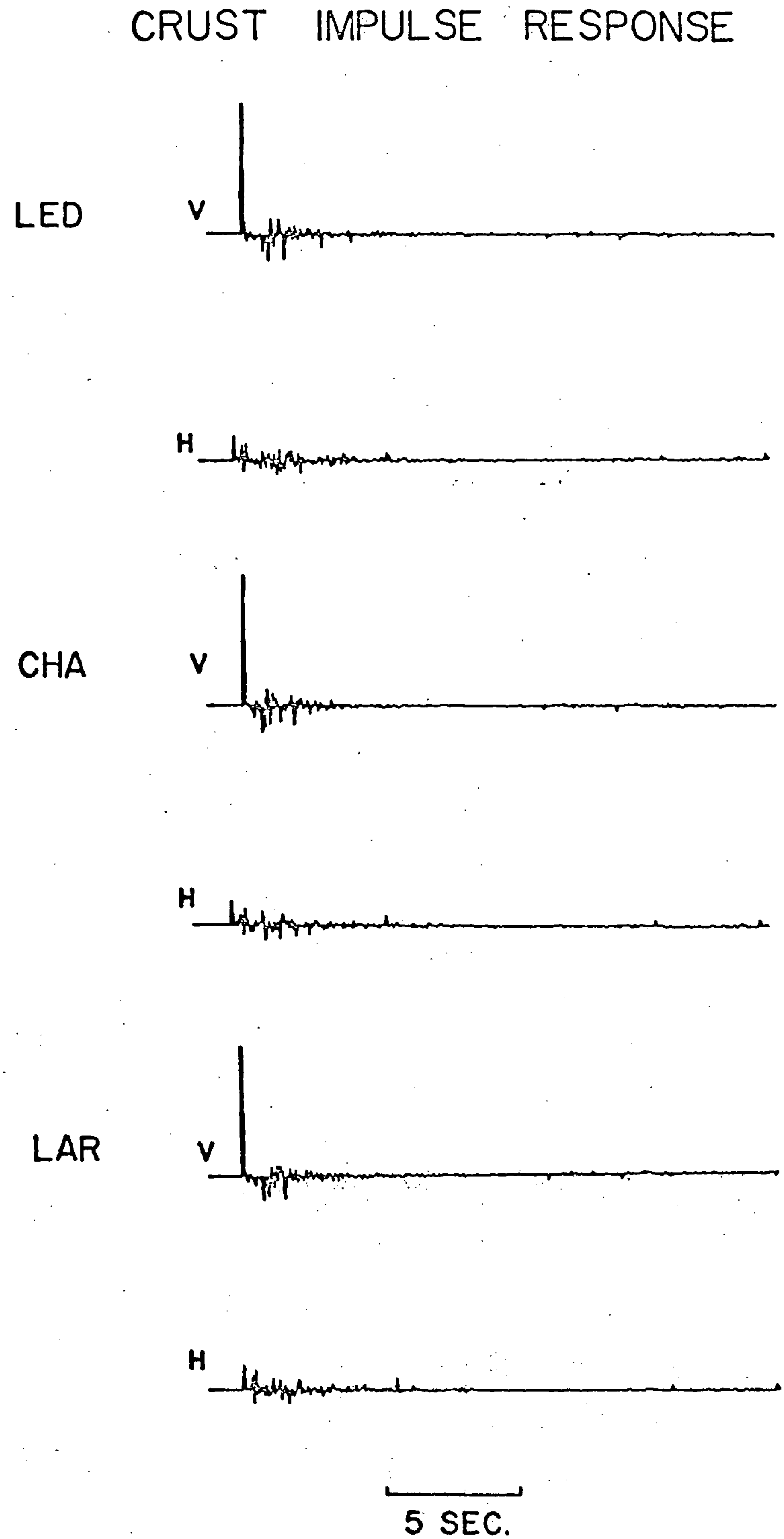

Fig. 29. The vertical and radial horizontal synthetic impulse responses of the three crustal sections representing the three stations.

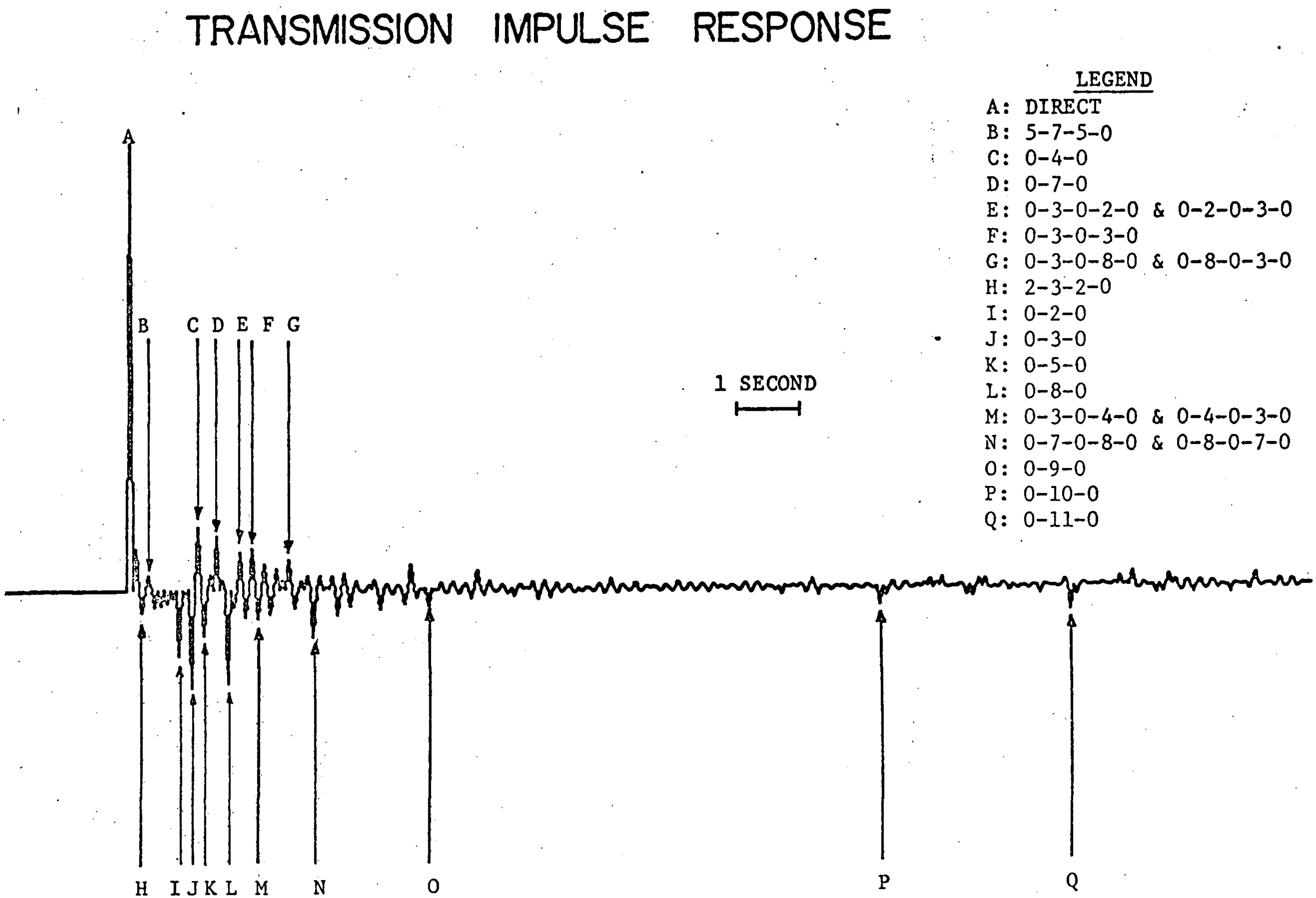

Fig. 30. The normal incidence synthetic impulse response for the LED crustal section. Various multiples or reverberations are designated by letters. The legend describes the internal reverberation paths which cause these later arrivals.

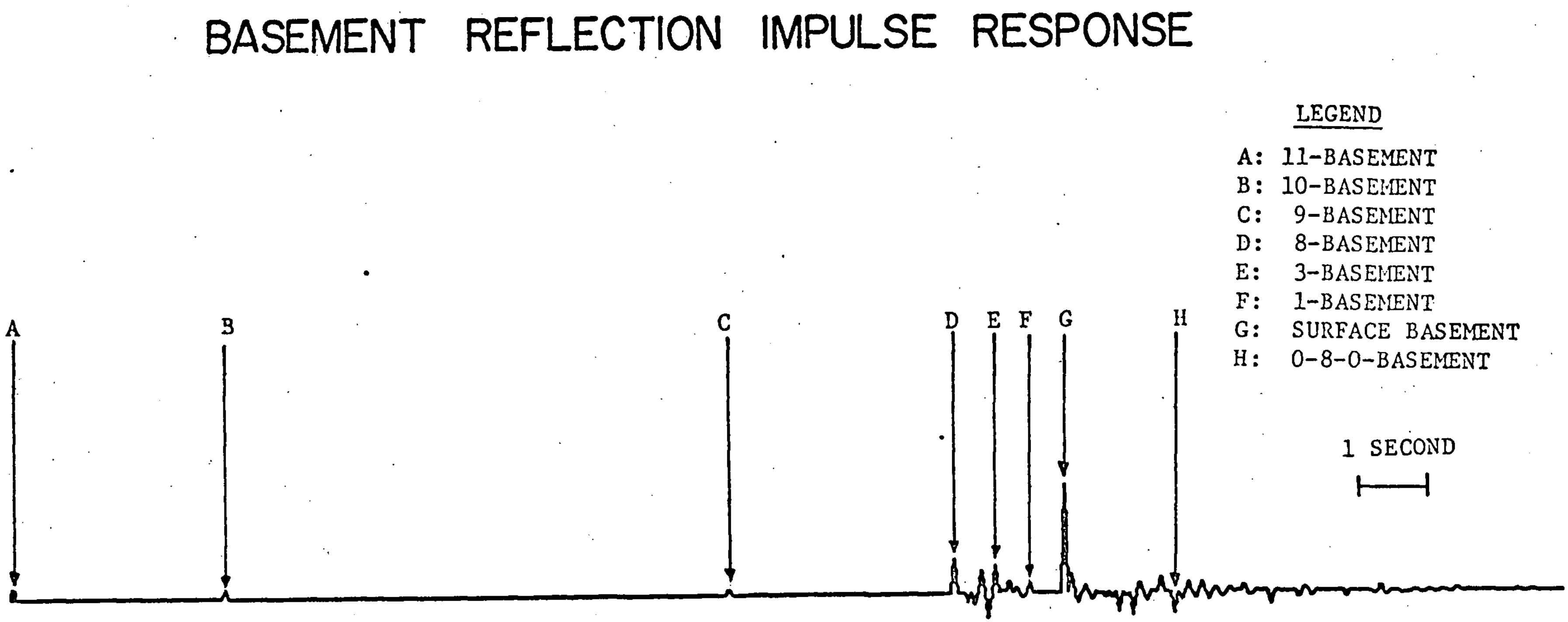

Fig. 31. The basement reflected wave synthetic impulse response for the LED crustal section. Reflections from various internal crust boundaries into the basement are designated by letters. One reverberated multiple, H, is also shown. The legend describes the internal reverberation paths causing the later arrivals.

second and so on. The last integer represents the boundary on which the motion is observed. Primary multiples which first reflect from the surface and then from an internal boundary before returning to the surface usually display the largest amplitudes. However, some high amplitude impulses from entirely internal multiples are also evident. For example, the multiples designated (2-3-2-0) and (5-7-5-0) are not reflected from the surface. The particularly strong (0-3-0) multiple due to the Wabumum upper boundary and surface and the (0-8-0) due to the Precambrian upper boundary should affect the early character of the experimental seismograms. The impulse response displacement wave propagated back into the mantle shows several reflections from the major boundaries of the crust (Figure 31). These waveforms reflected back into the mantle can retain much character created in crustal reverberations.

3.16 Incident Waveform Models

The computation of any reasonable synthetic seismogram requires a realistic input waveform for the linear systems model which is based upon the known properties of the mantle path and the nature of seismic source motions. But, because the form of P motions at sources are not generally known, plausible assumptions must be applied.

For the Novaya Zemlya event, which resulted from a Soviet underground nuclear test of a device in the 0.1 to 1.0 megaton TNT equivalence range, the results of Werth and Herbst (1967) for explosion waveforms have been considered. Their work on small nuclear explosions (Werth and Herbst, 1967; Figure 1) shows that the radial displacement time function near an explosion source has the form of a positive pulse of short duration (less than 0.5 seconds for their three examples). Based on their evidence, an impulse displacement time function source model has been assumed for the Novaya Zemlya event. Werth and Herbst suggested that waveforms at teleseismic distances are not highly dependent upon the exact nature of the explosion source motion pulse so that the impulse approximation should be an adequate description. It should be noted that the field seismograph instruments observed only a band of frequencies below about 5 Hz. Assuming a linear nature for the wavemotions from the source through the mantle, only those source frequencies within the instrument bandpass can affect the seismogram. Consequently, the "impulse model" merely requires that the source waveforms look like an impulse below 5 Hz. The exact infinite impulse of infinitesmal duration is not required.

An impulse model is also particularly attractive because it imposes the minimum possible character on the source displacement motions. It determines no spectral amplitude or phase character and describes only an origin time; it is the maximum entropy (minimum information) waveform.

The chosen events in this work were limited to those exhibiting very short P coda. Since crustal reverberations can only lengthen the P coda, the incident P wave must have even shorter duration. Among the events, the LED recording of the Venezuela event has character which is surprisingly similar to the Novaya Zemlya seismogram. This should indicate that the waveforms incident on the crust were also quite similar. Furthermore, since the two events occurred at nearly equal epicentral distances from the stations, the effects of the mantle path should also be similar. This implies similarity in the source generated waveforms, at least as seen by the narrow band instruments. However, the remaining earthquakes do not appear to generate such strikingly similar seismograms and the strict impulse model cannot be used as confidently.

Some step displacement source models were also considered and syntheses using these compared to impulse source syntheses. It seems reasonable that a step model could better represent elastic motions near the source of an earthquake fault.

Following the lead of Werth and Herbst (1967) and Carpenter (1967), the effect of the mantle path on the source waveform is considered to be due only to absorption and attending dispersion. Carpenter shows the Futterman absorption model obeys a principle of similarity which he describes:

$$F(t,T/Q) = (Q/T)F_o(tQ/T) \tag{3-7}$$

where $F(t,T/Q)$ is the waveform amplitude at time t for an event-to-station travel time of T and a medium with quality Q. Thus, $F_o(tQ/T)$ parametrically describes only the shape of the waveform and T/Q is a characteristic time which is the essential parameter of F_o. In Figure 32, Futterman model responses to impulse displacement source motions are compared for various mantle Q's ranging from 500 to 3000 for a source to station travel time of 600 seconds. For these responses, the characteristic time parameter ranges from 1.2 seconds down to 0.2 seconds. the 10 minute travel time corresponds roughly to the epicentral distance to the Novaya Zemlya and Venezuela event sources or approximately 55°.

The combined source motions and mantle absorption waveforms may be further combined with the seismograph response to determine the

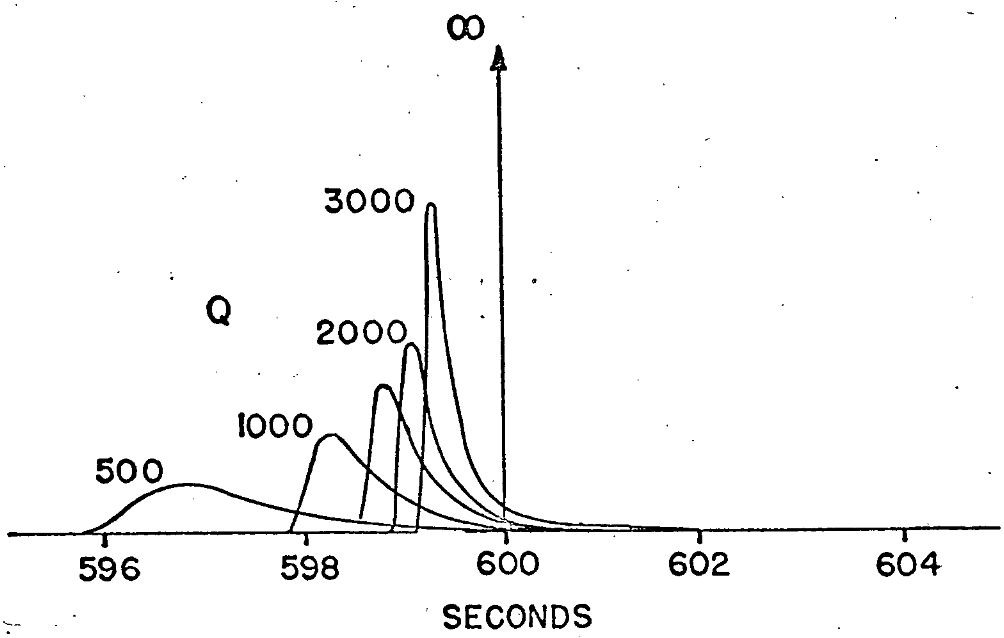

Fig. 32. The effect of various mantle path average Q values on an impulse source displacement motion which has travelled 10 minutes at the undispersed phase velocity through the mantle. Q=1500 has been found to be the best representation for construction of synthetic seismograms in this work.

input wavelet to the systems model. Since the source motions, mantle absorption and instrument response characteristics are all linear their order of combination does not affect the resultant seismogram syntheses. Wavelets obtained by the convolution of the seismograph impulse response and the response of the mantle absorption model to impulse and step source motions for various T/Q are presented in Figure 33. Similar wavelets were obtained by Carpenter using somewhat different instrument response characteristics.

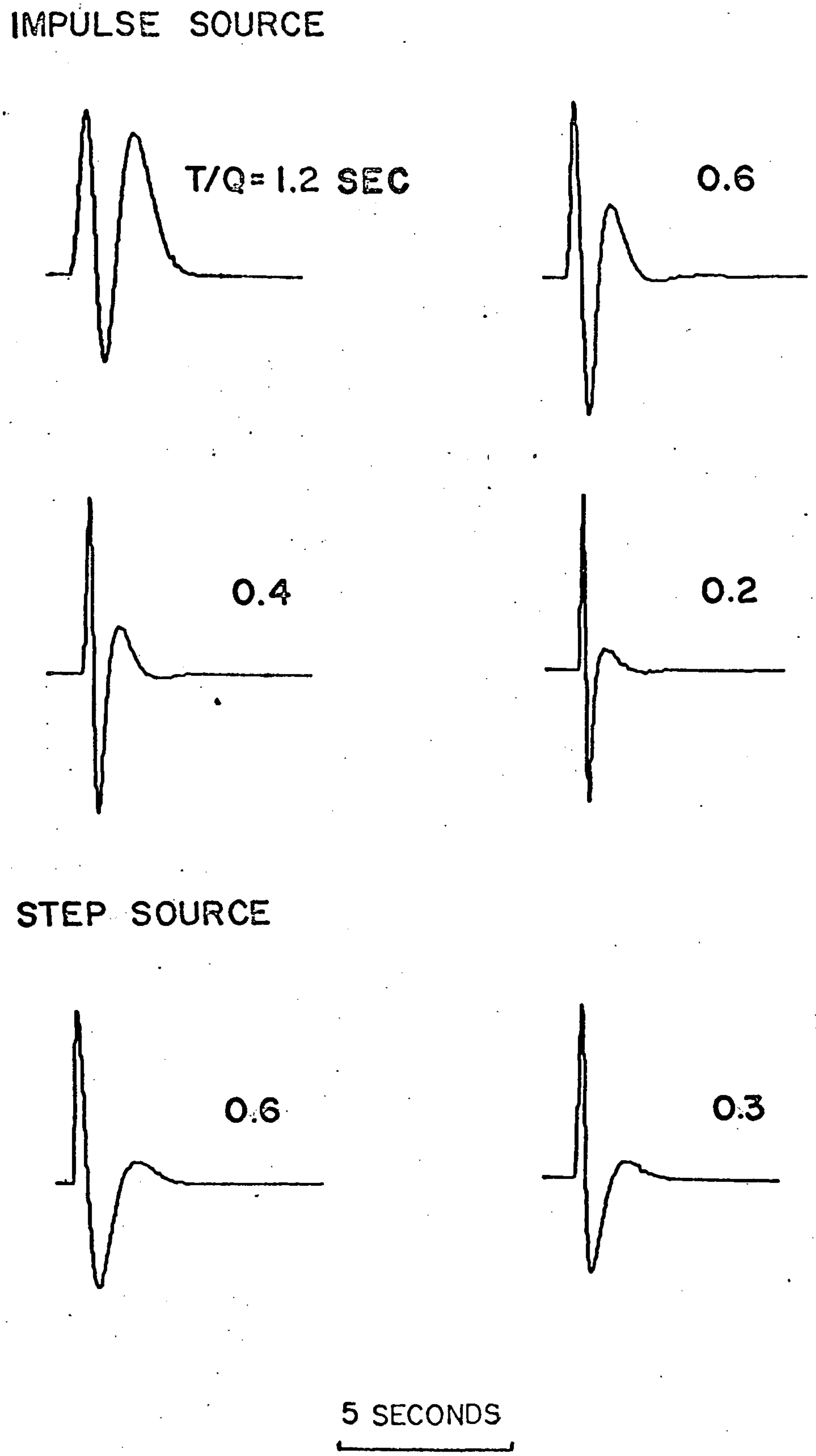

Fig. 33. Wavelets constructed by convolution of the seismograph response with absorbing mantle responses for various T/Q parameters for both impulse and step sources. T/Q=0.4 seconds has been found to be the best representation for seismogram synthesis at an epicentral distance of 55°.

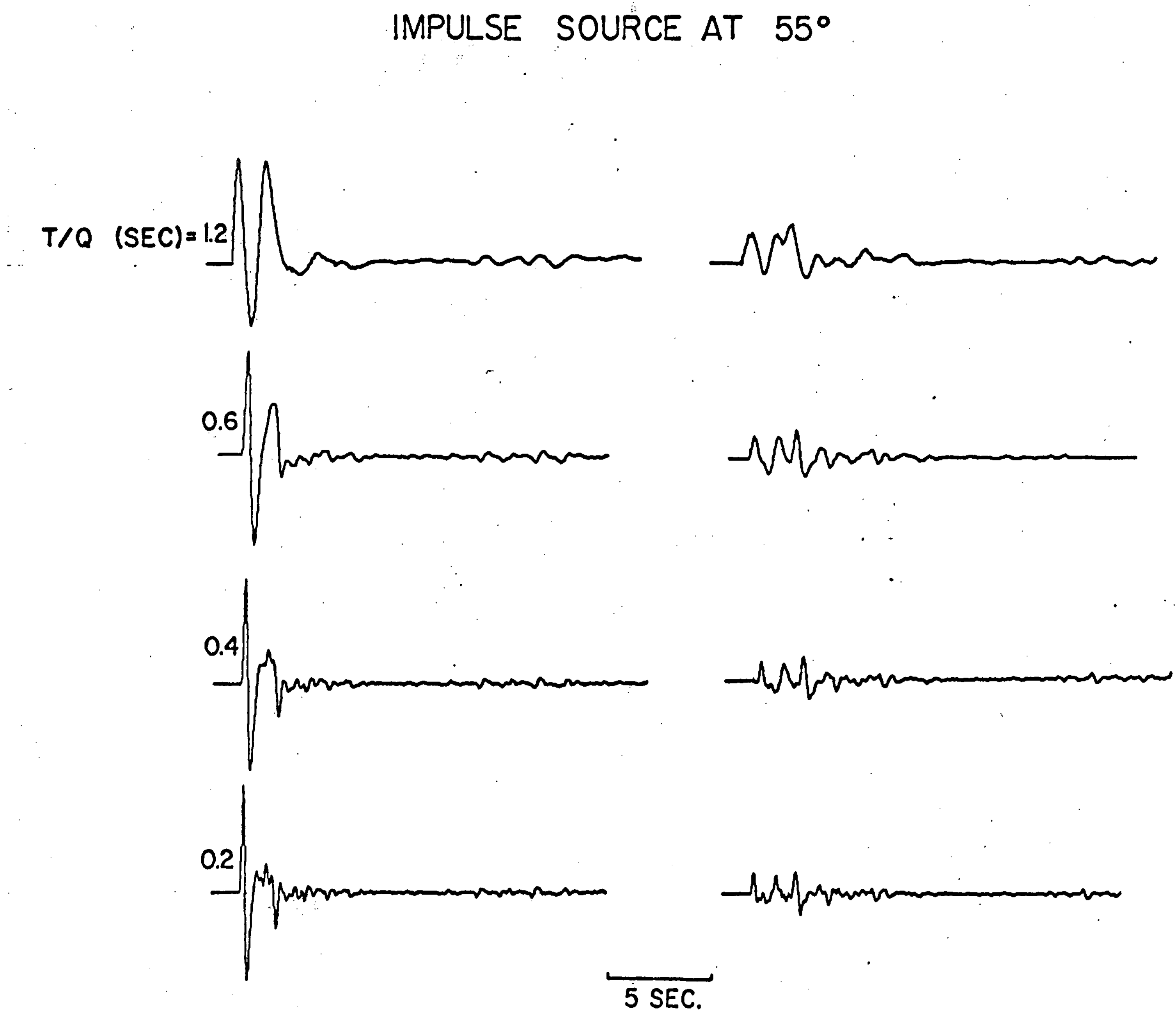

Fig. 34. Vertical and horizontal component synthetic seismograms for various T/Q wavelets of the form shown in Figure 32 for impulse source motions.

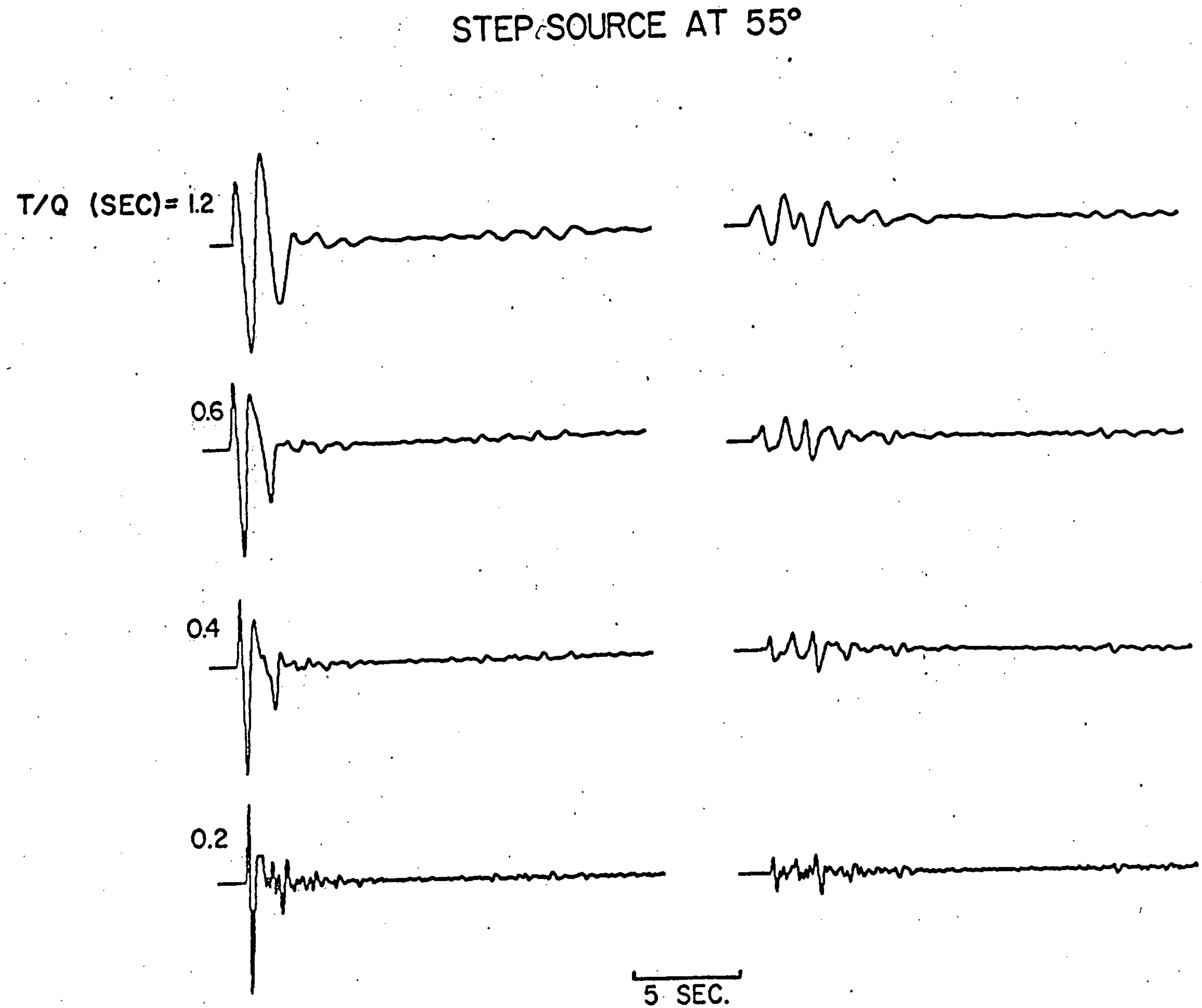

Fig. 35. Vertical and horizontal component synthetic seismograms for various T/Q wavelets for step source motions.

Using these computed wavelets for the input source to the linear systems model of the LED crust for 30° incidence (which corresponds to the 55° teleseismic distance) a set of synthetic seismograms have been calculated (Figure 34). Step source synthetic seismograms are also presented (Figure 35). Comparisons of these syntheses with the LED Novaya Zemlya and Venezuela records indicates that the impulse source model for T/Q = 0.4 seconds best represents the frequency character of the initial motions. (These two particular events are used in this comparison because their epicentral distances result in the 30° incidence angle used in this synthesis). Carpenter suggested that for teleseismic P waves, T/Q should approximate unity. However, those syntheses for T/Q = 1.2 seconds and 0.6 seconds lack high frequency character observed in the experimental records. Short duration source motions which could contain relatively more high frequency character than an impulse are physically unreasonable. It is better to retain the impulse model and require a lower T/Q = 0.4 seconds value which appears to best fit experiment. This T/Q value determines a mantle Q=1500. Q's in the mantle exceeding this (to 6000) for P waves with frequencies near 1 Hz have been reported by several investigators (Jackson and Anderson, 1970) so that this mantle absorption model is not unrealistic. For all subsequent syntheses Q has been held constant to 1500 while T/Q varies with travel time.

Synthetic seismograms for impulsive displacement sources at 55° and 85° epicentral distances are shown in Figure 36. In these computations, the internal crustal attenuation has been included using the attenuator weights of Table IV. For the 55° distance, the travel time determines T/Q = 0.4 seconds; for 85°, T/Q = 0.6 seconds. Impulse

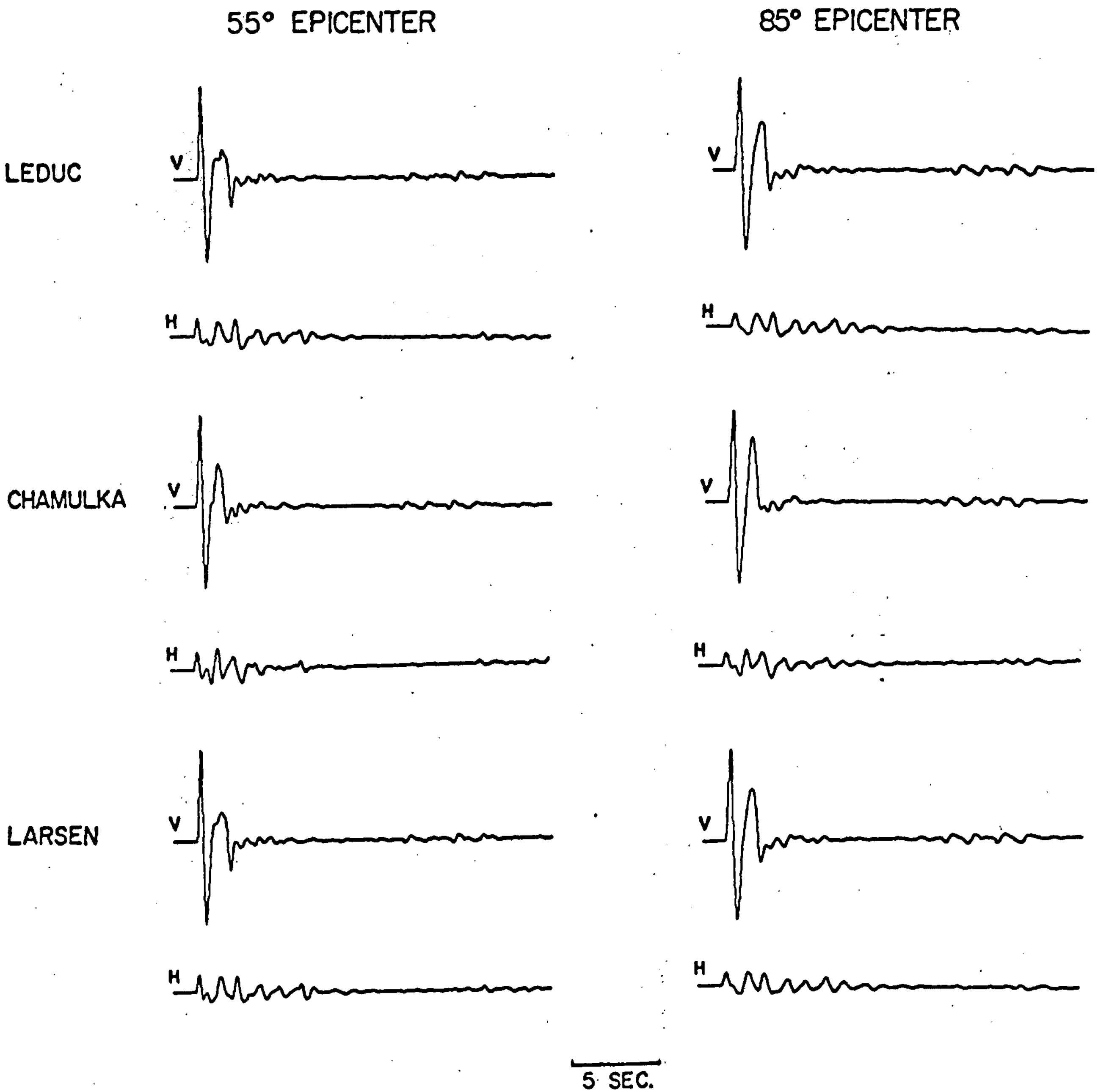

Fig. 36. Impulse source motion synthetic seismograms for 55° and 85° epicentral distances. The mantle Q has been chosen to be 1500 for all syntheses. Internal crustal absorption (causal) of Table II has been included.

source wavelets with these mantle absorption model parameters were used as systems inputs. A comparison between a vertical component non-attenuating crust seismogram and the corresponding absorbing crust seismogram showed little difference. Only a slight reduction in the apparent high frequency content was evident.

3.17 Seismogram Syntheses

Most of the recorded vertical component seismograms possess early character which is quite similar to the equivalent syntheses. In particular, the apparent frequency of the first few cycles of the synthetic responses compares well to the frequency nature of the early part of all of the equivalent experimental seismograms. This is not trivial, since the mantle Q assumption which actually determines the incident wave frequency content was based only on the Novaya Zemlya and Venezuela records. The frequency content of the syntheses for the larger 85° epicentral distance also favourably compares with the experimental records. The horizontal records are not so visibly comparable. This partially results from the greater relative noise contamination of the low amplitude horizontal motions. Noise also reduces the possibility of good comparisons with low amplitude vertical motions in the later portions of the vertical component records. It is apparent that all the recorded seismograms, and particularly those from the Novaya Zemlya, Kurile Islands and Ryukyu events, do not decay as rapidly as the equivalent syntheses. Furthermore, the Kurile Islands and Ryukyu events show distinct secondary arrivals (probably pP) within the first 25 seconds which suggests that the incident waveforms are longer and more complex than these simple source and mantle absorption models can describe. It would be difficult to create the theoretically possible but complicated source motion models which would exactly describe the experimental records. Therefore, it is reasonable to restrict any comparisons to the initial few seconds of record which are dominated by the beginning of the incident waveform resulting from the onset of source motions. However, even within these first few seconds, many discrepancies between the theory and experiment are still obvious.

In particular, the synthetic seismograms appear to exaggerate the amplitude of the first pulse of onset. This primary character should result from the instrument response to the surface motions generated by the very first passage of the incident waveform through the crust to the surface. Internal crustal reverberations can only slightly affect these very early mtoions. Thus, it becomes obvious that the source motion or mantle attenuation models are not completely adequate. Most probably, the source displacements are not as abrupt as the impulse and step displacement models. But, since the experimental seismograms are contaminated by background noise, precise correlations could not have been expected even from exact source motion models.

In the following more detailed comparisons between theory and experiment, the LAR recordings from the Venezuela event are not used because of their high apparent noise levels.

3.18 Comparisons of the Syntheses and Records for 55° Epicenter

Neglecting the noisy LAR Venezuela records, all vertical component seismograms show some motions which are correlatable with the

COMPARISON OF EXPERIMENTAL AND SYNTHETIC

SEISMOGRAMS FROM STATION LED

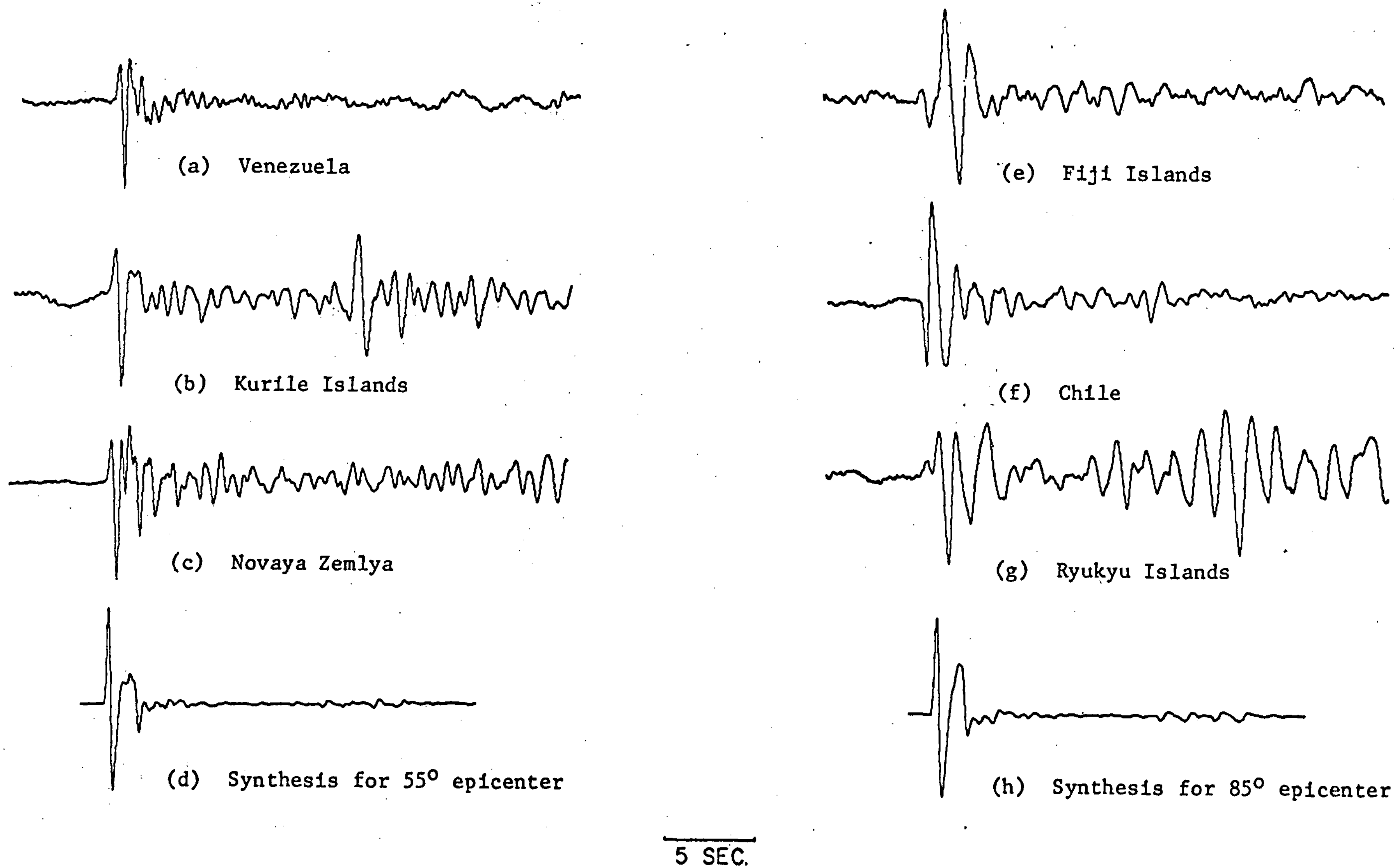

Fig. 37. A comparison of the vertical synthetic seismograms with the experimental seismograms of Figure 16 for station LED.

equivalent synthetic motions to beyond 4 seconds following onset. One such notable correlatable feature is a strong, short negative pulse at 2 seconds which corresponds to a consistent experimental feature (compare Figure 36 and Figure 16a,d,e; see also Figure 37). This pulse could result from the strong reverberation of the initial motions involving a reflection from the free surface and the upper Precambrian boundary. (See Figure 30). Another broad positive pulse beginning at 1 second appears to correlate with similar but more complicated experimental features. The synthesized pulses particularly well represent those of the Kurile Islands events in both general character and relative amplitude. The LED Novaya Zemlya seismogram contains more character in this area (near 1 second) than the equivalent syntheses. However, the CHA synthesis and record compare surprisingly well. The several strong multiples which arrive between 1 and 2 seconds (Figure 29) must largely contribute to the formation of this broad characteristic pulse.

Apart from the preceding comparisons, it is also possible to correlate the vertical component syntheses and the equivalent experimental seismograms on a peak to peak basis to almost 5 seconds following onset (compare Figure 37). However, the theory predicts amplitudes for these later motions which are lower than those observed. This indicates that these later motions are at least partially generated by some continuing incident wavemotion at the lower crustal boundary. Also, noise could contribute. Little significant correlation is obvious between any of the horizontal seismograms and their equivalent syntheses.

3.19 Comparisons of the Syntheses and Records for 85° Epicenter

Only the Fiji event vertical seismograms display initial character which directly corresponds to the equivalent syntheses (compare Figure 37). However, the Chile event records can also be made compatible by inversion (multiplication by -1). This suggests that the source motions for this event are better represented by a dilatational impulse model rather than the compressional impulse model used. The Ryukyu seismograms possess such very complex early character that correlations are somewhat ambiguous. The broad pulse feature at 1 second followed by the narrow pulse at 2 seconds is also evident on these synthetic seismograms and again corresponds to similar features of the Fiji and Chile records. For a Fiji correlation, the small amplitude precursor to the strong positive motion of the early record has been neglected. The horizontal motions from this event also appear to compare quite favourably with the theory. However, the high background noise level makes a detailed comparison difficult.

3.20 Synthesis Using an Input Wavelet Obtained by Deconvolution

Ulrych (1970) has recently developed a method of separating the convolved incident wavelet from the crustal impulse response function in a seismogram using homomorphic non-linear filtering methods (Oppenheim et al, 1968). The technique requires no assumptions on the character of the wavelet except a choice of its representative length and requires no assumptions of crustal properties except linearity. Using his homomorphic deconvolution procedure on the LED Venezuela seismogram, Ulrych obtained a short (30 sample points) input wavelet which was used for the re-synthesis of the seismogram by the

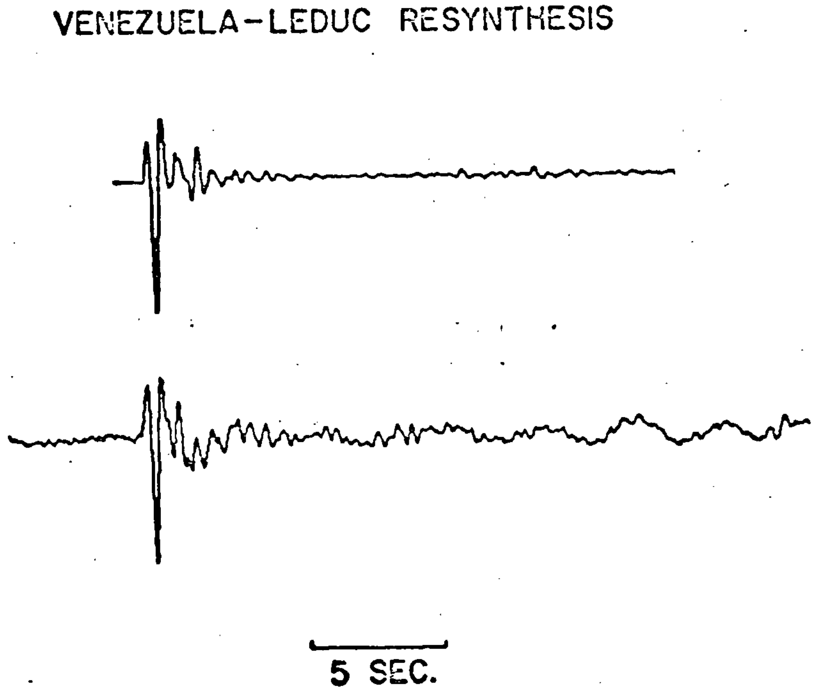

Fig. 38. A comparison of the vertical component LED seismogram for the Venezuela event (Event 1, Figure 16a) and the re-synthesis using the Ulrych wavelet. The internal crustal causal absorption of Table II has been included.

linear systems approach. (Figure 38). The seismogram synthesized with this wavelet provides a good test of the crust model and method.

It is not surprising that the synthesized seismogram is not identical to the experiments. Such a fortuitous result would demand an exact crust model and wavelet. However, the remarkable degree of similarity between the theory and experiment for the vertical component is extremely encouraging. The easily correlated character extends to almost 6 seconds following the onset. Since the input wavelet was only 1.5 seconds in length, it is obvious that these later motions are generated by the crustal response. The synthesis still poorly represents the horizontal component. Because the horizontal motions are mostly converted SV energy which arises at the internal crustal boundaries, it is apparent that significant model discrepancies must exist.

CHAPTER IV

CONCLUSIONS

4.1 Summary of Analyses

Between 0 and 2 Hz most of the experimental V/H spectral ratios exhibit general features which were theoretically predicted by the linear systems solutions. In particular, expected 0.7 and 1.7 Hz ratio peaks were found. However, except for such low frequencies, the spectral ratio comparisons between theory and experiment have revealed little further confirmation of the chosen crustal models. The observed correlations below 2 Hz suggest that on a scale determined by the long wavelengths of the low frequencies, the crust models are almost sufficient, but on a small scale, significant model discrepancies must exist. The effect of attenuation was virtually indeterminable experimentally since the spectral peaks which theory indicated should reveal crustal absorption properties were not consistent enough to derive any conclusions. However, the theoretical solutions conclusively demonstrated that attenuation effects are considerable beyond 2 Hz for a realistic crustal absorption model and must be included in any comprehensive ratio analysis. The visible effects of causal crustal attenuation of the time synthesized seismograms appeared to be slight. This, however, does not imply that attenuation cannot be important at higher frequencies.

The vertical-to-vertical experimental ratios showed little character as was theoretically predicted below 3 Hz. Unfortunately, the spectral detail necessary to distinguish and interpret relative crustal layering and absorption properties does not appear to be available.

Considering the extremely simple assumptions on source motions and mantle properties which were used for the time domain syntheses, the similarity between the early portions of the theoretical and most of the experimental vertical component seismograms was very encouraging. However, there was also a disturbing lack of correlation between the equivalent horizontal records and syntheses. The Ulrych homomorphic deconvolved input wavelet determined the best comparison between the theoretical synthesis and experiment. With these reasonable successes already achieved using the simplest of models for source motions, one could expect that better conceived input incident wavelets could provide some remarkably accurate syntheses.

The possible causes of any moderation of the success are varied. Background noise, inexact crustal models, scattering and possible non-linear effects could all contribute to discrepancies between theory and experiment. Among these possible factors, scattering effects due to inhomogenieties in the layers, non-plane interlayer boundaries and surface (topography) could invalidate this simple linear systems solution for a real sedimentary bedded crust. Chernov (Grant and West, 1965) has shown that the effect of scattering in an inhomogeneous medium increases rapidly with frequency. The correlations obtained at low frequencies is not inconsistent with this scattering hypothesis. Although, the chosen events appeared to possess large average signal-to-noise ratios, background noise dominates the P coda outside the signal band from 0.5 Hz to 3 Hz. This undoubtedly contributed to the lessened success at high frequencies.

It is possible that inaccuracy and insufficient detail in the crustal models has been attained using the interpolation between the available oilwell drill sites. Correlations between theory and experiment may be greatly improved at high frequencies by using more accurate models which would require more complete knowledge of the crust. Although the frequency domain computations can provide theoretically exact solutions for any model, further assumptions which generate model inaccuracies are necessary for digital time domain syntheses. For example, the time domain solutions require that the layer transit time for both P and SV motions is an exact integral multiple of the sampling increment. For the 0.05 second interval used in the thesis, the thinnest layers would exhibit both P and SV transit times precisely equal to this interval. Such difficulties could easily be overcome by reducing the sampling increment to obtain any desired level of accuracy. However, parallel increases in computer time and storage requirements must be tolerated.

4.2 Concluding Remarks and Suggestions

The linear systems solution of the multilayer propagation problem has already shown some particularly useful features. It becomes the first mathematical procedure to explicitly include layer attenuation for both normal and non-normal incidence although this extension has been suggested for the standard techniques. The fact that the theoretical P coda V/H ratio analyses for the crust and attenuation models used herein showed the significant dependence on attenuation beyond 2 Hz demonstrates that crustal absorption cannot be neglected in any complete propagation analysis using short period P-coda. Also, since attenuation showed little effect below 1 Hz, the previous V/H ratio work of several authors at low frequencies has been validated with respect to attenuation.

The linear systems approach has the particular advantage that the time and frequency formulations are completely parallel. This should aid in the conception of the relations between the characteristics of frequency and time solutions. Furthermore, two independent viewpoints should prove to be very useful.

The formulation admits analysis and solution using the large body of communications theory mathematics. Such methods have, in the past, been invaluable for the reduction and analysis of geophysical data. Their further application to the direct formulation of the propagation problem may prove as useful by providing new insights and producing generalizations of solutions.

It should be possible to extend solutions to include crustal properties which are non-linear. For example, appropriate non-linear operators which could describe possible non-linearities of crustal propagation could be inserted into the linearly restricted formulation and solved by the time synthesis approach. Since superposition is not strictly valid for non-linear systems, previous methods which require frequency incremented or modal solutions would not be sufficient in this regard. Also, the solution of sets of non-linear differential equations describing non-linear propagation would probably be much more difficult than the non-linear extension of the time domain systems solution. It may be difficult to conceive non-linearities in ideal infinitesmal strain propagation. But, in real crustal materials where scattering and absorption are known to occur, non-linear descriptions have been hypothesized (e.g., Walsh, 1966).

Although no solutions for incident S waves were attempted in this thesis, the linear systems formulation is directly applicable.

Furthermore, reflection seismology could be considered by a trivial extension of the normal incidence transmission problem. However, it is important to note that the systems formulation demands plane waves so that point sources within the crust cannot be allowed. Most other reflection seismic solutions also require plane waves, normal incidence, and neglect the effects of geometrical spreading which actually results from explosion sources.

The systems formulation may provide a new viewpoint which would permit a general solution of the important inverse problem. For ideally layered crusts, the layer transfer functions (see Appendix I) appear to contain all the information required to determine layer transit times and relative acoustic impedance variations for both normal and non-normal incidence conditions. It should be possible to obtain this information from the equivalent seismogram. This approach, however, cannot be so unambiguous as to determine layer velocities, densities and thicknesses. Inverse solutions are now being attempted.

The author feels that studies using the linear systems formulation could prove to be extremely fruitful for both more generalized propagation and inverse solutions.

REFERENCES

Alberta Society of Petroleum Geologists. 1964. Geological history of western Canada.

Anderson, D.L., Ben-Menahem, A. and Archambeau, C.B. 1965. Attenuation of seismic energy in the upper mantle. J. Geophys. Res. 70, pp. 1441-1448.

Basham, P.W. 1967. Time domain studies of short period teleseismic P phases, M.A.Sc. Thesis, University of British Columbia.

Bohn, E.V. 1963. The transform analysis of linear systems. Addison-Wesley, Reading. p. 100.

Carnahan, B., Luther, H.A., and Wilkes, J.O. 1969. Applied numerical methods. Wiley, New York. p. 80.

Carpenter, E.W. 1967. Teleseismic signals calculated for underground, underwater and atmospheric explosions. Geophysics, 32, pp. 17-32.

Claerbout, J.F. 1968. Synthesis of a layered medium from its acoustic transmission response. Geophysics, 33, pp. 264-269.

Clowes, R.M. and Kanasewich, E.R. 1970. Seismic attenuation and the nature of reflecting horizons within the crust. J. Geophys. Res. 75, pp. 6693-6705.

Cooley, J.W. and Tukey, J.W. 1965. An algorithm for the machine calculation of complex Fourier series. Math. of Comp. 19, pp. 297-301.

Cumming, G.L. and Kanasewich, E.R. 1966. Crustal structure in western Canada, Final Rept., Contract AF 19 (628)-2835, AFCLR, Bedford, Mass.

Deas, A.T. 1969. A crustal study using teleseismic P phases recorded near Port Arthur, Ontario. M.Sc. Thesis, University of British Columbia.

Ellis, R.M. and Basham, P.W. 1968. Crustal characteristics from short period P waves. Bull. Seism. Soc. Amer. 58, pp. 1681-1700.

Frasier, C.W. 1970. Discrete time solution of plane P-SV waves in a plane layered medium. Geophysics, 35, pp. 197-219.

Futterman, W.I. 1962. Dispersive body waves. J. Geophys. Res. 67, pp. 5279-5291.

Goupillaud, P. 1961. An approach to inverse filtering of near-surface layer effects from seismic records. Geophysics, 26, pp. 754-760.

Grant, F.S. and West, G.F. 1965. Interpretation theory in applied geophysics. McGraw-Hill, New York. pp. 48, 200.

Haskell, N.A. 1953. The dispersion of surface waves on multilayered media. Bull. Seism. Soc. Amer. 43, pp. 17-34.

Ibrahim, A.K. 1969. Determination of crustal thickness from spectral behaviour of SH waves. Bull. Seism. Soc. Amer. 59, pp. 1247-1258.

Jackson, D.D. and Anderson, D.L. 1970. Physical mechanisms of seismic-wave attenuation. 1970. Rev. Geophys. and Space Phys. 8, pp. 1-63.

Knopoff, L. 1956. The seismic pulse in material possessing solid friction, I: Plane waves. Bull. Seism. Soc. Amer. 46, pp. 175-183.

Knopoff, L. and MacDonald, G.J.F. 1958. Attenuation of small amplitude stress waves in solids. Rev. Mod. Phys. 30, pp. 1178-1192.

Knopoff, L. and MacDonald, G.J.F. 1960. Models for acoustic loss in solids. J. Geophys. Res. 65, pp. 2191-2197.

Knopoff, L. 1964. Q. Rev. Geophys. 2, pp. 625-660.

Kuo, B.C. 1962. Automatic control systems. Prentice Hall, Englewood Cliffs, New Jersey. p. 40.

Lindsey, J.P. 1960. Elimination of seismic ghost reflections by means of a linear filter. Geophysics, 25, pp. 130-140.

McDonal, I.J., Angona, F.A., Mills, R.L., Sengbush, R.L., Van Nostrand, R.G. and White, J.E. 1958. Attenuation of shear and compressional waves in Pierre Shale. Geophysics, 23, pp. 421-439.

Mueller, S. and Ewing, M. 1962. Synthesis of normally dispersed wave trains by means of linear systems theory. Lamont Geological Observatory, Columbia University, Contribution No. 559.

Oppenheim, A.V., Schafer, R.W. and Stockham, T.G., Jr. 1968. Non-linear filtering of multiplied and convolved signals. Proc. IEEE 56, pp. 1264-1291.

Phinney, R.A. 1964. Structure of the Earth's crust from spectral behaviour of long period waves. J. Geophys. Res. 69, pp. 2997-3017.

Press, F. 1964. Seismic wave attenuation in the crust. J. Geophys. Res. 69, pp. 4417-4418.

Richter, C.F. 1958. Elementary seismology. Freeman, San Francisco. p. 670.

Robinson, E.A. and Treitel, S. 1966. Seismic wave propagation in layered media in terms of communication theory. Geophysics, 31, pp. 17-32.

Savage, J. C. 1965. Attenuation of elastic waves in granular mediums. J. Geophys. Res. 70, pp. 3935-3942.

Sherwood, J.W.C. 1962. The seismoline, an analog computer of theoretical seismograms. Geophysics, 27, pp. 19-34.

Thomson, W.T. 1950. Transmission of elastic waves through a stratified solid medium. J. Appl. Phys. 21, pp. 89-93.

Tullos, F.N. and Reid, A.C. 1969. Seismic attenuation in Gulf coast sediments. Geophysics 34, pp. 516-528.

Ulrych, T.J. 1971. Application of homomorphic deconvolution to seismology. Submitted for publication.

Walsh, J.B. 1966. Seismic wave attenuation in rock due to friction. J. Geophys. Res. 71, pp. 2591-2599.

Ware, J.A. and Aki, K. 1969. Continuous and discrete inverse-scattering problems in stratified elastic medium. J. Acoust. Soc. Amer. 45, pp. 911-921.

Werth, G.C. and Herbst, R.F. 1963. Comparisons of amplitudes of seismic waves from nuclear explosions in four mediums. J. Geophys. Res. 68, pp. 1463-1475.

Williams, G.D. and Burk, C.F., Jr. 1964. Geological History of Western Canada. Alberta Society of Petroleum Geologists, Calgary. Chapter 12.

Wuenschel, P.C. 1965. Dispersive body waves - an experimental study. Geophysics 30, pp. 539-551.

APPENDIX I

IMPULSE RESPONSE FUNCTION FOR NORMAL INCIDENCE

AI.1 Laplace Inversion of Transfer Functions

The normal incidence transfer function set:

$$
\begin{aligned}
H_{i_1}(s) &= \frac{G(s)}{1-F(s)G(s)} \cdot t_i \\
H_{i_2}(s) &= \frac{G^2(s)}{1-F(s)G(s)} \cdot t_i r_i' \\
H_{i_3}(s) &= \frac{G^2(s)}{1-F(s)G(s)} \cdot t_i' r_i \qquad \text{(A1-1)} \\
H_{i_4}(s) &= \frac{G(s)}{1-F(s)G(s)} \cdot t_i'
\end{aligned}
$$

where $G(s) = A_i(s)e^{-sT_i}$ and $F(s) = G(s)\cdot r_i r_i'$

must be inverse Laplace transformed to obtain the characteristic layer impulse response set:

$$h_{i_k}(t) = L^{-1}\{H_{i_k}(s)\} \quad .$$

Rather than directly attempt to invert the closed forms above, it is easier to return to the series representation and accomplish inversion term by term. This approach is used, for example, in transmission line theory (e.g., Bohn, 1963, Chapter 11) because the closed forms are generally unsuitable for Laplace inversions. Also, with the inclusion of a general absorption function $A_i(s)$, the pole set required for direct inversion cannot be calculated.

Thus for:

$$H_i(s) = t_i\{A_i(s)e^{-sT_i}+A_i^3(s)e^{-3sT_i}r_ir_i'+A_i^5(s)e^{-5sT_i}r_i^2r_i'^2+\ \ldots\} \tag{A1-2}$$

the impulse response series is easily determined by term by term inversion:

$$\begin{aligned} h_{i_1}(t) = t_i\{&a_i(t)*\delta(t-T_i)+a_i(t)*a_i(t)*a_i(t)*\delta(t-3T_i)r_ir_i' \\ &+ a_i(t)*\ldots*a_i(t)*\delta(t-5T_i)r_i^2r_i^2+\ \ldots\} \end{aligned} \tag{A1-3}$$

where $\quad a_i(t) = L^{-1}\{A_i(s)\}$

Noting that:

$$H_{i_2}(s) = (r_i'A_i(s)e^{-sT_i})H_{i_1}(s)$$

$$H_{i_3}(s) = (\frac{t_i'r_i}{t_i}A_i(s)e^{-sT_i})H_{i_1}(s) \tag{A1-4}$$

and $\quad H_{i_4}(s) = \frac{t_i'}{t_i}H_{i_1}(s)$

we may further determine:

$$h_{i_2}(t) = r_i'.a_i(t)*\delta(t-T_i)*h_{i_1}(t) \tag{A1-5}$$

$$h_{i_3}(t) = \frac{t_i{}'r_i}{t_i} \cdot a_i(t) * \delta(t-T_i) * h_{i_1}(t) \tag{A1-5}$$

and

$$h_{i_4}(t) = \frac{t_i{}'}{t_i} * h_{i_1}(t) \quad .$$

For non-attenuating conditions, $a_i(t)=1$ and the four response functions may be represented in simplified infinite series form:

$$h_{i_1}(t) = t_i \sum_{n=1}^{\infty} (r_i r_i{}')^{n-1} \delta(t-[2n-1]T_i)$$

$$h_{i_2}(t) = t_i r_i \sum_{n=1}^{\infty} (r_i r_i{}')^{n-1} \delta(t-2nT_i)$$

$$h_{i_3}(t) = t_i{}' r_i \sum_{n=1}^{\infty} (r_i r_i{}')^{n-1} \delta(t-2nT_i) \tag{A1-6}$$

and

$$h_{i_4}(t) = t_i{}' \sum_{n=1}^{\infty} (r_i r_i{}')^{n-1} \delta(t-[2n-1]T_i) \quad .$$

AI.2 Poles and Zeros of the Normal Incidence Transfer Functions

The four transfer functions (equation A1-1) each have a common denominator which determines the pole set at complex frequencies for which:

$$1-(r_i r_i{}')A_i{}^2(s)e^{-2sT_i} = 0 \tag{A1-7}$$

Since the $A_i(s)$ can represent any general attenuation function, no specific pole set can be determined without assumptions on $A_i(s)$. For the non-attenuating case, $A_i(s) = 1$. A physical constraint (conservation of energy) demands that the reflection coefficients at the two elastic boundaries of layer i obey:

$$|r_i r_i'| < 1 \quad . \tag{A1-8}$$

s is a complex number and the exponential must obey the periodic relationship:

$$e^{-2sT_i} = e^{-2sT_i} \cdot e^{i2n\pi} \tag{A1-9}$$

where n is any arbitrary integer.

Thus a solution of equation (A1-2) follows:

$$e^{2(in\pi - sT_i)} = \frac{1}{r_i r_i'} \tag{A1-10}$$

Taking the natural logarithm of this equation:

$$2(in\pi - sT_i) = -\ln(r_i r_i') \tag{A1-11}$$

and there are an infinite number of solutions for s:

$$s_n = \frac{1}{T_i}\{in\pi + \frac{1}{2}\ln(r_i r_i')\} \quad . \tag{A1-12}$$

Two conditions on the coefficients yield different general pole patterns:

Case I - $0 < r_i r_i' < 1$

Thus $\ln(r_i r_i')$ is negative real and the pole positions are shown in Figure 39. The poles are periodic with the rate $\omega = \pi/T_i$ $(f = \frac{1}{2T_i})$ the first non-zero frequency pole is at $f_1 = \frac{1}{2T_i}$.

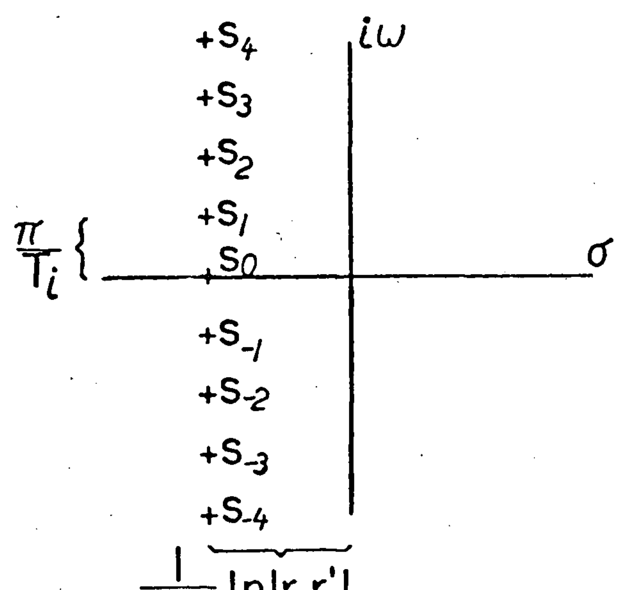

Fig. 39. Pole maps of the one layer transfer function for normal incidence: Case I.

<u>Case II</u> $- -1 < r_i r_i' < 0$

Set $r_i r_i' = |r_i r_i'| e^{i\pi}$. Thus $\ln(r_i r_i')$ is complex with principal value:

$$\ln(r_i r_i') = \ln|r_i r_i'| + i\pi \ . \tag{A1-13}$$

The poles $s_n = \frac{1}{T_i}\{i(n+1/2)+1/2\ln|r_i r_i'|\}$ are shown in Figure 40. Again, the poles are periodic with rate $f = \frac{1}{2T_i}$. However, the fundamental pole has the frequency component $f_o = \frac{1}{4T_i}$. These fundamental poles

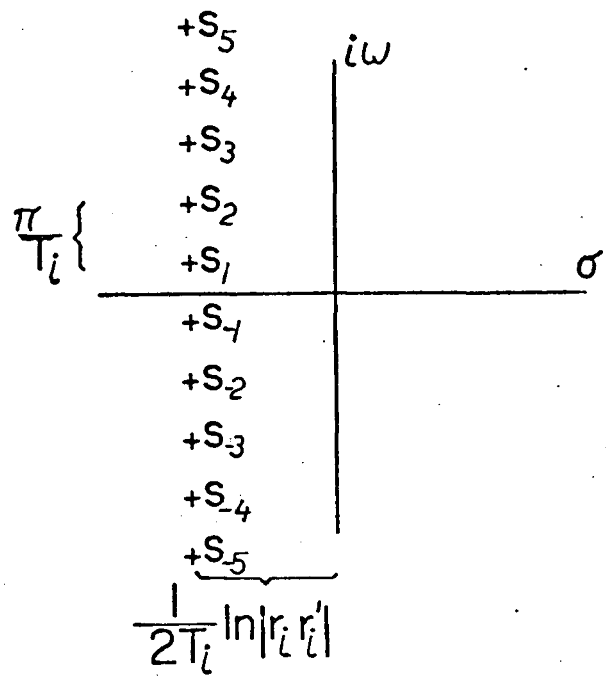

Fig. 40. Pole maps of the one layer transfer function for normal incidence: Case II.

at $f_1 = \frac{1}{2T_i}$ for Case I and $f_o = \frac{1}{4T_i}$ for Case II represent the fundamental reverberation resonance frequencies due to the layer; the periodic poles represent the harmonics. Each transfer function has zeros at infinite s.

For non-normal incidence, the computation of poles and zeros is much more difficult because the nature of the denominator of the transfer function is highly complicated (Appendix III). However, similar general features should prevail for incidence angles which are not large.

APPENDIX II

PHASE ADVANCE TRANSFER FUNCTIONS

Consider any layer i with origin as shown in Figure 41. The direct P wave ray which exits the upper boundary at $x=0$, $z=\eta_i$ enters the lower boundary at $x=a$, $z=0$. The phase at a given instant at $(a,0)$ is time advanced relative to the phase at point P and hence at the origin (0,0) according to the trigonometric relation:

$$\tau_{P_i} = (\eta_i \tan(e_i)\sin(e_i))/\alpha_i \quad . \tag{A2-1}$$

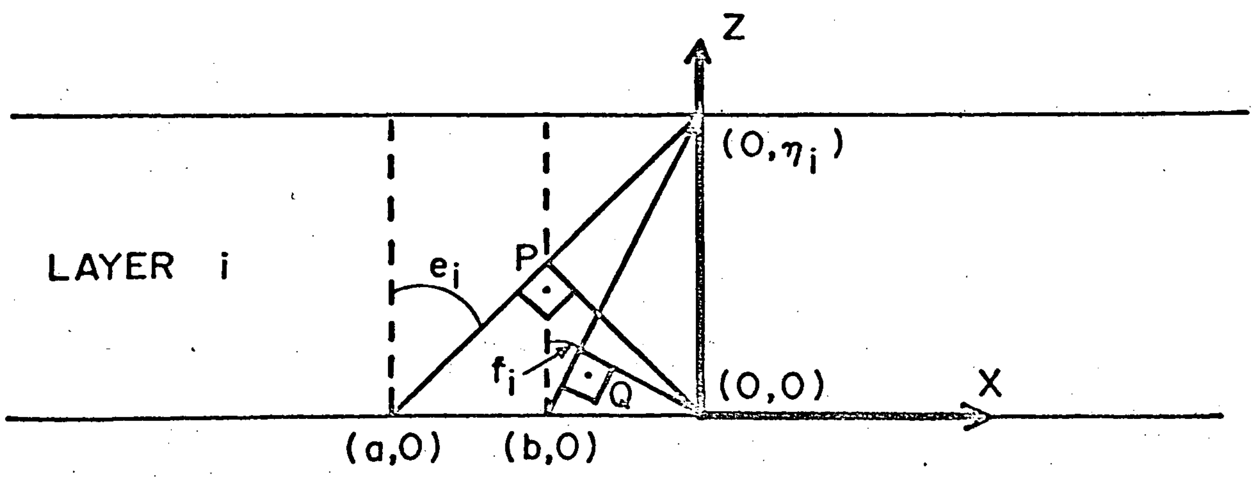

Fig. 41. A representation of phase advance time calculations necessary for non-normal condition analyses.

Similarly for the direct S wave entering at (b,0), the time advance between (b,0) and point Q is:

$$\tau_{s_i} = (\eta_i \tan(f_i)\sin(f_i))/\beta_i \quad . \tag{A2-2}$$

These advance times represent any one transit from one boundary to the other for the P and S waves respectively. Higher orders of reflections are included through further multiplication by identical advance functions. The included advance transfer functions of layer in Figure 8 exactly establish the correct phase relations for any possible combinations of internal reverberations.

The phase advance transfer functions and the layer delay functions may be combined into single delay functions:

$$e^{-sT'_{s_i}} \quad \text{and} \quad e^{-sT'_{p_i}}$$

where

$$T'_{p_i} = T_{p_i} - \tau_{p_i} = \frac{\eta_i}{\alpha_i}\cos(e_i) \tag{A2-3}$$

and

$$T'_{s_i} = T_{s_i} - \tau_{s_i} = \frac{\eta_i}{\beta_i}\cos(f_i) \quad . \tag{A2-4}$$

APPENDIX III

EXAMPLE BLOCK REDUCTION PROCEDURE

It is desirable to obtain a single transfer function H(s) to represent a system component (Figure 42) such that $V_o(s) = H(s)V_i(s)$.

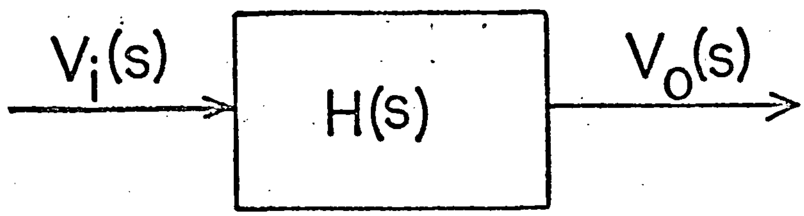

Fig. 42. The desired block diagram representation in terms of transfer function and transformed signals.

Two common system block diagrams can be easily conformed to this form using the standard block diagram reduction methods (Kuo, 1963).

Case I - Summed parallel systems (Figure 43):

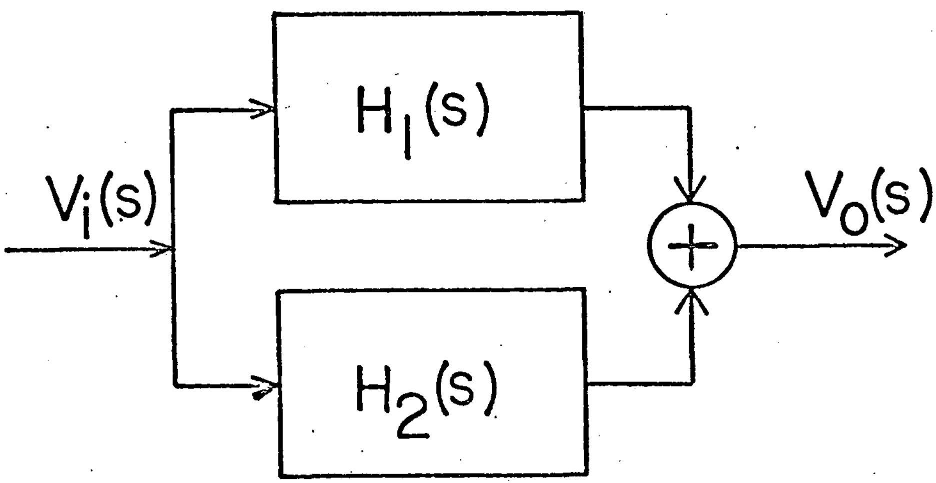

Fig. 43. Block diagram of parallel summing paths.

$$V_o(s) = (H_1(s)+H_2(s))V_i(s) \tag{A3-1}$$

Set:
$$H(s) = H_1(s)+H_2(s) \tag{A3-2}$$

Case II - Continuous (feedback systems) loops (Figure 44):

$$V_o(s) = \frac{H_1(s)}{1-H_1(s)H_2(s)} \cdot V_i(s) \tag{A3-3}$$

Set:
$$H(s) = \frac{H_1(s)}{1-H_1(s)H_2(s)} \tag{A3-4}$$

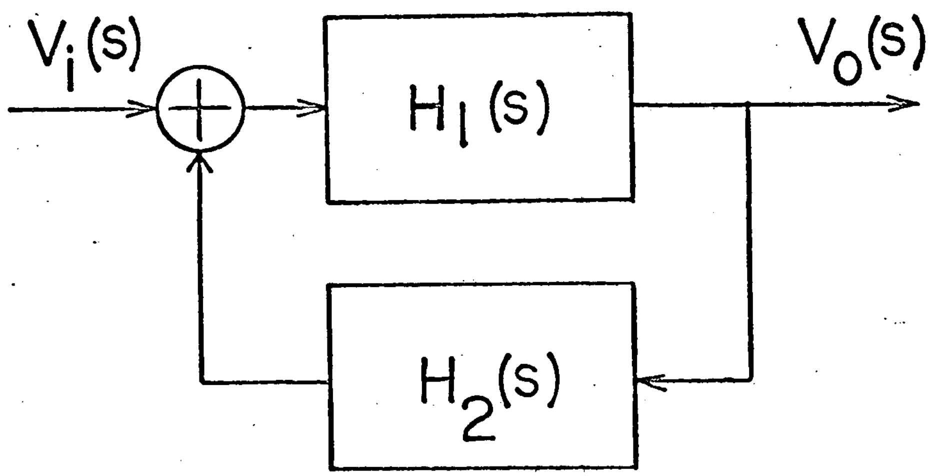

Fig. 44. Block diagram of the linear positive feedback system.

Example Reduction:

Refer to Figure 8 during the following reductions.

Given the equation:

$$U_{i-1}(s) = H_{i_1}(s)U_i(s) \tag{A3-5}$$

which relates an up travelling P wave entering layer i to the equivalent up travelling P wave entering layer i-1, determine

$$H_{i_1}(s) = U_{i-1}(s)/U_i(s). \tag{A3-6}$$

It is first necessary to determine the P and SV motions incident on the upper boundary due to the P and SV motions at the lower boundary. For simplicity, let the forward absorption and delay transfer functions be represented by (see Appendix II for definition of $T_{p_i}{}'$ and $T_{s_i}{}'$):

$$G_1(s) = A_{p_i}(s)e^{-sT_{p_i}{}'} \tag{A3-7}$$

$$G_2(s) = A_{s_i}(s)e^{-sT_{s_i}{}'} \tag{A3-8}$$

and the return transfer functions:

$$B_1(s) = r_{pp_i} r_{pp_i{}'} G_1(s)$$

$$B_2(s) = r_{ps_i} r_{sp_i{}'} G_2(s) \tag{A3-9}$$

$$B_3(s) = r_{sp_i} r_{pp_i{}'} G_1(s)$$

$$B_4(s) = r_{ss_i} r_{sp_i} \, G_2(s)$$

$$B_5(s) = r_{ps_i} r_{ss_i} \, G_2(s)$$

$$B_6(s) = r_{pp_i} r_{ps_i} \, G_1(s) \qquad \text{(A3-9)}$$

$$B_7(s) = r_{ss_i} r_{ss_i} \, G_2(s)$$

$$B_8(s) = r_{sp_i} r_{ps_i} \, G_1(s) \quad .$$

Combining the parallel transfer functions (Case I) the simplified block representation of Figure 45 is possible. Further combining $G_1(s)$ with its return path transfer function and $G_2(s)$ with its return path transfer function form:

$$F_1(s) = \frac{G_1(s)}{1-G_1(s)(B_1(s)+B_2(s))}$$

$$F_2(s) = \frac{G_2(s)}{1-G_2(s)(B_7(s)+B_8(s))} \qquad \text{(A3-10)}$$

Since it is intended only to obtain the layer response to the incident P wave, the only non-zero input signal is $U_i(s)$. The total open loop transfer function (obtained by breaking the continuous loop of Figure 44) is $F_1(s)F_2(s)(B_3(s)+B_4(s))(B_5(s)+B_6(s))$. The open loop and forward transfer functions combine to form (Case II):

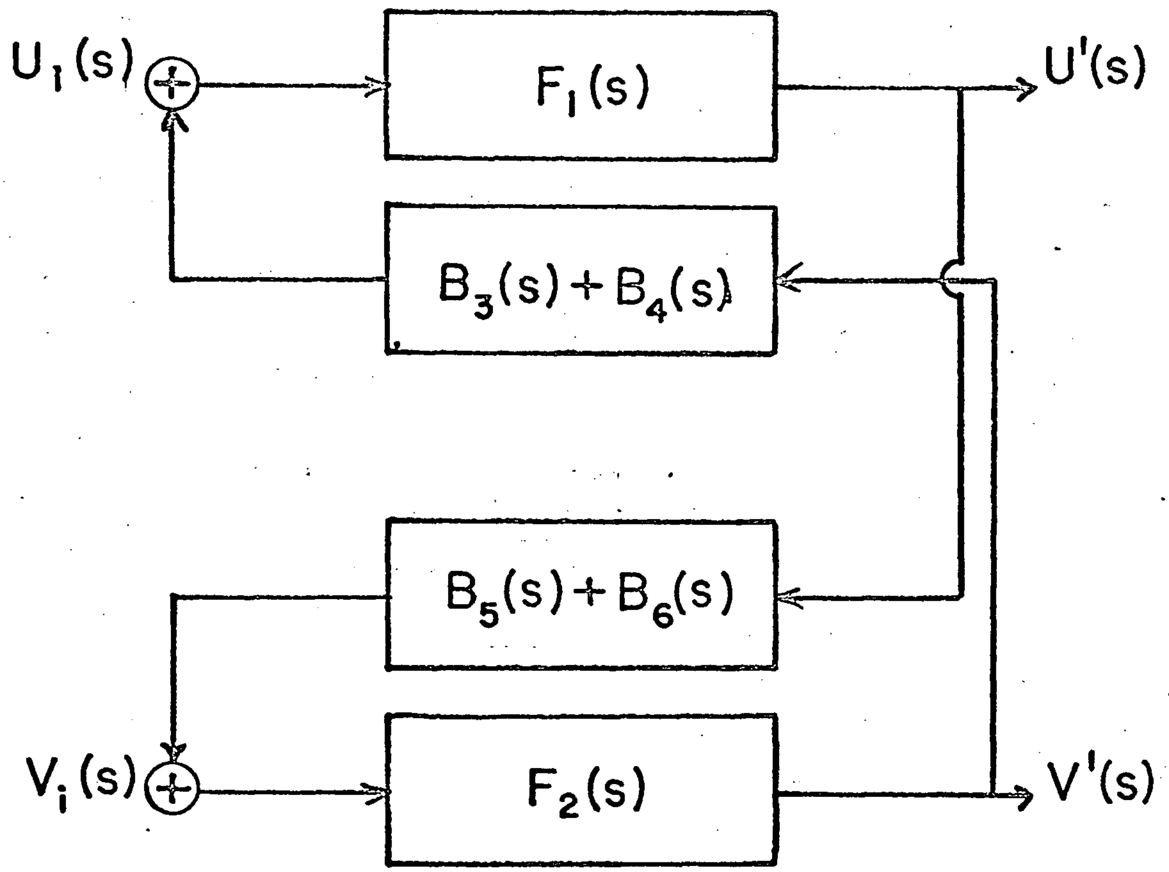

Fig. 45. The reduced system block diagram having the layer response to inputs $U_i(s)$ and $V_i(s)$.

$$\frac{U'(s)}{U_i(s)} = \frac{F_1(s)}{1-F_1(s)F_2(s)(B_5(s)+B_6(s))(B_3(s)+B_4(s))}$$

(A3-11)

$$\frac{V'(s)}{U_i(s)} = \frac{F_1(s)F_2(s)(B_5(s)+B_6(s))}{1-F_1(s)F_2(s)(B_5(s)+B_6(s))(B_3(s)+B_4(s))} \, .$$

The final transmission of these P and SV motions incident on the upper boundary through the upper boundary determines $U_{i-1}(s)$:

$$U_{i-1}(s) = t_{pp_i} U'(s) + t_{sp_i} V'(s) \tag{A3-12}$$

so that:

$$H_i\ (s) = \frac{U_{i-1}(s)}{U_i(s)} = \frac{F_1(s)\cdot t_{pp_i} + F_1(s)F_2(s)(B_5(s)+B_6(s))\cdot t_{sp_i}}{1-F_1(s)F_2(s)(B_5(s)+B_6(s))(B_3(s)+B_4(s))} \tag{A3-13}$$

Each transfer function $H_{i_k}(s)$ can be obtained in a similar manner. All 16 transfer function possess the same denominator.

APPENDIX IV

FORTRAN COMPUTER PROGRAMS FOR TIME DOMAIN SEISMOGRAM SYNTHESES AND FOURIER COMPONENT SOLUTIONS BASED ON THE LINEAR SYSTEMS THEORY

The following FORTRAN IV-G programs were used for the numerical solutions of the transmission problems in this thesis.

I: NON-NORMAL INCIDENCE CRUSTAL FOURIER TRANSFER FUNCTION PROGRAM

This program was used for the frequency domain transfer function solutions.

II: NON-NORMAL INCIDENCE SYNTHETIC SEISMOGRAM FOR ANGLES LESS THAN CRITICAL

This program was used for the time domain seismogram syntheses for non-normal incidence conditions. On an IBM System 360 Model 67 computer operating under the Michigan Terminal System, the computational time was approximately 0.005 second per layer per time increment for non-attenuating crust models. The computational time was slightly increased for attenuating layer models.

III: SUBROUTINES

All subprograms required by the above two programs are following.

```
C     NON-NORMAL INCIDENCE CRUSTAL FOURIER TRANSFER FUNCTION PROGRAM
C     ***************************************************************
C   PROGRAM DESCRIPTION
C     THE PROGRAM USES THE FREQUENCY DOMAIN LINEAR SYSTEMS CRUSTAL MODEL FOR
C     COMPUTATION OF SAMPLED FREQUENCY COMPONENT FOURIER TRANSFER FUNCTIONS
C   PROGRAM LIMITATIONS
C     MAXIMUM NO. OF LAYERS=10
C     MAXIMUM NO. OF FREQUENCY POINTS CALCULABLE=50
C     ACAUSAL ZERO-PHASE ATTENUATION IS ASSUMED - THE PROGRAM MAY BE
C     GENERALIZED TO CAUSAL ATTENUATION  BY ALLOWING COMPLEX ABSORPTION FNCS.
C   INPUT CARDS
C     CARD 1: TITLE
C     CARD 2: NO. OF LAYERS, NO. OF FREQUENCY POINTS, INITIAL FREQUENCY,
C             FINAL FREQUENCY
C     CARD 3: OUTPUT LIST AND ATTENUATOR FLAGS
C     SKIP OUTPUT LIST                     NFLAG1=0
C     SKIP ATTENUATION                     NFLAG2=0
C     CARD 4: FLAGS TO CHOOSE PROGRAM OPTIONS -
C     SKIP RATIO PROGRAM                   NRATIO=0
C     SKIP DISPLACEMENT PROGRAM            NDISPL=0
C     CARD 5FF: LAYER THICKNESS, P VELOCITY, S VELOCITY, DENSITY, Q FOR P,
C             Q FOR SV. - IF THE ATTENUATOR FLAG = 0 SKIP THE Q SPECIFICATIONS
C     CARD 6:  P OR S-WAVE INCIDENCE ANGLE WITH NORMAL - THE INPUT WAVE TYPE
C            IS DETERMINED BY WHICH ANGLE IS NON-ZERO.   FOR NORMAL INCIDENCE
C             VERY SMALL INCIDENCE ANGLES MAY BE USED WITHOUT DETECTABLE ERROR
      DIMENSION ALP(11),BET(11),RHO(11),H(10),E(11),F(11),TPP(21),TPS(21
     1),TSP(21),TSS(21),RSP(21),RSS(21),RPS(21),RPP(21),FREQ(50),VP(11)
     2,VS(11),TP(10),TS(10),AP(10),AS(10),EXPP(10),EXPS(10),STAT(15),UX(
     311),WZ(11),PANGLE(11),SANGLE(11),A(40,41),B(40,41),X(40,1),SINE(11
     4),SINF(11),COSE(11),COSF(11),TAUP(10),TAUS(10),RAT(50),UAMP(11,50)
     5,UPHS(11,50),WAMP(11,50),WPHS(11,50),QP(10),QS(10)
      COMPLEX EXPP,EXPS,G1,G2,A,H1,H2,H3,H4,X,DET,B,D1,D2,D3,D4,D5,D6,D7
     1,D8,P1,S1,UX,WZ
      DATA PI/3.1415927/
C   READ TITLE CARD: 80 CHARACTERS TO BE PRINTED ON OUTPUT
      READ(5,2) STAT
      WRITE(6,2) STAT
```

```
C  READ INPUT: NUMBER OF LAYERS NUMBER OF FREQUENCY POINTS,INITIAL FREQUENCY
C  AND FINAL FREQUENCY
      READ(5,10) N,MMAX,FREQ(1),FREQ(MMAX)
      NP=N+1
      FINC=(FREQ(MMAX)-FREQ(1))/FLOAT(MMAX-1)
      DO 1 I=2,MMAX
1     FREQ(I)=FREQ(I-1)+FINC
C  READ INPUT: FLAGS TO DETERMINE OPTIONS
      READ(5,3) NFLAG1,NFLAG2
      READ(5,3) NRATIO,NDISPL
      IF(NRATIO.EQ.0.AND.NDISPL.EQ.0) STOP
      WRITE(6,29)
      READ(5,11) ANGINP,ANGINS
      IF(NFLAG5.EQ.0) GO TO 13
C  READ INPUT: LAYER THICKNESS, P VELOCITY, S VELOCITY, DENSITY, ATTENUATION
C  CONSTANTS  FOR P AND SV MOTIONS
      READ(5,12) (H(I),ALP(I),BET(I),RHO(I),QP(I),QS(I),I=1,N)
      GO TO 111
C  READ INPUT: LAYER PARAMETERS WITHOUT ATTENUATION CONSTANTS -- THIS OPTION
C  IS USED WHEN ATTENUATOR FLAG IS SET TO 0
13    READ(5,121) (H(I),ALP(I),BET(I),RHO(I),I=1,N)
111   READ(5,121) DUMMY,ALP(NP),BET(NP),RHO(NP)
      WRITE(6,14) (I,ALP(I),BET(I),RHO(I),H(I),I=1,N)
      WRITE(6,14) NP,ALP(NP),BET(NP),RHO(NP)
      EQUIVALENCE (VP,ALP),(VS,BET)
C  REFLECTION AND TRANSMISSION ZOEPPRITZ' COEFFICIENTS ARE CALCULATED
      ANGINP=ANGINP*PI/180.
      ANGINS=ANGINS*PI/180.
      CALL COEGEN(N,VP,VS,RHO,ANGINP,ANGINS,E,F,TPP,TPS,RPP,RPS,TSP,TSS,
     1RSP,RSS)
C  LAYER TRANSIT TIMES AND PHASE ADVANCE TIMES ARE CALCULATED
      DO 5 I=1,N
      COSE(I)=COS(E(I))
      SINE(I)=SIN(E(I))
      COSF(I)=COS(F(I))
      SINF(I)=SIN(F(I))
      TP(I)=H(I)/(VP(I)*COSE(I))
      TS(I)=H(I)/(VS(I)*COSF(I))
      TAUP(I)=H(I)*SINE(I)*SINE(I)/(VP(I)*COSE(I))
```

```
      TAUS(I)=H(I)*SINF(I)*SINF(I)/(VS(I)*COSF(I))
5     CONTINUE
      COSE(NP)=COS(E(NP))
      SINE(NP)=SIN(E(NP))
      COSF(NP)=COS(F(NP))
      SINF(NP)=SIN(F(NP))
C  CALCULATION OF TRANSFER MATRIX VS. FREQUENCY
      IF(NFLAG2.NE.0) GO TO 221
      DO 222 I=1,N
C  ABSORPTION FUNCTIONS ARE SET TO ONE FOR NO ABSORPTION
      AP(I)=1.
222   AS(I)=1.
221   CONTINUE
      DO 99 M=1,MMAX
      W=PI*FREQ(M)*2.
C  CALCULATION OF ABSORPTION FUNCTIONS OF FREQUENCY
      IF(NFLAG2.EQ.0) GO TO 24
      DO 22 I=1,N
      AS(I)=EXP(-0.5*W*TS(I)/QS(I))
22    AP(I)=EXP(-0.5*W*TP(I)/QP(I))
24    CONTINUE
C  CALCULATION OF OF DELAY TRANSFER FUNCTIONS AT FREQUENCY COMPONENT
      DO 4 I=1,N
      A1=W*(TP(I)-TAUP(I))
      A2=W*(TS(I)-TAUS(I))
      EXPP(I)=CMPLX(COS(A1),-SIN(A1))
      EXPS(I)=CMPLX(COS(A2),-SIN(A2))
4     CONTINUE
      KMAX=4*N
      LMAXP=KMAX+1
      DO 20 K=1,KMAX
      DO 20 L=1,LMAXP
20    A(K,L) =0.
```

```
C  FORM MAIN DIAGONAL OF MATRIX -- ALL VALUES=-1.
      DO 21 K=1,KMAX
21    A(K,K)=-1.
C  COMPUTE REMAINING MATRIX COMPONENTS
      IF(N.EQ.1) GO TO 23
      DO 6 I=2,N
      G1=AP(I)*EXPP(I)
      G2=AS(I)*EXPS(I)
      J=I+NP
C  SUBROUTINE TRANS1 COMPUTES THE COMMON PARTS OF THE LAYER TRANSFER FUNCTIONS
C  FOR UP-TRAVELLING OUTPUT SIGNALS
      CALL TRANS1(RPP(I),RPS(I),RSP(I),RSS(I),RPP(J),RPS(J),RSP(J),RSS(J
     1),G1,G2,H1,H2,H3,H4)
      D1=TPP(I)*H1+TSP(I)*H3
      D2=TPP(I)*H2+TSP(I)*H4
      D3=TPS(I)*H1+TSS(I)*H3
      D4=TPS(I)*H2+TSS(I)*H4
      D5=RPP(J)*G1
      D6=RPS(J)*G1
      D7=RSP(J)*G2
      D8=RSS(J)*G2
      K=4*I-7
      L=K+4
      KP=K+1
      LP=L+1
C  INPUT-OUTPUT RELATIONS ARE INDICATED BY THE FOLLOWING COMMENT CARDS
C     A(U(I-1)/U(I))
      A(K,L)=D1
C     A(U(I-1)/V(I))
      A(K,LP)=D2
C     A(V(I-1)/U(I))
      A(KP,L)=D3
C     A(V(I-1)/V(I))
      A(KP,LP)=D4
      L=K+2
      LP=L+1
C     A(U(I-1)/D(I))
      A(K,L)=D5*D1+D6*D2
C     A(U(I-1)/E(I))
```

```
      A(K,LP)=D7*D1+D8*D2
C     A(V(I-1)/D(I))
      A(KP,L)=D5*D3+D6*D4
C     A(V(I-1)/E(I))
      A(KP,LP)=D7*D3+D8*D4
C  SUBROUTINE TRANS1 COMPUTES THE COMMON PARTS OF THE LAYER TRANSFER FUNCTIONS
C  FOR DOWN-TRAVELLING OUTPUT  SIGNALS
      CALL TRANS1(RPP(J),RPS(J),RSP(J),RSS(J),RPP(I),RPS(I),RSP(I),RSS(I
     1),G1,G2,H1,H2,H3,H4)
      D1=TPP(J)*H1+TSP(J)*H3
      D2=TPP(J)*H2+TSP(J)*H4
      D3=TPS(J)*H1+TSS(J)*H3
      D4=TPS(J)*H2+TSS(J)*H4
      D5=RPP(I)*G1
      D6=RPS(I)*G1
      D7=RSP(I)*G2
        D8=RSS(I)*G2
      K=4*I-1
      L=K-4
      KP=K+1
      LP=L+1
C     A(D(I+1)/D(I))
      A(K,L)=D1
C  INPUT-OUTPUT RELATIONS ARE INDICATED BY THE FOLLOWING COMMENT CARDS
C     A(D(I+1)/E(I))
      A(K,LP)=D2
C     A(E(I+1)/D(I))
      A(KP,L)=D3
C     A(E(I+1)/E(I))
      A(KP,LP)=D4
      L=K-2
      LP=L+1
C     A(D(I+1)/U(I))
      A(K,L)=D5*D1+D6*D2
C     A(D(I+1)/V(I))
      A(K,LP)=D7*D1+D8*D2
C     A(E(I+1)/U(I))
      A(KP,L)=D5*D3+D6*D4
C     A(E(I+1)/V(I))
```

```
      A(KP,LP)=D7*D3+D8*D4
6     CONTINUE
23    CONTINUE
C  CALCULATE TRANSFER MATRIX COMPONENTS FOR LAYER 1
      I=1
      J=1+NP
      G1=AP(1)*EXPP(1)
      G2=AS(1)*EXPS(1)
      CALL TRANS1(RPP(J),RPS(J),RSP(J),RSS(J),RPP(I),RPS(I),RSP(I),RSS(I
     1),G1,G2,H1,H2,H3,H4)
      D1=TPP(J)*H1+TSP(J)*H3
      D2=TPP(J)*H2+TSP(J)*H4
      D3=TPS(J)*H1+TSS(J)*H3
      D4=TPS(J)*H2+TSS(J)*H4
      D5=RPP(I)*G1
      D6=RPS(I)*G1
      D7=RSP(I)*G2
        D8=RSS(I)*G2
C     A(D(2)/U(1))
      A(3,1)=D5*D1+D6*D2
C     A(D(2)/V(1))
      A(3,2)=D7*D1+D8*D2
C     A(E(2)/U(1))
      A(4,1)=D5*D3+D6*D4
C     A(E(2)/V(1))
      A(4,2)=D7*D3+D8*D4
      K=4*N-3
      KP=K+1
      KPP=KP+1
      KPPP=KPP+1
      L=K+4
C  THE CONSTANT VECTOR DETERMINING INPUT CONDITIONS IS COMPUTED
      IF(ANGINS.EQ.0.) GO TO 7
```

```
      IF(ANGINP.EQ.0.) GO TO 8
C     A(U(N)/U(N+1))
7     A(K,L)=-TPP(NP)
C     A(V(N)/U(N+1))
      A(KP,L)=-TPS(NP)
C     A(D(N+1)/U(N+1))
      A(KPP,L)=-RPP(NP)
C     A(E(N+1)/U(N+1))
      A(KPPP,L)=-RPS(NP)
      GO TO 9
C     A(U(N)/V(N+1))
8     A(K,L)=-TSP(NP)
C     A(V(N)/V(N+1))
      A(KP,L)=-TSS(NP)
C     A(D(N+1)/V(N+1))
      A(KPP,L)=-RSP(NP)
C     A(E(N+1)/V(N+1))
      A(KPPP,L)=-RSS(NP)
9     CONTINUE
      DO 30 K=1,KMAX
      DO 30 L=1,LMAXP
30    B(K,L)=A(K,L)
      CALL GAUCOM(KMAX,B,X,DET,40,41)
      I=1
      J=1+NP
      CALL TRANS1(RPP(I),RPS(I),RSP(I),RSS(I),RPP(J),RPS(J),RSP(J),RSS(J
     1),G1,G2,H1,H2,H3,H4)
C  COMPUTE TRANSFER FUNCTION THROUGH UPPER LAYER TO FREE SURFACE BOUNDARY
      P1=H1*X(1,1)+H2*X(2,1)
      S1=H3*X(1,1)+H4*X(2,1)
C  CALCULATION OF SURFACE DISPLACEMENTS -- COMPLEX
      D1=P1*RPP(1)
      D2=S1*RSP(1)
      D3=S1*RSS(1)
      D4=P1*RPS(1)
      D5=(P1+D1+D2)*COSE(1)
      D6=(P1-D1-D2)*SINE(1)
      D7=(S1+D3+D4)*SINF(1)
      D8=(-S1+D3+D4)*COSF(1)
```

```
      UX(1)=D6+D8
      WZ(1)=D5+D7
      IF(MDISPL.EQ.0) GO TO 321
C  COMPUTATION OF  INTERIOR BOUNDARY DISPLACEMENTS -- COMPLEX
      DO 32 I=2,NP
      IM=I-1
      L4=4*IM
      L3=L4-1
      L2=L3-1
      L=L2-1
      D1=X(L,1)*COSE(IM)+X(L3,1)*COSE(I)
      D2=X(L,1)*SINE(IM)-X(L3,1)*SINE(I)
      D3=X(L2,1)*SINF(IM)+X(L4,1)*SINF(I)
      D4=-X(L2,1)*COSF(IM)+X(L4,1)*COSF(I)
      UX(I)=D2+D4
32    WZ(I)=D1+D3
C  COMPUTE SURFACE AND INTERNAL BOUNDARY DISPLACEMNTS VS. FREQUENCY IN TERMS OF
C  AMPLITUDE AND PHASE COMPONENTS
      DO 33 I=1,NP
      UXI=AIMAG(UX(I))
      UXR=REAL(UX(I))
      WZI=AIMAG(WZ(I))
      WZR=REAL(WZ(I))
      UAMP(I,M)=SQRT(UXR*UXR+UXI*UXI)
      WAMP(I,M)=SQRT(WZR*WZR+WZI*WZI)
      UPHS(I,M)=ATAN2(UXI,UXR)
33    WPHS(I,M)=ATAN2(WZI,WZR)
      DO 25 I=1,NP
      PANGLE(I)=E(I)*180./PI
      SANGLE(I)=F(I)*180./PI
25    CONTINUE
      IF(NFLAG1.EQ.0) GO TO 26
      WRITE(6,18) FREQ(M)
      WRITE(6,15)((A(K,L),L=1,LMAXP),K=1,KMAX)
      WRITE(6,15) (X(L,1),L=1,KMAX)
26    CONTINUE
      WRITE(6,17)
      WRITE(6,16) (I,UX(I),WZ(I),UAMP(I,M),UPHS(I,M),WAMP(I,M),WPHS(I,M)
     1,PANGLE(I),SANGLE(I),I=1,NP)
```

```
      WRITE(6,19) DET
27    CONTINUE
321   IF(NRATIO.EQ.0) GO TO 322
C  COMPUTATION OF SPECTRAL AMPLITUDE RATIOS FOR SURFACE MOTIONS-- INTERNAL
C  BOUNDARY SPECTRAL RATIOS COULD ALSO BE OBTINED
C  BOUNDARY SPECTRAL RATIOS COULD ALSO BE OBTAINED
      UXI=AIMAG(UX(1))
      UXR=REAL(UX(1))
      WZI=AIMAG(WZ(1))
      WZR=REAL(WZ(1))
      RAT(M)=SQRT(WZR*WZR+WZI*WZI)/SQRT(UXR*UXR+UXI*UXI)
322   CONTINUE
99    CONTINUE
      IF(NRATIO.NE.0) WRITE(6,110)
      IF(NRATIO.NE.0) WRITE(6,11) (FREQ(M),RAT(M),M=1,MMAX)
      STOP
2     FORMAT(15A4)
3     FORMAT(5I1)
10    FORMAT(2I2,2F6.2)
11    FORMAT(2F6.2)
110   FORMAT(' FREQ  RATIO')
12    FORMAT(6F8.4)
121   FORMAT(4F8.4)
14    FORMAT(I4,4F9.3)
15    FORMAT(18(1X,F5.2)/)
16    FORMAT(3X,I2,1X,10F11.4)
17    FORMAT(//2X,5HLAYER 8X,9HU-COMPLEX 13X,9HW-COMPLEX  9X,5HU-AMP 6X,
     15HU-PHS 6X,5HW-AMP 6X,5HW-PHS 6X,5HP-ANG 6X,5HS-ANG/12X,4HREAL 7X,
     24HIMAG 7X,4HREAL 7X,4HIMAG/)
18    FORMAT(//35X,10HMATRIX FOR F6.2,17HCYCLES PER SECOND  //)
19    FORMAT(/15H DETERMINANT=  2E17.7///)
29    FORMAT(1X,5HLAYER 2X,5HP-VEL 4X,5HS-VEL 3X,7HDENSITY 3X,5HDEPTH /)
      END
```

```
C       NON-NORMAL INCIDENCE SYNTHETIC SEISMOGRAM FOR ANGLES LESS THAN CRITICAL
C       *********************************************************************
C   PROGRAM DESCRIPTION
C       THE PROGRAM USES THE TIME DOMAIN LINEAR SYSTEMS CRUST MODEL FOR
C       SYNTHESIS OF SAMPLED TIME SERIES SYNTHETIC SEISMOGRAMS
C   PROGRAM LIMITATIONS
C       MAXIMUM NO. OF LAYERS=20
C       MAXIMUM NO. OF HELD POINTS PER LAYER=200
C       MAXIMUM NO. OF ATTENUATOR OPERATOR WEIGHTS PER LAYER=20
C       THE ATTENUATORS MUST BE CAUSAL
C       MAXIMUM NO. OF OUTPUT TIME POINTS=1000
C   INPUT CARDS:
C       CARD 1: TITLE
C       CARD 2: FLAG FOR ATTENUATION MODEL: FOR NO ATTENUATION ENTER 00
C       CARD 3: NO. OF LAYERS, NO. OF TIME SAMPLE POINTS, TIME INCREMENT
C               P INCIDENCE ANGLE, S INCIDENCE ANGLE.  THE NON-ZERO ANGLE
C               DETERMINES THE FORM OF THE INPUT WAVEFORM.
C       CARD 4FF:  LAYER THICKNESS, P VELOCITY, S VELOCITY, DENSITY
C                  CONTINUE TO BASEMENT
C       THE FOLLOWING CARDS ARE INCLUDED ONLY IF  NATTEN IS NOT EQUAL TO 00
C       CARD5FF: P AND S ATTENUATOR LENGTHS FOR LAYERS 1 TO N
C       CARD 6FF: P ATTEN WEIGHTS AND S ATTEN WEIGHTS FOR LAYERS 1 TO N
C       THE INPUT WAVEFORM TIME SERIES SAMPLE POINTS OF ANY LENGTH ARE
C       READ FROM DEVICE 4
C       *********************************************************************
       DIMENSION EPDLAY(20),ESDLAY(20),FPDLAY(20),FSDLAY(20),EP(20,200),
      $ES(20,200),FP(20,200),FS(20,200),RPP(41),RPS(41),RSP(41),RSS(41),
      $TPP(41),TPS(41),TSP(41),TSS(41),NTAUP(20),NTAUS(20),STAT(20),ALP(2
      $1),BET(21),RHO(21),H(21),AIN(1000),POUT(1000),SOUT(1000),USURF(100
      $0),WSURF(1000),E(21),F(21),ATTENP(20,20),ATTENS(20,20),JP(20),JS(2
      $0)
       DATA PI/3.1415927/
C      INITIALIZE ALL OUTPUTS
       DO 10 I=1,20
       EPDLAY(I)=0.
       ESDLAY(I)=0.
       FSDLAY(I)=0.
```

```
      FPDLAY(I)=0.
      NTAUP(I)=0.
      NTAUS(I)=0.
      DO 10 J=1,200
      EP(I,J)=0.
      ES(I,J)=0.
      FP(I,J)=0.
10    FS(I,J)=0.
      MMIN=0
      READ(5,1) STAT
      WRITE(6,1) STAT
      READ(5,9) NATTEN
      READ(5,2) N,MMAX,TINC,ANGINP,ANGINS
      NP=N+1
      NM=N-1
      READ(5,3) (H(I),ALP(I),BET(I),RHO(I),I=1,N)
      READ(5,3) DUMMY,ALP(NP),BET(NP),RHO(NP)
      WRITE(6,4)
      WRITE(6,5) (I,ALP(I),BET(I),RHO(I),H(I),I=1,N)
      WRITE(6,5) NP,ALP(NP),BET(NP),RHO(NP)
      ANGINP=ANGINP*PI/180.
      ANGINS=ANGINS*PI/180.
C     CALCULATE TRANSMISSION AND REFLECTION COEFFICIENTS
      CALL COEGEN(N,ALP,BET,RHO,ANGINP,ANGINS,E,F,TPP,TPS,RPP,RPS,TSP,
     $TSS,RSP,RSS)
C     CALCULATE TRANSIT TIMES AND DELAYS
      DO 50 I=1,N
      TAUP=H(I)*COS(E(I))/ALP(I)
      TAUS=H(I)*COS(F(I))/BET(I)
      NTAUP(I)=IFIX(TAUP/TINC+0.5)
      NTAUS(I)=IFIX(TAUS/TINC+0.5)
      IF(NTAUP(I).EQ.0) NTAUP(I)=1
      IF(NTAUS(I).EQ.0) NTAUS(I)=1
50    CONTINUE
      IF(NATTEN.EQ.0) GO TO 21
C     READ IN MODEL ATTENUATION PARAMETERS
C     READ IN ATTENUATION OPERATOR LENGTHS
      READ(5,9) (JP(I),JS(I),I=1,N)
C     READ ATTENUATOR WEIGHTS
```

```
      WRITE(6,101)
      DO 21  I=1,N
      JPLIM=JP(I)
      JSLIM=JS(I)
      READ(5,102) (ATTENP(I,K),K=1,JPLIM)
      READ(5,102) (ATTENS(I,K),K=1,JSLIM)
      WRITE(6,103) (ATTENP(I,K),K=1,JPLIM)
      WRITE(6,103) (ATTENS(I,K),K=1,JSLIM)
21    CONTINUE
      WRITE(6,8)
C     READ INPUT WAVEFORM FROM DEVICE 4
      READ(4,7,END=99) (AIN(I),I=1,1000)
99    MEND=I
      DO 98 I=MEND,MMAX
      AIN(I)=0.0
98    CONTINUE
      DO 100 M=1,MMAX
      IF(ANGINP.NE.0.0) GO TO 22
      SINPUT=AIN(M)
      PINPUT=0.0
      GO TO 23
22    PINPUT=AIN(M)
      SINPUT=0.0
23    CONTINUE
C     UPDATE ALL DELAY OUTPUTS
C     FOR ALL LAYERS
      IF(NATTEN.EQ.0) GO TO 24
C    ATTENUATING MODEL SYNTHESIS DELAY OPERATIONS FOR ALL LAYERS
C     DELAY
      DO 28 I=1,N
      NTP=NTAUP(I)
      NTS=NTAUS(I)
      NTPM=NTP-1
      NTSM=NTS-1
      EPINTP=EP(I,NTP)
      FPINTP=FP(I,NTP)
      ESINTS=ES(I,NTS)
      FSINTS=FS(I,NTS)
C     ATTENUATION OPERATOR CONVOLUTIONS
```

```
      EPDLAY(I)=EPINTP*ATTENP(I,1)
      ESDLAY(I)=ESINTS*ATTENS(I,1)
      FPDLAY(I)=FPINTP*ATTENP(I,1)
      FSDLAY(I)=FSINTS*ATTENS(I,1)
      DO 25 K=1,NTPM
      IF(K.GE.JP(I)) GO TO 26
      EP(I,NTP-K+1)=EP(I,NTP-K)+EPINTP*ATTENP(I,K+1)
      FP(I,NTP-K+1)=FP(I,NTP-K)+FPINTP*ATTENP(I,K+1)
      GO TO 25
26    EP(I,NTP-K+1)=EP(I,NTP-K)
      FP(I,NTP-K+1)=FP(I,NTP-K)
25    CONTINUE
      DO 28 K=1,NTSM
      IF(K.GE.JS(I)) GO TO 27
      ES(I,NTS-K+1)=ES(I,NTS-K)+ESINTS*ATTENS(I,K+1)
      FS(I,NTS-K+1)=FS(I,NTS-K)+FSINTS*ATTENS(I,K+1)
      GO TO 28
27    ES(I,NTS-K+1)=ES(I,NTS-K)
      FS(I,NTS-K+1)=FS(I,NTS-K)
28    CONTINUE
      GO TO 30
C     NON-ATTENUATING MODEL SYNTHESIS DELAY OPERATIONS
24    CONTINUE
C     DELAY
      DO 30 I=1,N
      NTP=NTAUP(I)
      NTPM=NTP-1
      NTS=NTAUS(I)
      NTSM=NTS-1
      EPDLAY(I)=EP(I,NTP)
      ESDLAY(I)=ES(I,NTS)
      FSDLAY(I)=FS(I,NTS)
      FPDLAY(I)=FP(I,NTP)
      DO 301 K=1,NTPM
      EP(I,NTP-K+1)=EP(I,NTP-K)
301   FP(I,NTP-K+1)=FP(I,NTP-K)
      DO 302 K=1,NTSM
      ES(I,NTS-K+1)=ES(I,NTS-K)
302   FS(I,NTS-K+1)=FS(I,NTS-K)
```

```
30    CONTINUE
C     COMPUTE WAVEFORMS RETRANSMITTED INTO BASEMENT AT TIME SAMPLE M
      POUTPT=TSP(N+NP)*FSDLAY(N)+TPP(N+NP)*FPDLAY(N)+RSP(NP)*SINPUT+RPP
     $(NP)*PINPUT
      SOUTPT=TSS(N+NP)*FSDLAY(N)+TPS(N+NP)*FPDLAY(N)+RSS(NP)*SINPUT+RPS
     $(NP)*PINPUT
C     JUNCTION UPDATE TO TIME SAMPLE M
C     BOTTOM LAYER
      EP(N,1)=TSP(NP)*SINPUT+TPP(NP)*PINPUT+RPP(N+NP)*FPDLAY(N)+RSP(N+NP
     $)*FSDLAY(N)
      ES(N,1)=TSS(NP)*SINPUT+TPS(NP)*PINPUT+RSS(N+NP)*FSDLAY(N)+RPS(N+NP
     $)*FPDLAY(N)
      FP(N,1)=TSP(N+NP-1)*FSDLAY(N-1)+TPP(N+NP-1)*FPDLAY(N-1)+RSP(N)*ESD
     $LAY(N)+RPP(N)*EPDLAY(N)
      FS(N,1)=TSS(N+NP-1)*FSDLAY(N-1)+TPS(N+NP-1)*FPDLAY(N-1)+RSS(N)*ESD
     $LAY(N)+RPS(N)*EPDLAY(N)
C     INTERMEDIATE LAYERS
      IF(N.EQ.2) GO TO 41
      DO 40 I=2,NM
      EP(I,1)=TSP(I+1)*ESDLAY(I+1)+TPP(I+1)*EPDLAY(I+1)+RSP(I+NP)*FSDLAY
     $(I)+RPP(I+NP)*FPDLAY(I)
      ES(I,1)=TSS(I+1)*ESDLAY(I+1)+TPS(I+1)*EPDLAY(I+1)+RSS(I+NP)*FSDLAY
     $(I)+RPS(I+NP)*FPDLAY(I)
      FP(I,1)=TSP(I+NP-1)*FSDLAY(I-1)+TPP(I+NP-1)*FPDLAY(I-1)+RSP(I)*ESD
     $LAY(I)+RPP(I)*EPDLAY(I)
40    FS(I,1)=TSS(I+NP-1)*FSDLAY(I-1)+TPS(I+NP-1)*FPDLAY(I-1)+RSS(I)*ESD
     $LAY(I)+RPS(I)*EPDLAY(I)
41    CONTINUE
C     TOP LAYER
      EP(1,1)=TSP(2)*ESDLAY(2)+TPP(2)*EPDLAY(2)+RSP(1+NP)*FSDLAY(1)+RPP(
     $1+NP)*FPDLAY(1)
      ES(1,1)=TSS(2)*ESDLAY(2)+TPS(2)*EPDLAY(2)+RSS(1+NP)*FSDLAY(1)+RPS(
     $1+NP)*FPDLAY(1)
      FP(1,1)=RSP(1)*ESDLAY(1)+RPP(1)*EPDLAY(1)
      FS(1,1)=RSS(1)*ESDLAY(1)+RPS(1)*EPDLAY(1)
C     END OF JUNCTION UPDATE TO TIME SAMPLE M
C     COMPUTE SURFACE MOTIONS FROM IMPINGING S AND P WAVEFORMS
      PZ=(EPDLAY(1)*(1.+RPP(1))+ESDLAY(1)*RSP(1))*COS(E(1))
      PX=(EPDLAY(1)*(1.-RPP(1))-ESDLAY(1)*RSP(1))*SIN(E(1))
```

```
      SZ=(ESDLAY(1)*(1.+RSS(1))+EPDLAY(1)*RPS(1))*SIN(F(1))
      SX=(-ESDLAY(1)*(1.-RSS(1))+EPDLAY(1)*RPS(1))*COS(F(1))
      UO=PX+SX
      WO=PZ+SZ
      XM=FLOAT(M-1)*TINC
C     WRITE OUT FIRST 200 TIME SAMPLES FOR CHECK
      IF(M.LT.200) WRITE(6,6) XM,PINPUT,SINPUT,POUTPT,SOUTPT,WO,UO
C     SAVE OUTPUT SURFACE MOTIONS AND BASEMENT WAVEFORM TIME SERIES FOR
C     LATER PLOTTING OR WRITEOUT
      POUT(M)=POUTPT
      SOUT(M)=SOUTPT
      USURF(M)=UO
      WSURF(M)=WO
100   CONTINUE
      STOP
1     FORMAT(20A4)
2     FORMAT(I2,I4,3F8.4)
3     FORMAT(4F8.4)
4     FORMAT('LAYER   P-VEL     S-VEL     DENSITY     DEPTH')
5     FORMAT(2X,I2,1X,4F10.4)
6     FORMAT(F8.4,6E17.7)
7     FORMAT(10F8.5)
8     FORMAT('  TIME     INPUT P PULSE     INPUT S PULSE    BASEMENT P REFL
     $  BASEMENT S REFL   VERT SURF MOTION   HORZ SURF MOTION')
9     FORMAT(20I2)
101   FORMAT(' FILTER WEIGHTS FOR P AND S MOTIONS IN LAYERS 1 TO N')
102   FORMAT(16F5.3)
103   FORMAT(16F6.3)
104   FORMAT(10E10.3)
      END
```

```
C   ZOEPPRITZ COEFFICIENT GENERATION PROGRAM
C   ********************************************
C   SUBROUTINE DISCRIPTION
C   VARIABLES TRANSMITTED FROM MAIN
C      N: NUMBER OF LAYERS
C      ALP,BET,RHO: P AND S VELOCITIES AND LAYER DENSITIES
C      ANGINP,ANGINS: THE INCIDENT P AND S ANGLES AT THE BASEMENT BOUNDARY
C      E,F: THE INTERNAL LAYER P AND S ANGLES WITH THE NORMAL
C      TPP, RPP ETC:  ZOEPPRITZ' COEFFICIENTS FOR TOP BOUNDARY 1 TO N+1
C                     FOR BOTTOM BOUNDARY N+2 TO 2N
C   **************************************************************
      SUBROUTINE COEGEN(N,ALP,BET,RHO,ANGINP,ANGINS,E,F,TPP,TPS,RPP,
     1RPS,TSP,TSS,RSP,RSS)
C     MCCAMY NOTATION FOR ZOEPPRITZ' EQUATIONS
      DIMENSION ALP(1),BET(1),RHO(1),E(1),F(1),TPP(1),TPS(1),RPP(1),RPS(
     $1),TSP(1),TSS(1),RSP(1),RSS(1),W(2,2),Z(2,3),COF(2,1)
      NP=N+1
      IF(ANGINP.EQ.0.) GO TO 2
      E(NP)=ANGINP
1     C=ALP(NP)/SIN(E(NP))
      GO TO 3
2     F(NP)=ANGINS
      C=BET(NP)/SIN(F(NP))
3     CONTINUE
      DO 4 I=1,NP
      X=ALP(I)/C
      Y=BET(I)/C
      IF(X.GT.1.) GO TO 10
      E(I)=ATAN2(X,SQRT(1.-X*X))
14    IF(Y.GT.1.) GO TO 15
      F(I)=ATAN2(Y,SQRT(1.-Y*Y))
      GO TO 4
10    WRITE(6,11) I
      E(I)=1.5707964
      GO TO 14
15    WRITE(6,11) I
      F(I)=1.5707964
```

```
      GO TO 4
 11   FORMAT(47H CRITICAL REFLECTION- NO TRANSMISSION TO LAYER  I2)
 4    CONTINUE
C     FREE SURFACE REFLECTION COEFFICIENTS
      TPP(1)=0.
      TPS(1)=0.
      TSP(1)=0.
      TSS(1)=0.
      W(1,1)=-SIN(2.*E(1))
      W(2,1)=+COS(2.*F(1))
      W(1,2)=+ALP(1)*COS(2.*F(1))/BET(1)
      W(2,2)=+BET(1)*SIN(2.*F(1))/ALP(1)
      DO 20 L=1,2
      DO 20 M=1,2
 20   Z(L,M)=W(L,M)
      Z(1,3)=-W(1,1)
      Z(2,3)=+W(2,1)
      CALL GAUELI(2,Z,COF,DET,2,3)
      RPP(1)=COF(1,1)
      RPS(1)=COF(2,1)
      DO 21 L=1,2
      DO 21 M=1,2
 21   Z(L,M)=W(L,M)
      Z(1,3)=-W(1,2)
      Z(2,3)=W(2,2)
      CALL GAUELI(2,Z,COF,DET,2,3)
      RSP(1)=COF(1,1)
      RSS(1)=COF(2,1)
      DO 12 I=2,NP
      J=I-1
      K=I
 12   CALL COEFF(ALP,BET,RHO,E,F,TPP,TPS,RPP,RPS,TSP,TSS,RSP,RSS,I,J,K)
      DO 13 I=1,N
      J=I+1
      KNP=I+NP
 13   CALL COEFF(ALP,BET,RHO,E,F,TPP,TPS,RPP,RPS,TSP,TSS,RSP,RSS,I,J,KNP
     1)
      RETURN
      END
```

```
C   SECOND COEFFICIENT SUBROUTINE
C   ******** *******************
C   THIS SUBROUTINE IS REQUIRED BY COEGEN
C   *****************************************
       SUBROUTINE COEFF(ALP,BET,RHO,E,F,TPP,TPS,RPP,RPS,TSP,TSS,RSP,RSS,I
      1,J,K)
       DIMENSION ALP(1),BET(1),RHO(1),E(1),F(1),TPP(1),TPS(1),RPP(1),RPS(
      $1),TSP(1),TSS(1),RSP(1),RSS(1),C(4,4),Z(4,5),COF(4,1)
       C(1,1)=-SIN(E(I))
       C(1,2)=+COS(F(I))
       C(1,3)=-SIN(E(J))
       C(1,4)=+COS(F(J))
       C(2,1)=+COS(E(I))
       C(2,2)=+SIN(F(I))
       C(2,3)=-COS(E(J))
       C(2,4)=-SIN(F(J))
       C(3,1)=+COS(2.*F(I))
       C(3,2)=+BET(I)/ALP(I)*SIN(2.*F(I))
       C(3,3)=+RHO(J)/RHO(I)*ALP(J)/ALP(I)*COS(2.*F(J))
       C(3,4)=+RHO(J)/RHO(I)*BET(J)/ALP(I)*SIN(2.*F(J))
       C(4,1)=-SIN(2.*E(I))
       C(4,2)=+ALP(I)/BET(I)*COS(2.*F(I))
       C(4,3)=RHO(J)/RHO(I)*((BET(J)/BET(I))**2)*ALP(I)/ALP(J)*SIN(2.*E(J
      1))
       C(4,4)=-RHO(J)/RHO(I)*((BET(J)/BET(I))**2)*ALP(I)/BET(J)*COS(2.*F(
      1J))
       DO 20 L=1,4
       DO 20 M=1,4
20     Z(L,M)=C(L,M)
       Z(1,5)=-SIN(E(I))
       Z(2,5)=-COS(E(I))
       Z(3,5)=+COS(2.*F(I))
       Z(4,5)=+SIN(2.*E(I))
       CALL GAUELI(4,Z,COF,DET,4,5)
       RPP(K)=COF(1,1)
       RPS(K)=COF(2,1)
       TPP(K)=COF(3,1)
```

```
      TPS(K)=COF(4,1)
      DO 21 L=1,4
      DO 21 M=1,4
21    Z(L,M)=C(L,M)
      Z(1,5)=+COS(F(I))
      Z(2,5)=-SIN(F(I))
      Z(3,5)=+BET(I)/ALP(I)*SIN(2.*F(I))
      Z(4,5)=-ALP(I)/BET(I)*COS(2.*F(I))
      CALL GAUELI(4,Z,COF,DET,4,5)
      RSP(K)=COF(1,1)
      RSS(K)=COF(2,1)
      TSP(K)=COF(3,1)
      TSS(K)=COF(4,1)
      RETURN
      END
```

```
C   BASIC LAYER TRANSFER FUNCTION GENERATION PROGRAM
C   ******************************************************
C   THIS SUBROUTINE IS CALLED BY THE FOURIER COEFFICIENT MAIN PROGRAM
C   ***********************************************************************
      SUBROUTINE TRANS1(RPPI,RPSI,RSPI,RSSI,RPPJ,RPSJ,RSPJ,RSSJ,G1,G2,H1
     1,H2,H3,H4)
      COMPLEX RPPI,RPSI,RSPI,RSSI,RPPJ,RPSJ,RSPJ,RSSJ,G1,G2,H1,H2,
     1H3,H4,B1,B2,B3,B4,B5,B6,B7,B8,DEN
      B1=G1*RPPJ
      B3=B1*RSPI
      B1=B1*RPPI
      B6=G1*RPSJ
      B8=B6*RSPI
      B6=B6*RPPI
      B5=G2*RSSJ
      B7=B5*RSSI
      B5=B5*RPSI
      B4=G2*RSPJ
      B2=B4*RPSI
      B4=B4*RSSI
      B1=B1+B2
      B3=B3+B4
      B5=B5+B6
      B7=B7+B8
      B2=G1/(1.-G1*B1)
      B4=G2/(1.-G2*B7)
      DEN=1./(1.-B2*B3*B4*B5)
      H1=B2*DEN
      H2=B4*H1
      H3=B5*H2
      H2=B3*H2
      H4=B4*DEN
      RETURN
      END
```

```
C   GAUSS ELIMINATION SUBROUTINE FOR REAL SIMULTANEOUS EQUATIONS
C   ************************************************************************
C   PROGRAM DISCRIPTION
C   TRANSMITTED VARIABLES
C       N: NUMBER OF EQUATIONS
C       A: INPUT COEFFICIENTS ( CONSTANT VECTOR IN ROW N+1)
C       X: OUTPUT SOLUTION VECTOR
C       DET: CHECK DETERMINANT
C       ID: MAIN PROGRAM DIMENSION OF FIRST DIMENSION OF A
C       JD: MAIN PROGRAM DIMENSION OF SECOND DIMENSION OF A
C   ********************************************************************
        SUBROUTINE GAUELI(N,A,X,DET,ID,JD)
        DIMENSION A(ID,JD),X(ID,1)
        NP=N+1
        NM=N-1
        DET=1.0
C       TRIANGULARIZATION
        DO 12 K=1,NM
        KP=K+1
        R=1.0/A(K,K)
        DET=DET*A(K,K)
        DO 11 J=KP,NP
11      A(K,J)=R*A(K,J)
        DO 12 I=KP,N
        S=A(I,K)
        DO 12 J=KP,NP
12      A(I,J)=A(I,J)-S*A(K,J)
        DET=DET*A(N,N)
C       BACK SUBSTITUTION
        X(N,1)=A(N,NP)/A(N,N)
        DO 22 I=1,NM
        K=N-I
        KP=K+1
        S=A(K,NP)
        DO 21 J=KP,N
21      S=S-A(K,J)*X(J,1)
22      X(K,1)=S
        RETURN
        END
```

```
C   GAUSS ELIMINATION SUBROUTINE FOR COMPLEX SIMULTANEOUS EQUATIONS
C   ***************************************************************
C   PROGRAM DISCRIPTION
C   TRANSMITTED VARIABLES
C      N: NUMBER OF EQUATIONS
C      A: INPUT COEFFICIENTS ( CONSTANT VECTOR IN ROW N+1)
C      X: OUTPUT SOLUTION VECTOR
C      DET: CHECK DETERMINANT
C      ID: MAIN PROGRAM DIMENSION OF FIRST DIMENSION OF A
C      JD: MAIN PROGRAM DIMENSION OF SECOND DIMENSION OF A
C   ***********************************************************
      SUBROUTINE GAUCOM(N,A,X,DET,ID,JD)
C     GAUSS ELIMINATION SUBROUTINE FOR  COMPLEX SIMULTANEOUS EQUATIONS
      COMPLEX A,X DET,S
      DIMENSION A(ID,JD),X(ID,1)
      NP=N+1
      NM=N-1
      DET=1.0
C     TRIANGULARIZATION
      DO 12 K=1,NM
      KP=K+1
      R=1.0/A(K,K)
      DET=DET*A(K,K)
      DO 11 J=KP,NP
11    A(K,J)=R*A(K,J)
      DO 12 I=KP,N
      S=A(I,K)
      DO 12 J=KP,NP
12    A(I,J)=A(I,J)-S*A(K,J)
      DET=DET*A(N,N)
C     BACK SUBSTITUTION
      X(N,1)=A(N,NP)/A(N,N)
      DO 22 I=1,NM
      K=N-I
      KP=K+1
      S=A(K,NP)
      DO 21 J=KP,N
21    S=S-A(K,J)*X(J,1)
22    X(K,1)=S
      RETURN
      END
```